1-10-2012

A Quantitative Determination of Air-water Heat Fluxes in Hermit Lake, New Hampshire Under Varying Meteorological Conditions, Time of Day, and Time of Year

Nicholas D. Kyper
Plymouth State University, ndkyper@gmail.com

A QUANTITATIVE DETERMINATION OF AIR-WATER HEAT FLUXES IN HERMIT LAKE, NEW HAMPSHIRE UNDER VARYING METEOROLOGICAL CONDITIONS, TIME OF DAY, AND TIME OF YEAR

by

NICHOLAS D. KYPER

B.S., MILLERSVILLE UNIVERSITY, 2010

THESIS

Submitted to Plymouth State University

in Partial Fulfillment of

the Requirements for the Degree of

Master of Science

in

Applied Meteorology

December, 2011

This thesis has been examined and approved.

_____

Thesis Director, Samuel T. Miller
Associate Professor of Meteorology
Department of Atmospheric Sciences and Chemistry

_____

Lisa Doner
Research Assistant Professor
Center for the Environment

_____

Scott Smyers
Senior Scientist
Oxbow Associates, Inc.

_____

Date

DEDICATION

This thesis is dedicated to my family and Felicia. Without all of their love and support, none of this would have been possible.

ACKNOWLEDGEMENTS

First and foremost I would like to thank my thesis advisor, Dr. Samuel Miller. His guidance and insight proved to be more than valuable throughout this research. I appreciate all that Sam has done for me for this thesis and during my time at Plymouth State. I would also like to thank Dr. Lisa Doner and Scott Smyers who were also a part of my thesis committee. This research would not be possible without the funding obtained by Lisa and I appreciate the valuable opportunity that was provided to me by her. Scott Smyer's frog sound data and his knowledge of the data were key components to this research and I thank him for providing both.

Next, I would like to thank the Mount Washington Observatory for providing the meteorological data used throughout the course of this study and Plymouth State's Center for the Environment for providing the funds to cover my educational expenses. Assistance with programming and technical issues provided by Brendon Hoch and guidance regarding synoptic events provided by Dr. Eric Hoffman were much appreciated.

Finally, I would like to thank my parents, Patricia and David Kyper and my spouse Felicia Pflum. Without their love, support, and belief in me, I would not be the man I am today nor would I be where I am. I truly appreciate everything they have done for me and I hope they are proud of what I have accomplished.

TABLE OF CONTENTS

LIST OF TABLES

LIST OF FIGURES

ABSTRACT

A QUANTITATIVE DETERMINATION OF AIR-WATER HEAT FLUXES IN HERMIT LAKE, NEW HAMPSHIRE UNDER VARYING METEOROLOGICAL CONDITIONS, TIME OF DAY, AND TIME OF YEAR

by

Nicholas D. Kyper

Plymouth State University, December, 2011

An extensive heat flux study is performed at Hermit Lake, New Hampshire from May 26, 2010 till November 7, 2010 to determine the effects of the five individual heat fluxes on Hermit Lake and the surrounding amphibian community. Hermit Lake was chosen due to the relatively long meteorological observations record within the White Mountains of New Hampshire, a new lakeside meteorological station, and ongoing phenology studies of the surrounding eco-system. Utilizing meteorological data from the lakeside weather station and moored water temperature sensors, the incident (Q_i), blackbody ($Q_{b_{net}}$), latent (Q_e), sensible (Q_s), and net (Q_n) heat fluxes are calculated.

The incident heat flux is the dominate term in the net flux, accounting for 93% of the variance found in Q_n and producing a heat gain of ~ 19x10^8 J m^{-2} throughout the period of study. This large gain produces a net gain of heat in the lake until October 1, 2010, where gains by Q_i are offset by the large combined losses of $Q_{b_{net}}$, Q_s, and Q_e thereby producing a gradual decline of heat within the lake. The latent and blackbody heat fluxes produce the largest losses of heat in the net heat flux with a total losses of ~ -8x10^8 J m^{-2} and ~ -7x10^8 J m^{-2}, respectively. The sensible heat flux is negligible,

producing a total minimal loss of ~ $-1x10^8$ J m^{-2}. Overall the net heat produces a net gain of heat of $2x10^8$ J m^{-2} throughout the study period.

Frog calls indicative of breeding are recorded from May 26, 2010 until August 16, 2010. The spring peeper, American toad, and green frog each produced enough actively calling days to be compared to air temperature, surface water temperature, and wind speed data, as well as data from the five heat fluxes. Linear regression analysis reveals that certain water temperature thresholds affect the calling activities of the spring peeper and green frog, while higher wind speeds have a dramatic effect on the calling activities of both the green frog and American toad. All three frog species phenological activities are also affected by certain thresholds in the incident, blackbody, latent, sensible, and net heat fluxes.

CHAPTER 1

1. Background

a. Introduction

Air-sea interaction is a very important component to determining the global heat budget and understanding how the climate of the Earth is changing (Gill 1982). This heat transfer is governed by four individual heat fluxes. These fluxes include two radiative fluxes (shortwave and longwave) and two turbulent fluxes (evaporative and sensible) (Josey *et al.* 1997). While this interaction between the world's oceans and the atmosphere is important on a global scale, it is also necessary to understand the air-water interaction in lakes, rivers, and streams in the context of local environments. For these smaller scale water bodies, the air-water interaction is important to eco-system sustainability, especially with regard to potential impacts of climate change, whether it be the surrounding vegetation, amphibians, and/or aquatic species (Churchill and Kerfoot 2007).

The focus of this study is on the air-water interaction for Hermit Lake, a small (0.2 ha) alpine lake located at the base of Tuckerman's Ravine on the southeast flank of Mount Washington, in northern New Hampshire (Lat. 44°15'38.87"N, Lon. 71°17'08.76"W). The lake has an elevation of 1,031 m ASL (meters above sea level) and is a shallow water body with a maximum depth of roughly one meter. Hermit Lake was selected due to the relatively long meteorological observations record in the White Mountain region near Hermit Lake as well as a new lakeside meteorological station. In addition, there are ongoing phenology studies of the local ecosystem that include monitoring of a number of different amphibian species that reside around the lake including, wood frogs, green frogs, American toads, and spotted salamanders (Jones and Smyers 2010). According to Jones and Smyers (2008) these amphibians are part of the

only tundra-breeding amphibian population in the eastern United States and, as such, are susceptible to significant potential impacts from projected regional-scale climate change (IPCC, 2007). This amphibian population is one of the many reasons why it is important to study the air-water interaction for small-scale water bodies, like Hermit Lake.

b. Net heat flux

In order to understand the air-water interaction at Hermit Lake we must determine the net vertical heat flux of the lake. The net heat flux (Q_n) is a combination of four principle heat flux components and can be calculated via:

$$Q_n = Q_i + Q_{b_{net}} + Q_s + Q_e \quad \textbf{(1)}$$

where Q_i is the shortwave (incident) heat flux, $Q_{b_{net}}$ is the net longwave (blackbody) heat flux, Q_s is the conductive (sensible) heat flux, and Q_e is the evaporative (latent) heat flux (Pickard and Emery 1982). Each of these terms are in turn complex functions and are discussed below. Positive heat flux values indicate a heat gain into the lake while negative values indicate a heat loss from the lake. Only a basic discussion of the four heat flux equations will be given here. For a more in depth and technical discussion of each individual heat flux equation and their associated uncertainties, please refer to Appendix A.

c. Incident heat flux

The incident heat flux is given by:

$$Q_i = (1 - Ab)I_{sw} \quad \textbf{(2)}$$

where Ab is the water-surface albedo (unitless) and I_{sw} is the measured incoming shortwave radiation ($\mathrm{W\ m^{-2}}$) (Rogers *et al.* 1995). The intensity of Q_i is highly dependent on the amount of scattering produced by the atmosphere and the altitude of the

sun, which are accounted for when measuring I_{sw}, as well as the amount of sunlight reflected by the water surface (Ab) (Rizzi 2008). According to Pickard and Emery (1982), based on long-term world area radiational averages, the incident heat flux tends to dominate the contribution to the net heat flux in terms of a net gain. This finding can also be seen in past air-water studies (Beardsley *et al.* 1998; Miller 1999; Reed and Stabeno 2001; Churchill and Kerfoot 2007).

d. Blackbody heat flux

According to Budyko (1974) and Churchill and Kerfoot (2007), the blackbody heat flux is given by:

$$Q_{b_{net}} = Q_{b_1} + Q_{b_2} + Q_{b_3} \quad \textbf{(3)}$$

where Q_{b_1} is a downwelling term and is therefore a heat gain for the lake. Q_{b_2} and Q_{b_3} are upwelling terms and therefore each represent a heat loss for the lake. Q_{b_1} is given by:

$$Q_{b_1} = \varepsilon\sigma T_s^4 (0.05e^{0.5}) B_C \quad \textbf{(3.1)}$$

where ε is the emissivity of the water-surface (0.985), σ is the Stefan-Boltzman constant (5.673 x 10^{-8} W $m^{-2}K^{-4}$), T_s is the surface water temperature (Kelvins), e is the vapor pressure (millibars), and B_C is the cloud correction factor (Churchill and Kerfoot 2007). Q_{b_1} represents a gain of heat within the lake due to downwelling long-wave radiation from water vapor at or near the water surface (Figure 1). When the surface water temperature (T_s) increases, the water vapor increases due the latent heat released by the water surface. The water vapor near the water surface acts to absorb any incoming blackbody radiation as well as emitted blackbody radiation by the water surface. The

vapor then remits the blackbody radiation back down to the water surface, with a portion of the radiation escaping into the atmosphere above.

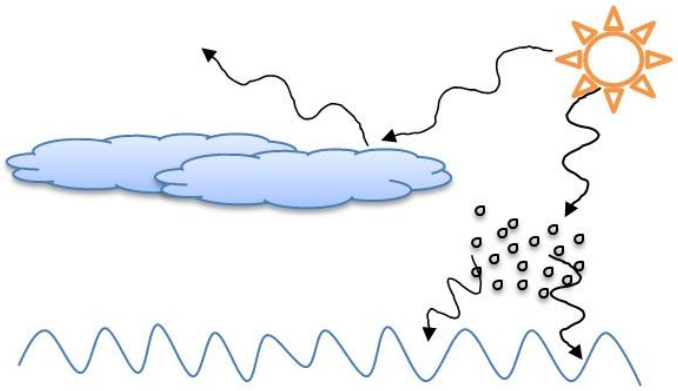

Figure 1. Graphical description of the processes in Q_{b_1}. The blue line is the water surface, the black lines represent longwave radiation, and the black droplets represent the water vapor in the air.

Q_{b_2} is given by:

$$Q_{b_2} = -\varepsilon\sigma T_s^4 (0.39) B_C \tag{3.2}$$

where ε is the emissivity of the water-surface, σ is the Stefan-Boltzman constant, T_s is the water-surface temperature (Kelvins), and B_C is the cloud correction factor. The 0.39 value is a statistically derived coefficient determined by M. E. Beriland (Budyko 1974). Q_{b_2} represents an overall loss of heat from the lake, but a portion of this loss is negated by the cloud cover. As cloud cover increases, the cloud cover coefficient decreases. This in effect acts to decrease the loss of heat from the lake by reflecting any emitted blackbody radiation from the water back down to the water surface. However, if the cloud cover is at a minimum, then the value of B_C increases as does the loss of heat associated with Q_{b_2}. According to Pickard and Emery (1990), the increased loss of heat by blackbody radiation in clear sky conditions is attributed to the water vapor content of the atmosphere. The longwave radiation emitted by a water surface ranges from 8 to 13

μm. The water vapor content of the atmosphere is relatively transparent to radiation within the given wavelength range. When clouds are present, the longwave radiation is effectively blocked and reemitted to the surface with some of the radiation passing through the clouds and emitted into the upper atmosphere (Figure 2). According to Rizzi (2008), the effects of blackbody radiation are most pronounced on cloudy days and often produce the greatest sources of heat at the lake water surface.

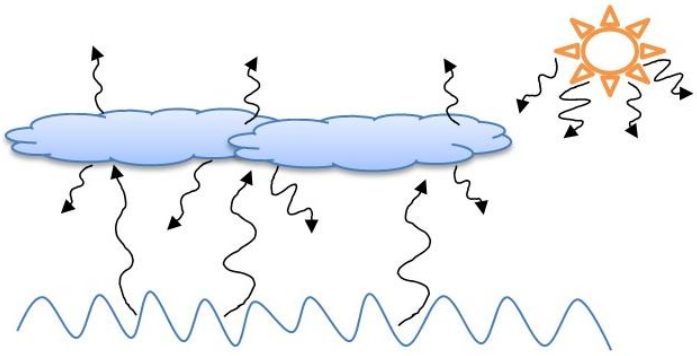

Figure 2. Graphical description of the processes in Q_{b_2}. The blue line is the water surface and the black lines represent the longwave radiation.

The final term in the blackbody radiation equation (Q_{b_3}) is given by:

$$Q_{b_3} = -4\varepsilon\sigma T_s^3(T_s - T_a) \tag{3.3}$$

where ε is the emissivity of the water-surface, σ is the Stefan-Boltzman constant, T_s is the water-surface temperature (Kelvins), and T_a is the air temperature above the water surface (Kelvins). Q_{b_3} is also considered an upwelling term and is therefore a heat loss for the lake. Here the loss is strictly driven by the temperature gradient between the water-surface temperature and the air temperature above the lake. As the difference in the vertical temperature gradient increases ($T_s > T_a$), the loss of heat by the lake increases. Inversely, the larger T_a is than T_s, the more heat is being gained by the lake.

The combined blackbody heat flux equation would look like the original blackbody equation (Equation 3.4) developed by M. E. Beriland (Budyko 1974).

$$Q_{b_{net}} = \varepsilon\sigma T_s^4(0.05e^{0.5} - 0.39)B_C - 4\varepsilon\sigma T_s^3(T_s - T_a) \quad \textbf{(3.4)}$$

Alone (3.4) is a very complex equation, therefore to understand how the blackbody equation actually operated, (3.4) was simplified to look like Equation 3. This simplification created an easier interpretation of the individual forces at work within the blackbody radiation equation. For a more in depth discussion of Equation 3.4, please refer to Budkyo (1974).

e. Sensible heat flux

According to Miller (1999), the sensible heat flux through a water-surface is given by:

$$Q_s = -\rho_a c_p C_S(T_s - T_a)W \quad \textbf{(4)}$$

where ρ_a is the density of moist air (kg m^{-3}), c_p is the specific heat coefficient of moist air at a constant pressure (J kg^{-1} K^{-1}), C_S is the sensible heat transfer coefficient (Stanton number), T_s and T_a are the temperatures of the water-surface and the air immediately above the water surface (Celsius), and W is the wind speed ($m\ s^{-1}$). This equation accounts for the conduction of heat through the air above the lake and the water itself. Keep in mind that heat is always conducted down a temperature gradient from higher temperatures to lower temperatures (Wallace and Hobbs 2006), therefore when the air temperature is greater than the water surface temperature Q_s will represent a heat gain (positive value). The opposite is true when the water surface temperature is greater than the air temperature. According to Pickard and Emery (1990), the rate of heat loss or gain is proportional to the strength of the vertical temperature gradient.

f. Latent heat flux

The final term in the net heat flux equation is the latent heat flux, which is given by:

$$Q_e = -\rho_a L_V C_e (q_s - q_a) W \quad \textbf{(5)}$$

where ρ_a is the density of moist air (kg m^{-3}), L_V is the latent heat of vaporization (J kg^{-1}), C_e is the evaporative heat transfer coefficient (Dalton number), q_s and q_a are the specific humidities at the water-surface and the air immediately above the water-surface, and W is wind speed (m s^{-1}) (Miller 1999). Typically Q_e is considered a loss term due to evaporational cooling, especially when dealing with dry air masses. When a moist air mass is present the loss is held to a minimum and can even represent a gain of heat in some cases (Pickard and Emery 1990). This process can be depicted in examining Equation 5. When q_s is greater than q_a, this implies that there is a greater amount of water vapor being transferred to the air above the water surface and therefore evaporational cooling is taking place. Inversely, if q_a is greater than q_s, heat is being transferred to the water-surface by way of condensation.

g. Summary

The combination of all four heat flux terms discussed above contributes to the net heat flux (Q_n) in Equation 1. It is important to examine how the net heat flux contributes to Hermit Lake in regards to a net heat gain or loss. Whether the lake is gaining or losing heat is an important factor when examining the ecology and biology of the plants, amphibians, and other living organisms in and around Hermit Lake.

A plethora of heat flux research exists for the world's oceans and larger water bodies, such as the Gulf of Maine (Miller 1999), owning to the net heat flux of the larger

water bodies importance in determining global climate factors such as global temperature changes (Miller 2011; personal communication). Heat flux research on small, shallow lakes such as, Hermit Lake, is not new, but access to year-round, on-site observations for local, observation-based heat flux calculations and application of that data to phenology and ecosystem monitoring is relatively novel, especially for alpine environments.

h. Basic physical limnology

According to Rizzi (2008), the vertical water column of a lake is separated into three layers: epilimnion, metalimnion, and hypolimnion. The epilimnion is the upper portion of the lake that is in direct contact with the air above it. This direct contact with the air above allows the layer to quickly heat or cool and is also less dense than the deeper waters. The metalimnion or thermocline is where the largest vertical temperature gradients occur within a lake. This layer is normally defined as the region where a temperature change of at least 1°C per meter of depth occurs (Rizzi 2008). Depending on the time of year or depth of the lake, certain weather patterns can lower the thermocline such as a passing cold front and its associated rain storms. If there is a great deal of solar heating occurring at the surface of a lake, the thermocline will rise. For example, during the summer time, the thermocline is generally higher in depth within a given lake due to solar heating. Once the season begins to transition to fall, solar heating becomes less and the epilimnion begins to cool. This cooling forces the thermocline to sink and eventually overturn within the deepest and coldest part of the lake, the hypolimnion. This overturning produces what is known as mixing.

Mixing is defined as when the entire vertical water column of a lake, is of the same temperature. These events can occur due to solar heating or very cold air masses,

water currents, and wind. Mixing events erode the density differences within the three layers of a lake, which allows for the vertical water column to have a nearly constant water temperature throughout. If no mixing is occurring and all three layers have different water temperatures, then the water column is stratified. Even if stratification is occurring, strong winds or currents could essentially still mix the top two layers and form a well-mixed epilimnion (Rizzi 2008).

i. Literature review

1) MILLER (1999)

Miller (1999) examined the air-sea interaction in the Gulf of Maine in response to heat flux changes during the 1997-1998 winter season. The main objective was to determine how changes in the net heat flux of the Gulf of Maine affected the formation of Maine Winter Water. Utilizing meteorological observations over a 635-hour period from moored buoys in the Gulf of Maine, Miller was able to determine that the largest heat losses were associated with the passage of a low pressure system and the subsequent arrival of a cold high pressure system.

In terms of the individual heat fluxes, the greatest loss of heat was associated with the latent (Q_e) and sensible (Q_s) heat flux terms. The latent heat flux was responsible for a total loss of 19.5 x 10^7 J m^{-2} of heat from the Gulf of Maine while the sensible heat flux was responsible for a total loss of 8.3 x 10^7 J m^{-2} of heat. It is interesting to note that Miller (1999) discovered that the maximum losses of heat associated with Q_e occurred approximately five-hours after the passage of a cold front. The maximum losses in heat associated with Q_s occurred approximately 15-hours after the passage of a cold

front. Overall the net heat flux for the Gulf of Maine during the 635 hour observational period represented a loss of 23.5 x 10^7 J m^{-2} of heat from the water body.

2) BEARDSLEY *et al.* (1998)

Surface net heat flux and the four individual heat fluxes were estimated for the northern California shelf during two separate experiments. The first occurred from 1981 – 1982 during the Coastal Ocean Dynamics Experiment (CODE) and the second occurred from 1988 – 1989 during the Shelf Mixed Layer Experiment (SMILE). Each experiment focused on heat fluxes from the early winter season through the summer. This timeframe allowed for examination of seasonal variations within the heat fluxes as well as the effect of synoptic events.

Each experiment presented with similar results in terms of largest contributors to the net heat flux of the northern California shelf. The incident heat flux (Q_i) was the largest mean component, followed by Q_b. Q_e and Q_s were weaker, but of the same magnitude. During the winter season of both experiments the mean net heat flux value was roughly -9 W m^{-2}. Losses in Q_b negated almost any gains associated with Q_i which allowed the net heat flux to be dominated by the latent and sensible heat fluxes. During the winter season, low air temperatures coupled with low relative humidities resulted from offshore advection of cold, dry continental air. This advection was due to the passage of high- and low-pressure systems which is consistent with findings in Miller's (1999) study. The cold, dry air contributed to negative mean values of Q_e and Q_s and therefore the negative mean value of Q_n.

During the spring, Q_i dominated the net heat flux with a mean value of 189 W m^{-2}. Q_b and Q_e represented losses, but were an order of magnitude smaller than Q_i and

since Q_s was negligible, the net heat flux was an overall gain of heat with a mean value of 130 W m^{-2}. During the summer season the gain of heat by the net heat flux was even more amplified by the increase in Q_i to a mean value of 248 W m^{-2}. The other three heat fluxes' mean values remained relatively unchanged compared to the spring season.

3) CHURCHILL AND KERFOOT (2007)

The impact of the net surface heat flux on the thermal stratification in Portage Lake, Michigan was the focus of this study. Portage Lake is a much larger and deeper lake than Hermit Lake with a mean depth of approximately nine meters. Utilizing moored measurements within the lake and meteorological observations from a nearby airport, the individual heat fluxes were estimated from June 1998 through August 1999.

Just as was discovered in Beardsley *et al.'s* (1998) study, the seasonal variations in the net het flux (Q_n) were mainly driven by variations in the incident heat flux. During the course of the study several mixing events were observed. The weather patterns associated with these mixing events tend to resemble that of the passage of a low-pressure system and its associated cold front. Each mixing event corresponded to cold air outbreaks and cloudy sky conditions. The mixing events were also associated with negative net heat flux values, mainly due to minimum values of the incident heat flux and much larger losses within the latent and sensible heat fluxes.

j. Scientific question

This study uses observational data to calculate the four individual heat fluxes as well as the net heat flux at Hermit Lake. These fluxes will quantitatively answer questions that form the basis for this research.

1) How do all five air-water heat fluxes vary with time of day, time of year, and under varying meteorological conditions?
2) How does the total heat budget of Hermit Lake vary over the course of the study? At what times is the lake experiencing a net gain or a net loss of heat?
3) How is breeding within the local amphibian community at Hermit Lake affected by various meteorological conditions and the five heat fluxes?

CHAPTER 2

2. Data and Methodology

a. Total cloud cover

In order to calculate the incident heat flux Q_i, the water-surface albedo Ab, must be calculated (Rogers *et al.* 1995). For an unfrozen and frozen lake, the cloud cover (C) must be known so that the albedo and subsequently, Q_i can be computed. This created a problem for this research since there was no available cloud cover data from the Hermit Lake station. Therefore, the total cloud cover needed to be estimated.

Observed cloud cover data from a nearby station is used as an estimate of local cloud cover. The Mount Washington Summit Station, the only station with observed cloud cover data within a reasonable distance, is located approximately 1,985 m away from and 886 m above the Hermit Lake station. All data used throughout the course of this study is in 15-minute intervals, but the observed cloud cover data from Summit Station is hourly. In general, reducing cloud data from hourly to 15-minute intervals is not scientifically accurate nor advisable, especially for cumulus cloud cover. Fortunately, pyranometer data from the Hermit Lake station is available to help enhance the quality of the reduction.

With observed incoming solar radiation (I_{sw}) from the Hermit Lake pyranometer, a cloud cover error is calculated for each timestamp and each of the nine sets of cloud cover coefficients (a,b) (Lind and Katsaros 1986) using calculated clear-sky solar radiation (I_{sw_0}), and calculated solar elevation angles (θ):

$$\varepsilon = \left| \left(\frac{I_{sw}}{I_{sw_0}} - a \right) - (b \cos(\theta)) \right| \quad \textbf{(6)}$$

Then, using the set of coefficients associated with the minimum error, a cloud cover category is assigned to each timestamp (Lind and Katsaros 1986). Each cloud cover category receives an estimated value for cloud cover of one (minimal cloud cover), four (moderate cloud cover), or seven (overcast) (eighths). The calculations mentioned above and the process of assigning cloud cover categories and estimated total cloud covers are performed with the PERL program, *cloudcover_est.pl*, found in the attached CD-ROM.

Conversion of observed cloud cover data from hourly to 15-minute intervals is accomplished with a weighting equation (6.1) :

$$TCC_{15min} \cong \frac{(OTCC_0)(w_0) + (ETCC)(w_E) + (OTCC_{60})(w_{60})}{w_0 + w_E + w_{60}} \quad \textbf{(6.1)}$$

where TCC_{15min} is the total cloud cover in 15-minute intervals, $OTCC_0$ is observed total cloud cover from the Summit Station at the top of the hour, w_0 is the weight for top of the hour cloud cover, $ETCC$ is the estimated total cloud cover calculated from the pyranometer data, w_E is the weight for the estimated cloud cover, $OTCC_{60}$ is observed total cloud cover from the Summit Station at the bottom of the hour, and w_{60} is the weight for bottom of the hour cloud cover. w_0 and w_{60} are determined using a linear process (Figure 3). For w_0, this term carries a weight of one at the top of the hour and linearly decreases to zero as time approaches the bottom of the hour. For w_{60}, this term carried a weight of zero at the top of the hour, but linearly increased to one as time approached the bottom of the hour.

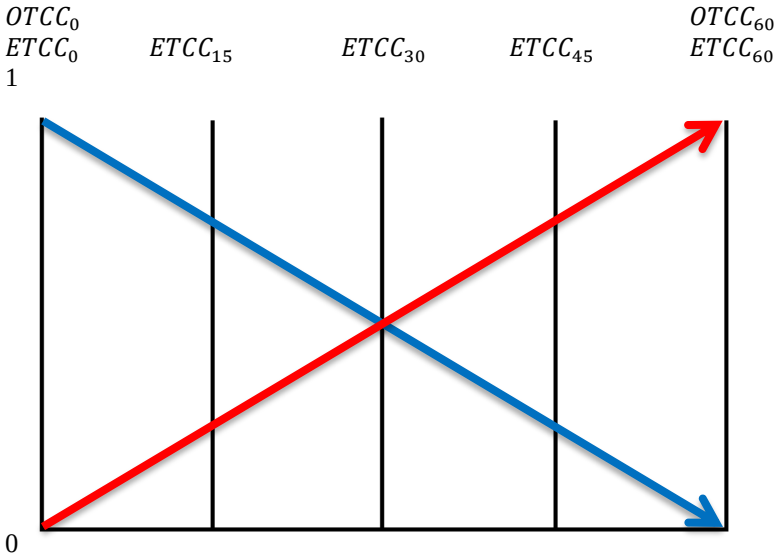

Figure 3. Depiction of how w_0 (blue) and w_{60} (red) are determined. The vertical axis is unitless and the horizontal axis is in minutes.

To determine w_E, the PERL script *cloudcover_est.pl* (CD-ROM) is used. The process of determining the estimated cloud cover was discussed above, but the observed cloud cover data is also needed in order to determine w_E. The observed cloud cover data obtained from Summit Station is recorded in percentages, which is converted to eighths using the following equation:

$$OTCC = \frac{OTCC_{\%}}{100} * 8 \tag{6.2}$$

Despite the conversion, a number of the cloud cover values did not equal either one, four, or seven (eighths). To rectify this problem, where original observed cloud cover values are zero or 1.6 (eighths), these are designated as one eighth (minimal cloud cover). Similarly, values of 3.6 (eighths) become four eighths (moderate cloud cover), and any other observed values are designated seven eighths (overcast). This process of data management gives estimated cloud cover the same scaling as observed cloud cover and allows for calculation of estimation error. To determine the error produced by using the estimated cloud cover values the following equation is utilized:

$$\varepsilon = OTCC - ETCC \tag{6.3}$$

Bulk statistics on the total dataset of errors (ε) (Table 1) determine the quality of the estimated cloud cover values compared to the observed hourly cloud cover values. Here, the two most important statistics are the standard deviation and the sum. A standard deviation of 3 indicates that, 65% of the time, the cloud cover category of the $ETCC$ is off by at least one category. A sum of 783 indicates that $ETCC$ underestimates actual cloud cover. One explanation for this is Hermit Lake's location 886 m below the summit of Mount Washington. Summit Station can be, and often is, completely overcast, when Hermit Lake is not.

Table 1. Bulk statistics of $\boldsymbol{\varepsilon}$

Max	6
Min	-6
Mean	0.5039
Std. Dev	3.0519
Sum	783

The calculated errors for $ETCC$ enable a weighting system for w_E. Since $ETCC$ underestimates actual cloud cover, the weighting function is equal to zero at the top of the hour and linearly increases to 0.5 at the half hour mark. After this point, w_E linearly decreases until it becomes zero again at the bottom of the hour (Figure 4). This process is necessary to ensure that w_E carries the same weight at 30 minutes as w_0 and w_{60} carry at the top of the hour or bottom of the hour.

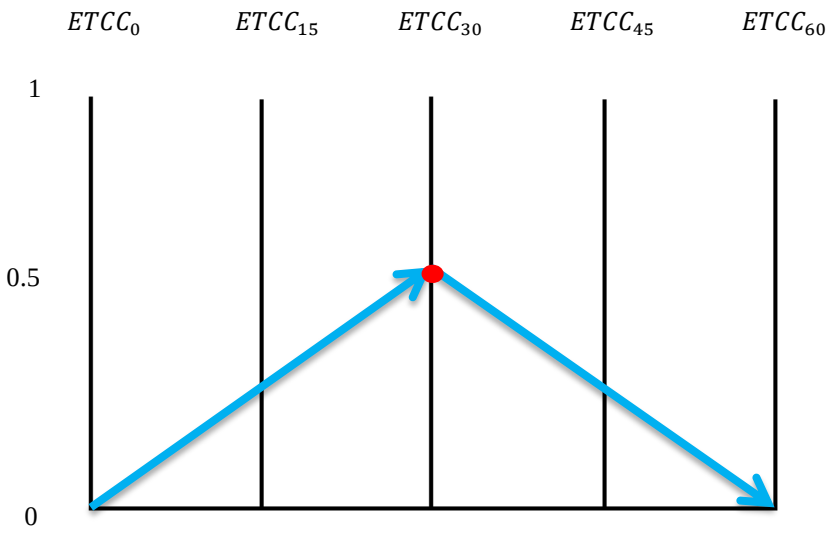

Figure 4. Depiction of how w_e is determined. The vertical axis is unitless and the horizontal axis is in minutes.

With observed total cloud cover modified to 15-minute intervals, the cloud cover values were designated one, four, or seven (eighths). This process ensures that the resolution of the final product is no better than the input values. Albedo (Ab) is then computed for an unfrozen lake using the final values of TCC_{15} for C.

b. Surface water temperature

Hermit Lake is a shallow lake with a maximum of depth of approximately one meter. An offshore, sub-surface mooring of three HOBO Pro v2 Water Temperature Data Loggers monitors water temperature, with a ± 0.2°C accuracy and 5 minute resolution, at the surface, at 50 cm, and at 100 cm depth (Doner 2011). Useable surface temperature data includes six days at the end of May, 2010 and also the interval from the beginning of July 2010 to the beginning of November 2010 (Figure. 5).

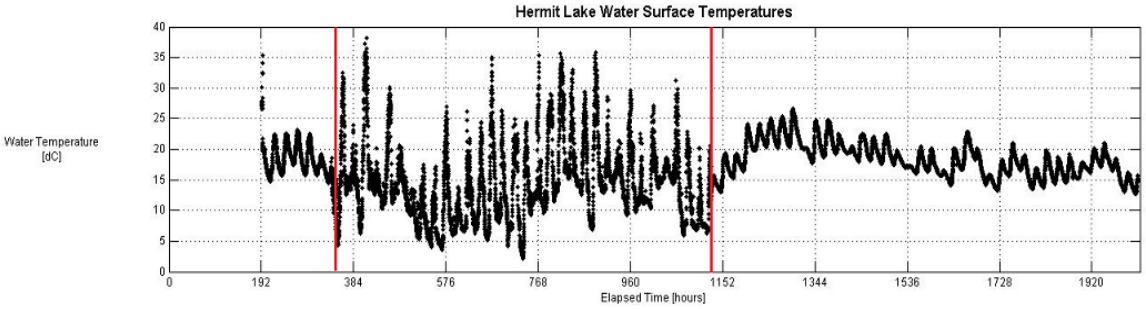

Figure 5. Original surface water temperature series [°C] for Hermit Lake from 201005241710 GMT to 201008081550 GMT. Data between the red lines is unusable data.

On May 30, 2010 at 1705 GMT, a strong wind flipped the surface buoy making the surface water temperature sensor into an impromptu air temperature sensor and creating a gap in the surface water temperature dataset. On July 2, 2010 at 1510 GMT the buoy was repaired and the surface water temperature record restarted. These events, and the resulting change in the data, are indicated in Figure 5 by two red lines. To fill the need for the missing water surface data, a synthetic temperature series is derived.

To develop the synthetic water surface temperature series, the 50 cm water temperatures are used. The 50 cm temperatures were not affected by the flipping of the buoy and therefore provide meaningful insight to how the surface temperatures would have appeared had the buoy not flipped. To do this, the longest useable portion of the surface temperatures from July 2, 2010 at 1515 GMT to November 7, 2010 at 0330 GMT is compared to the 50 cm temperatures for the same time interval. The data, originally in five-minute intervals, is reduced to 15-minute intervals (time interval used throughout research). A simple two-sided triangular filter was applied to each series using the toolkit AIRSEA within the computer program MATLAB (Miller 2011; Mathworks 2010). Linear regression using a first-order fit of both datasets appear in Figure 6 and Table 2. The red line is the fitted line created by the linear regression analysis.

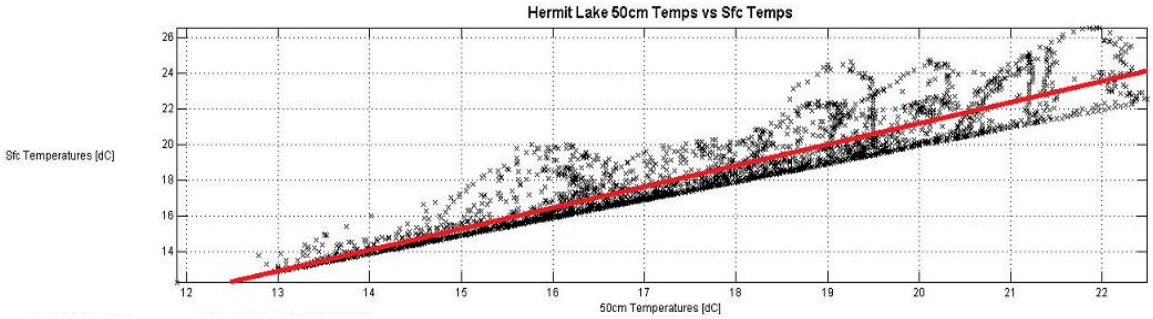

Figure 6. Results of the linear regression performed on the 50 cm and surface water temperatures. The red line marks the line of best fit.

Table 2. Statistical results for the red line y = a + bt in Figure 6.

$\boldsymbol{\sigma^2}$	1.106
$\mathbf{R^2}$	0.859
a	-2.499
b	1.183

A variance (σ^2) of 1.106 (Table 2) means that surface water temperatures are accurately estimated by the 50 cm temperature record, to within ~ 1 °C. The high value for the coefficient of determination (R^2) of 0.859 indicates that the linear regression is a good fit and statistically meaningful. A y-intercept (a) of -2.5 and slope value near 1 indicates that, for any given 50 cm water temperature the surface water temperature is 2.5 °C cooler. These statistics suggest that a synthetic surface water temperature series derived from the 50 cm temperatures is sufficiently accurate for the purpose of this research.

The synthesized data is substituted for the missing surface water temperature (indicated in Figure 5) for May 26, 2010 at 1515 GMT to July 2, 2010 at 1515 GMT in the following manner. In the raw data file containing the 50 cm water temperatures, the

temperatures corresponding to the above timeframe are reduced to 15-minute intervals. Using AIRSEA, the slope equation developed during the linear regression analysis is applied to the relevant 50 cm temperatures (Equation 7):

$$T_s = a + (b * T_{50cm}) \tag{7}$$

where *a* (the y-intercept) and *b* (the slope) are found in Table 2. The synthesized surface water temperatures fill the gap in the surface temperature records. To ensure a smooth transition between synthetic temperatures and observed temperatures, three and half hours of temperature data are deleted and replaced with the missing data marker -999. This length of time was chosen because it provides the smoothest transition between the synthetic and observed temperatures. Figure 7 consists of two graphs, the bottom graph is the newly formed surface temperature series and the top graph is the magnified portion between the blue lines in the bottom graph. The magnified portion displays the break where the synthetic temperatures end and the observed temperatures begin.

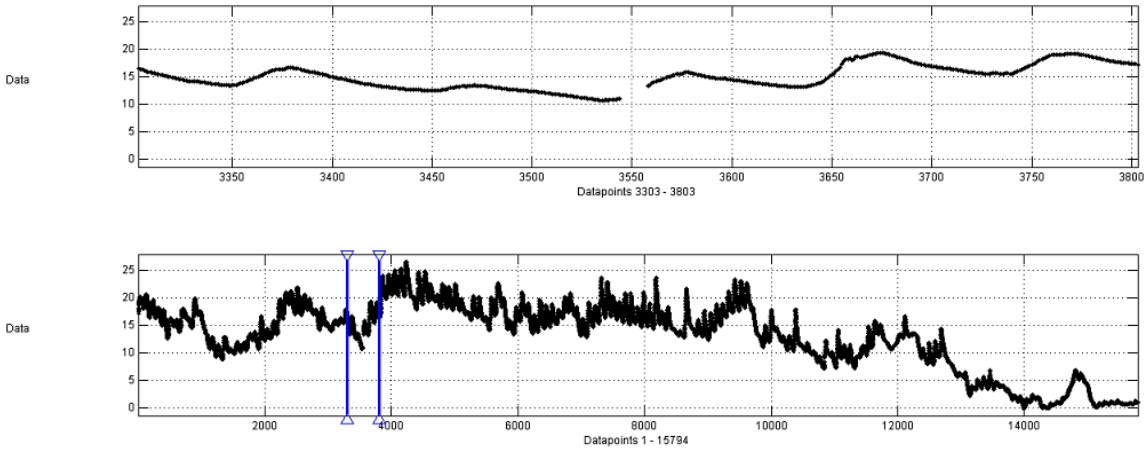

Figure 7. Final surface water temperature series for Hermit Lake. The bottom graph displays the new surface water temperature [°C] series while the top graph displays the magnified portion between the blue lines in the bottom graph. The magnified portion displays the break separating the synthetic temperatures from the observed temperatures.

Linear regression, using a first-order fit over a roughly four day period from May 26, 2010 at 1530 GMT till May 30, 2010 at 1630 GMT, of observed temperatures and synthesized temperatures helps demonstrate how well the synthesized surface water temperature series compares to actual observed surface water temperatures. This is the only timeframe containing both useable observed and synthetic surface water temperatures. The results of this linear regression appear in Figure 8 and Table 3. The red line marks the fitted line created by the linear regression analysis. From the statistical and graphical results it appears that the linear fit is not as good as one would hope, but it is still useable for the purposes of this research. One very important note is that the y-intercept (a) indicates that when the observed water temperature is equal to 0 °C, the synthetic temperature is about 8 °C warmer. These results suggest that the synthetic temperatures tend to overestimate the actual water temperature. This can be explained by the air-water interaction at the water surface. Cooling by the air above the water may cool the surface water temperatures to below the 50 cm water temperature during the time period that contains the synthesized temperatures. Another possibility is the penetration of sunlight throughout the water column, which can also warm the 50 cm temperatures above the surface water temperatures. The overestimated values are nevertheless, acceptable and therefore the synthetic water temperature values can be used as a replacement for the missing surface temperature data.

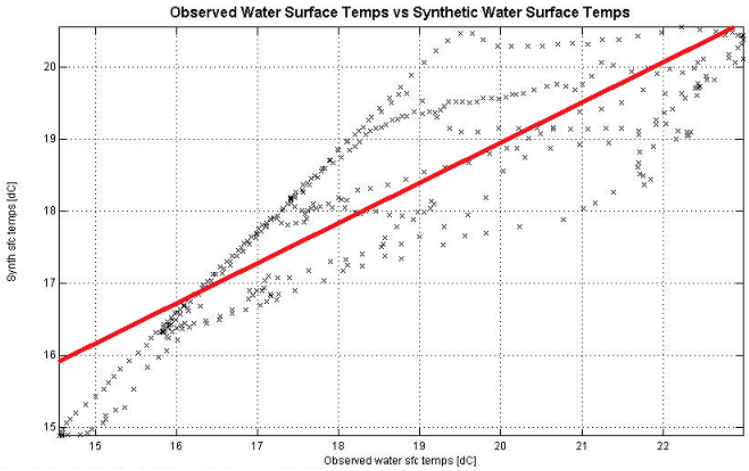

Figure 8. Results of the linear regression performed on the synthetic water temperatures and observed water temperatures. The red line marks the line of best fit.

Table 3. Statistical results for the red line y = a + bt in Figure 8.

$\boldsymbol{\sigma^2}$	0.508
$\mathbf{R^2}$	0.761
a	7.815
b	0.556

The final water surface temperature series contains temperatures from May 26, 2010 at 1515 GMT to November 7, 2010 at 0330 GMT. The data for 2010 ends abruptly on November 7, 2010 due to memory overflow by all three in-lake sensors.

c. Various important atmospheric variables

This section includes a discussion of the quality control methods performed to ensure that the air temperature, relative humidity, dew point temperature, incoming solar radiation, and wind speed data are suitable for input into the individual heat flux equations. Air temperature and relative humidity are recorded at the Hermit Lake station in one-minute intervals. Dew point temperature is not recorded at the station and is

needed in order to calculate the vapor pressure (e). Air temperature and relative humidity data are cleaned and reduced to 15-minute intervals using the toolkit AIRSEA within the computer program MATLAB (Miller 2011; Mathworks 2010). A degapping program performed on the relative humidity and air temperature files removes any gaps from missing timestamps. Next a point-to-point slope filter, applied to the relative humidity data removes any noticeable erroneous data points using a slope of 3% per minute. This allows for a maximum 3% change in humidity per minute. For slopes exceeding 3% per minute, the data point is designated with the missing/bad data marker (-999). No noticeable erroneous data points occur within the air temperature dataset therefore, no slope filter is applied. Missing data markers are linearly interpolated out of the datasets so that the "cleaned" versions do not contain any missing data. Finally, a two-sided triangular filter is applied to each dataset to reduce the data from one-minute intervals to 15-minute intervals.

Dew point temperatures are calculated with the AIRSEA toolkit (Miller 2011) using a form of the Clausius-Clapeyron equation. A few noticeable outliers within the dew point temperatures are smoothed out using a slope filter. To determine the slope of the filter, the original dew point temperature data set is visually inspected. Based on this inspection, the maximum allowed slope is selected as 1°C per 15 minutes.

The incoming solar radiation data recorded by the Apogee SP-110 Precision Pyranometer at Hermit Lake (Doner 2011) follows much of the same data filtering processes mentioned above. The dataset is first degapped then a point-to-point slope filter is applied to the series to smooth out any outliers. Incoming solar radiation data can be quite variable in response to cloud cover (Miller 2011, personal communication). This

means that large swings in observed solar radiation values can occur within a matter of minutes or even seconds. With this in mind and after a visual analysis of the solar radiation data, the maximum allowable slope is selected to be 600 W m^{-2} per minute. Any data marked by -999 is then linearly interpolated to create a complete dataset. A two-sided triangular filter is applied to the dataset to reduce the data's temporal resolution to 15-minute intervals.

Wind speed data is measured at Hermit Lake as a five-minute average. The same quality control and filtering processes are applied to the wind speed data, but with slightly different input for the filtering programs. No slope filter is applied to the data. Any missing/bad data markers are linearly interpolated and the wind speed data is reduced from five-minute intervals to 15-minute intervals via the two-sided triangular filter.

d. Albedo

The albedo, or the amount of sunlight reflected by the lake water surface is not directly measured at Hermit Lake, but is necessary to fully calculate the incident heat flux (Q_i). Utilizing Equation A2.7 for a water body of infinite depth (Ab_∞), and Equation A2.9 for a water body of finite depth (Ab) (Albert and Mobley 2003), found in Appendix A and the PERL program *heatflux_calcs.pl* (CD-ROM), the albedo is calculated.

Due to missing data in the cloud cover dataset, the albedo for Hermit Lake is only calculated for intervals when there is usable cloud cover data. If there are missing cloud cover data for the time of the albedo calculation, the albedo (Ab) is not calculated and is assigned a missing data marker of -999. During the timeframe of this study, 69% of the albedo data is usable based on available cloud cover data.

The albedo equations developed by Albert and Mobley (2003) require the use of the solar zenith angle (Z). For this research the solar elevation angle was originally calculated via the toolkit AIRSEA within the computer program MATLAB (Miller 2011; Mathworks 2010). To convert from a solar elevation angle to a zenith angle, simply subtract θ from 90. This conversion changes the coordinate system for the angle at which the sun is above the horizon. When the sun is directly overhead of the lake surface, the zenith angle is equal to 0°. Subsequently, when the sun is directly on the horizon, the zenith angle is equal to 90°. As the sun sets below the horizon, the zenith angle becomes greater than 90°. Note that for both Equations A2.7 and A2.9 in Appendix A, these equations divide by the cosine of the zenith angle. From basic trigonometry, it is known that the cosine of 90° is zero and the cosine of 0° is one. As the sun approaches the horizon, the albedo increases, and as the sun approaches directly overhead of the lake, the albedo decreases. A further discussion of the albedo behavior can be found in Chapter 3.

The conversion from solar elevation angle to solar zenith angle, creates zenith angles that exceed 90°. When the sun is below the horizon (90°), albedo is negligible. Therefore albedo for zenith angles exceeding 90° is assumed to zero. This step prevents any erroneous albedo values within the final incident heat flux calculations. Test calculations to determine if the PERL program performs the calculations correctly reveal some Ab_∞ values of greater than one. The albedo of any surface is a unitless value ranging between zero (no reflection) and one (100% reflection) and cannot drop below zero nor can it exceed one (Rogers *et al*. 1995). The errors all occur when zenith angles are close to 90°. To fix these errors, the value of Ab_∞ is capped at 0.9999, if it exceeds one. Once the values of Ab_∞ are capped the values of Ab behave reasonably well.

e. Frog calling intensity

As part of an ongoing, corollary project, with Scott Smyers, Oxbow Associates, Acton, MA, frog calls indicative of breeding activity, are monitored at Hermit Lake. With permission, the results of this project for 2010 are summarized here.

The recordings last for a half an hour, and begin one hour after sunset. The frog call record extends from May 26, 2010 to August 16, 2010 and identifies four different frog species. Those species are the spring peeper (*Pseudacris crucifer),* wood frog (*Lithobates sylvaticus*), American toad (*Anaxyrus americanus*), and green frog (*Lithobates clamitans*) (Smyers and Jones 2008; Smyers 2011; personal communication). Table 4 displays the number of days that each frog species was actively calling during the 83 day recording period. The wood frog is highlighted in red because there is a lack of data regarding calling activity from this species. Therefore, the focus of this portion of research will be directed towards the activity of the spring peeper, American toad, and green frog. Frog calling activity is split into four categories as defined by the North American Amphibian Monitoring Program (NAAMP).

These categories are as follows (Cook *et al.* 2010; Smyers 2011; personal communication):

0 = No frog calling activity was recorded.
1 = Individual frog species can be counted, there is space between calls.
2 = Calls of individual species can be distinguished, but there is some overlapping.
3 = Full chorus. Calls are constant, continuous, and overlapping.

Therefore, an actively calling day is one which has a corresponding calling category of 1, 2, or 3.

Table 4. Number of actively calling days (N) for each frog species during the 83 day recording period.

Frog Species	N (# of actively calling days)
Spring peeper	57
Wood frog	6
American toad	19
Green frog	26

In order to quantify the relationship between this monitored data and environmental conditions, this frog sound data is compared to datasets for air temperature, surface water temperature, wind speed, and the five individual heat flux summations associated with the beginning of each night's 30 minute recording period. To perform these comparisons, the time of sunset is determined from the calculated solar elevation angles mentioned in section *d.* The time of sunset for each day is determined and the the initial hour is set ahead one hour to match with the beginning of the 30 minute recording period. With these date timestamps, the associated meteorological data is pulled to create eight new time series to compare with the frog sound data. This entire process is performed using the PERL script *frog_hr.pl*, found in the attached CD-ROM.

Linear regressions are performed for each series, using MATLAB and the AIRSEA toolkit (Miller 2011; Mathworks 2010), with the meteorological data set as the independent variable and the frog sound data set as the dependent variable. A complete display of the linear regression results can be found in Appendix B. Relevant linear regression results pertaining to the spring peeper, American toad, and the green frog are discussed further, in Chapter 3.

CHAPTER 3

3. Results

The following results derive from data series reduced or interpolated to a 15-minute resolution, from their original one-minute, five-minute, or one hour resolutions.

a. Water temperature

Cleanup and partial synthesis of the water temperature data discussed in Chapter 2, section *b*, produces a surface temperature series (Figure 9) useful for this research. The series begins on May 26, 2010 at 1515 GMT and ends on November 7, 2010 at 0330 GMT. The length of this series in 2010 determines the period of study. The synthesized water surface temperatures occur at the beginning of the temperature series and end on July 2, 2010 at 1300 GMT (marked by the red line). Three and a half hours later, the observed temperatures begin.

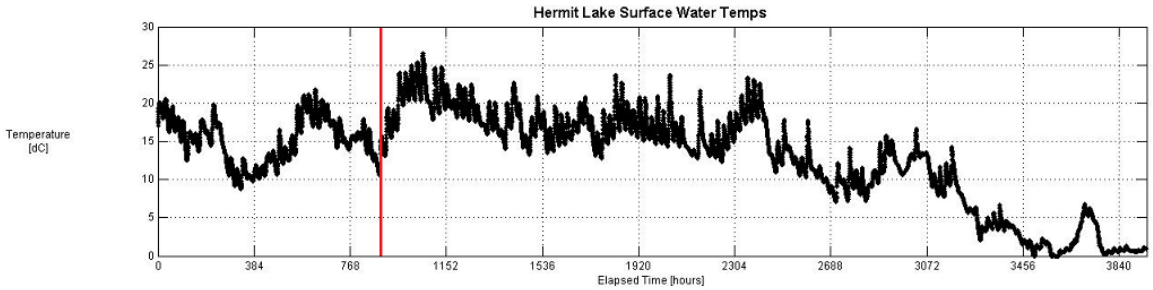

Figure 9. Water surface temperature [°C] series for Hermit Lake beginning 201005261515 GMT and ending 201011070330 GMT. The red line marks where synthesized temperatures end and where observed temperatures begin. The x-axis marks the elapsed time in hours and the y-axis marks the water temperature in degrees Celsius.

Figure 9 shows a high amount of variability in the surface water temperatures. This is expected for surface water since it is in direct contact with the airmass above. Also, as the air temperature cools with the onset of fall, the surface water temperature decreases as well. This decrease compares quite well with the decrease in air temperature, discussed below.

Figures 10 and 11 display the water temperature series for Hermit Lake at a depth of 50 cm and 100 cm, respectively. Variability in these temperatures decrease as depth increases. Increases and decreases in surface temperature are represented in the 50 cm 100 cm temperature series, but to a lesser degree. Throughout the water column, temperatures are warm from late spring through summer, but decrease rapidly as the season transitions into fall.

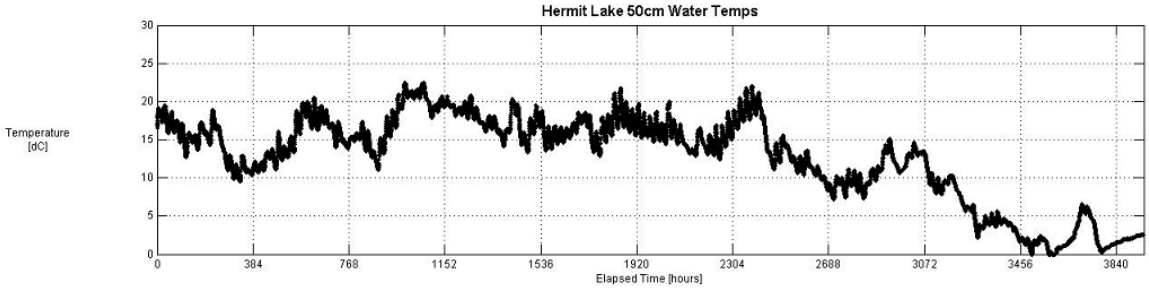

Figure 10. 50 cm water temperature [°C] series for Hermit Lake beginning 201005261515 GMT and ending 201011070330 GMT. The x-axis marks the elapsed time in hours and the y-axis marks the water temperature in degrees Celsius.

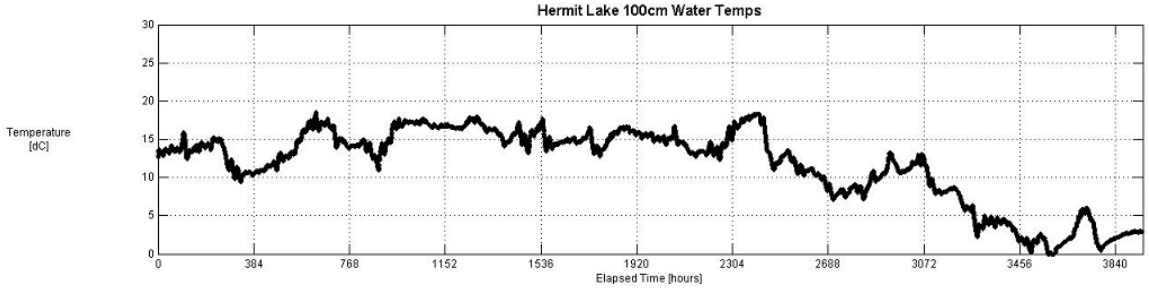

Figure 11. 100 cm water temperature [°C] series for Hermit Lake beginning 201005261515 GMT and ending 201011070330 GMT. The x-axis marks the elapsed time in hours and the y-axis marks the water temperature in degrees Celsius.

Bulk statistics computed for each series provide statistical insight to how the three water temperature series compare (Table 5). The differences between the series' statistics make physical sense. The water surface maximum temperature and the mean temperature are warmer than the 50 cm and 100 cm maximum and mean temperatures. The standard deviation of 6.128 for the surface water shows a higher degree of variability than for the 50 cm and 100 cm temperatures. These differences in relative variability are due to the

surface water's direct interaction with the airmass above which allows it to react quickly to fluctuations in air temperature. The effects of the air temperature's forcing on the surface water temperature over time are transmitted to deeper depths, but to a lesser degree.

Table 5: Bulk statistics for water surface, 50 cm, and 100 cm temperatures [°C]

	Surface	**50 cm**	**100 cm**
Max	26.543	22.486	18.500
Min	-0.159	-0.048	-0.060
Mean	13.052	12.785	11.752
Mode	17.200	17.200	16.700
Std. Dev.	6.128	5.695	4.929

Cross correlation analysis performed on the surface water temperatures and the 50 cm water temperatures shows an approximately one hour and 15 minute lag between surface water temperature forcing and temperature response at 50 cm. In other words, if the surface water warms by one degree Celsius, it will take roughly one hour and 15 minutes for the 50 cm temperatures to warm. Cross correlation of air and surface water temperatures reveals an approximately two and a half hour lag between atmospheric forcing and response in the surface water temperatures.

b. Air temperature

Figure 12 and Table 6 display the graph and statistics associated with air temperature for the period of interest from the Hermit Lake station. Visual comparisons of Figures 9-12 reveal that observed variations in the air temperature directly above the

water surface are reflected throughout the water profile. The variability in the air temperature is slightly higher than the water temperature, due to differences in specific heat between air and water.

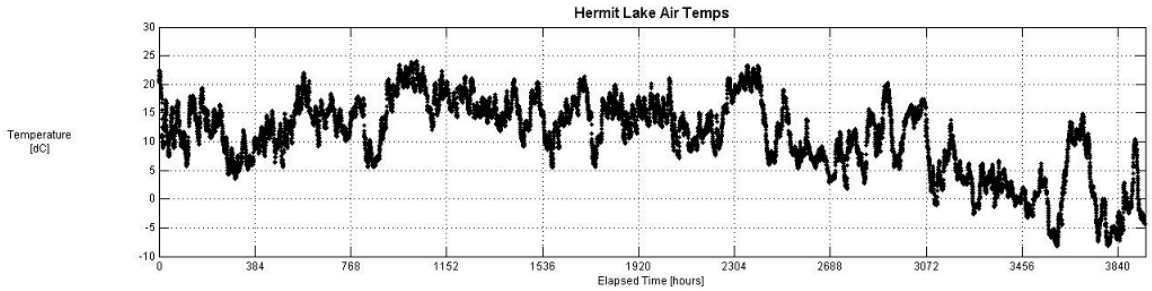

Figure 12. Air temperature [°C] series for Hermit Lake beginning 201005261515 GMT and ending 201011070330 GMT.

Table 6. Bulk statistics for air temperature [°C]

Max	24.026
Min	-8.245
Mean	10.925
Mode	9.722
Std. Dev.	6.669

One questionable statistic however is that the air temperature maximum is about two degrees Celsius less than the maximum temperature for the water surface. This is not a product of the synthetic temperature series; the maximum surface water temperature occurs within the *observational* data series. One explanation is that incoming radiational heat fluxes have more influence on warming of water temperature than on that of air temperature. A second hypothesis is that weather band contributions, atmospheric changes due to the passage of frontal and/or pressure systems, are responsible. These ideas are tested by power spectrum analysis on the differences between surface water

temperatures and air temperatures, using the toolkit AIRSEA, within the computer program MATLAB (Miller 2011; Mathworks 2010). The power spectrum analysis searches for peaks in the series above the 95 percent confidence level. If the radiational heat flux theory is true, a diurnal (every 12 hours) signal will exist in the series of peaks. If the weather band hypothesis is true, there will be a series of significant peaks every 3 to 4 days, the time it takes for frontal and/or pressure systems to affect a region (Miller 2011, personal communication). A lack of significant peaks, however, leads to rejection of both of these hypotheses. An alternative explanation is that microenvironmental differences between the location of the air temperature and water temperature sensors are greater than assumed. The air temperatures are measured about 2 m (6 ft) above the roofline of the Hermit Caretaker Shelter; and about 5 m (15 ft) off the ground. The Hermit Lake monitoring buoy is about 150 m (450 ft) away and about 25 m (75 ft) lower in elevation than the air sensors. Unfortunately, the time constraints of this study limit further research on this matter.

c. Dew point temperature

The dew point temperature series (Figure 13) and associated statistics (Table 7) show that as expected the maximum dew point temperature is less than the maximum air temperature. Once the season begins to transition into late fall/early winter, the dew points cool fairly rapidly. Late fall is where the minimum of -19.437 °C (Figure 13).

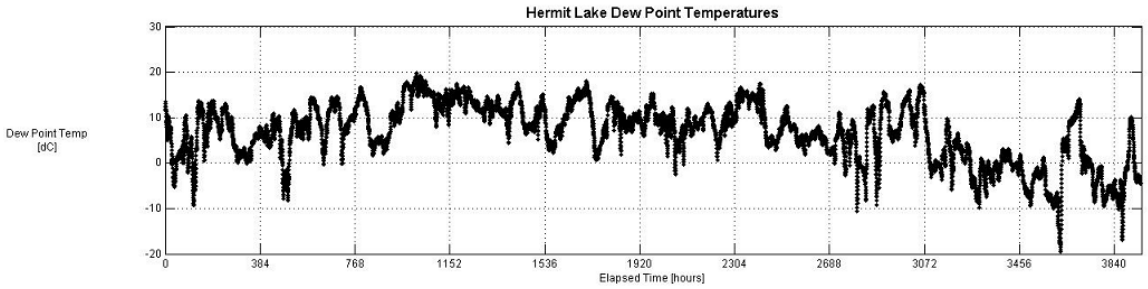

Figure 13. Dew point temperature [°C] series for Hermit Lake beginning 201005261515 GMT and ending 201011070330 GMT.

Table 7. Bulk statistics for dew point temperature [°C]

Max	19.846
Min	-19.437
Mean	6.715
Mode	-1.420
Std. Dev.	6.466

d. Incoming shortwave solar radiation

An Apogee SP-110 Precision Pyranometer measures incoming solar radiation at the Hermit Lake Station (Doner 2011) (Figure 14; Table 8). The statistical results are what is typical with a minimum value of zero (no incoming shortwave radiation at night). Zero is the most often repeated value, as shown by the mode. Sunshine is highly variable, indicated by the high standard deviation of ~ 248 W m^{-2}. Northern New Hampshire, where Hermit Lake is located, is typically a cloudy environment with cloudy skies more than 200 days per year (Figure 15). This is especially true during late fall and through the duration of winter (NCDC 2011). At Hermit Lake, the steady decrease in incoming solar

radiation after the onset of fall is explained by the increase in cloudy conditions and seasonal decreases in solar elevation angle (Figure 14).

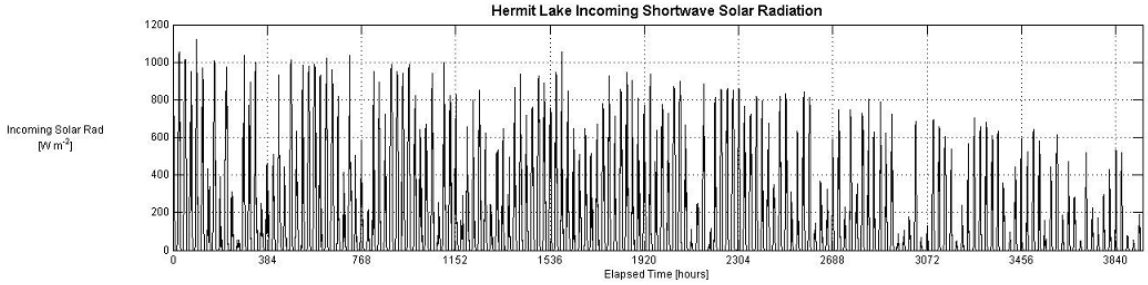

Figure 14. Incoming solar radiation [W m^{-2}] series for Hermit Lake beginning 201005261515 GMT and ending 201011070330 GMT.

Table 8. Bulk statistics for incoming solar radiation [W m^{-2}]

Max	1123.581
Min	0
Mean	152.288
Mode	0
Std. Dev.	241.408

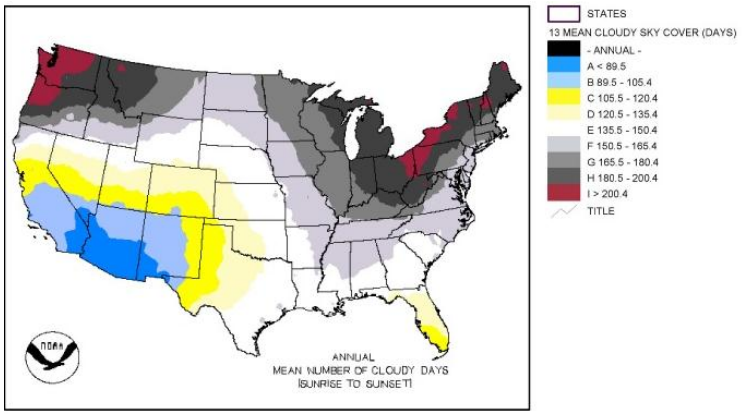

Figure 15. Annual mean number of cloudy days from 1961 to 1990 (NCDC 2011).

e. Wind speed

The wind speed data used for this study is originally measured as five-minute averages. The statistics (Table 9) and graph (Figure 16) reflect averages rather than instantaneous wind speeds. Of note is the higher wind speeds recorded near the end of the series, in late October, early November (Figure 16). This is most likely the result of the increasing strength and frequency of synoptic-scale low pressure systems that occur in the fall as the polar jet strengthens and pushes south, and as the sub-tropical ridge weakens and becomes suppressed. Visual inspection of air temperatures (Figure 12) and wind speeds (Figure 16), reveal that large decreases in temperature in late October and early November match times of higher wind speeds.

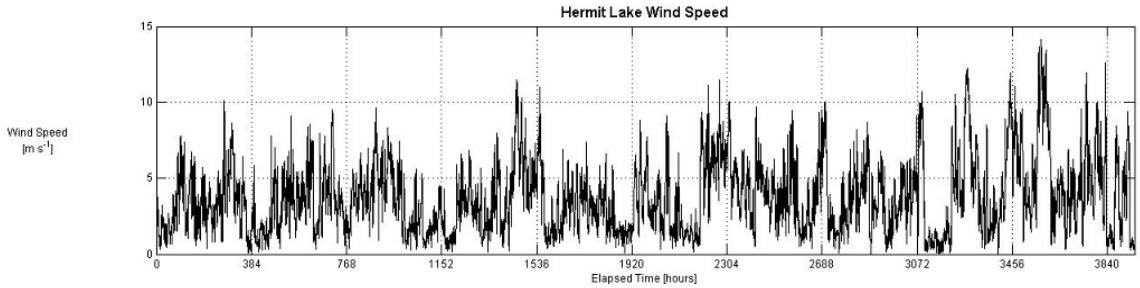

Figure 16. Wind speed [m s^{-1}] series for Hermit Lake beginning 201005261515 GMT and ending 201011070330 GMT.

Table 9. Bulk statistics for wind speed [m s^{-1}]

Max	14.139
Min	0
Mean	3.719
Mode	5.966
Std. Dev.	2.360

The wind speed maximum and standard deviation are unexpected for alpine environments. The standard deviation is remarkably low, yet wind is generally highly variable. This may be an artifact of the five-minute averages that the wind speed is recorded as. Another explanation is that Hermit Lake is in an area sheltered from the westerlies by the head wall in Tuckerman's Ravine. The headwall could act to decrease the wind speeds and therefore reduce the variability (Miller 2011, personal communication). The maximum wind speed of 14.139 m s^{-1} (roughly 32 mph), is reasonable, but the averaging process most likely dilutes the true maximum wind speed.

f. Station pressure

Station pressure is not recorded at Hermit Lake. Instead, Barnes analysis of several surrounding stations and their respective elevations (Barnes 1964) provide estimated pressure values (Figure 17; Table 10). Station pressure displays the greatest variability through much of the fall season (Figure 17), again probably from the influence of synoptic-scale low pressure systems that occur as the polar jet moves south and intensifies in the fall months (Miller 2011; personal communication).

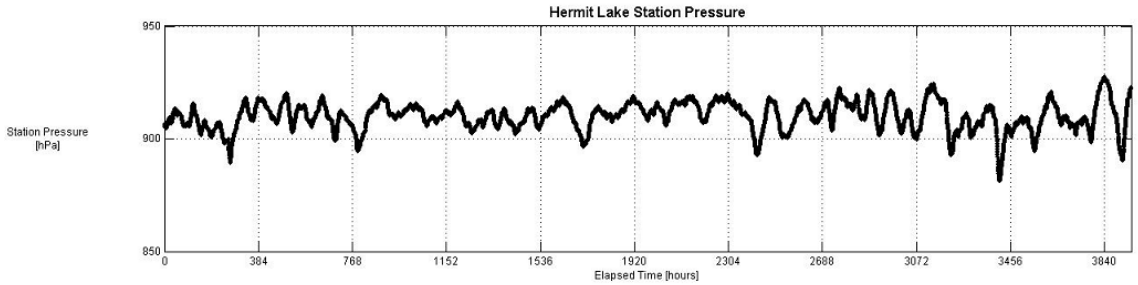

Figure 17. Station pressure [hPa] series for Hermit Lake beginning 201005261515 GMT and ending 201011070330 GMT.

Table 10. Bulk statistics for station pressure [hPa]

Max	927.601
Min	881.503
Mean	910.158
Mode	909.092
Std. Dev.	6.247

g. Albedo

Albedo is not recorded at Hermit Lake. Utilizing the albedo equations for an unfrozen lake found in Appendix A and the steps laid out in Chapter 2, the albedo is calculated (Figure 18). Albedo of the lake water surface as a function of the solar zenith angle compared reasonably well to results obtained by Payne (1972) and Albert and Mobley (2003).

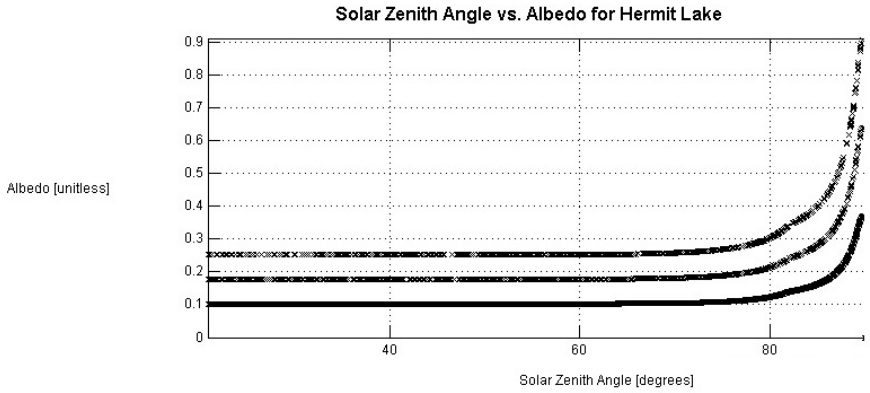

Figure 18. The albedo (*Ab*) of Hermit Lake as a function of the solar zenith angle (*Z*).

According to Petty (2008), the zenith angle (*Z*) is the angle of the sun away from directly overhead, a zenith angle of 0° is directly overhead, while a zenith angle of 90° is on the horizon. The albedo at Hermit Lake increases exponentially as the zenith angle approaches the horizon (Figure 18). This agrees with Petty's (2008) prediction that the

reflectivity (albedo) of a surface is low for a light near incidence ($Z \approx 0°$), but increases sharply to near 100% for angles near the horizon ($Z \approx 90°$). This also explains why water surfaces, in general are poor reflectors of light at high noon, but become excellent reflectors as the sun nears the horizon.

Figure 18, has three separate lines for the albedo. This is an artifact of the cloud cover estimation discussed in Chapter 2, section *a*, in which the resulting cloud cover was assigned to one of three categories: 1/8 (minimal cloud cover), 4/8 (moderate cloud cover), or 7/8 (overcast). Each cloud cover category has its own albedo value for each category. These albedo values are logical outcomes. The lowest values are associated with a cloud cover of 7/8. Conversely, the highest albedo values are associated with a cloud cover of 1/8.

h. Heat fluxes

1) INCIDENT HEAT FLUX

From Chapter 1, section *c*, the incident heat flux (Q_i) is a function of the water surface albedo (Ab) and the measured incoming short-wave radiation (I_{sw}). Incident heat flux over the study interval is plotted in Figure 19, with the associated statistics in Table 11. During the summer months (June - August), the incident heat flux appears to be at its greatest, with a maximum flux of 1008.146 W m^{-2} at the beginning of June. After August, the incident heat flux gradually and progressively decreases. This is mainly due to the increased cloud cover experienced in northern New Hampshire during the fall and winter seasons (NCDC 2011). Note that the incident heat flux and incoming solar radiation time series are very similar (Figures 14; 19), since incident heat flux is the amount of heat

absorbed by the surface from incoming shortwave radiation and the dominant term in Q_i is the measured incoming shortwave radiation.

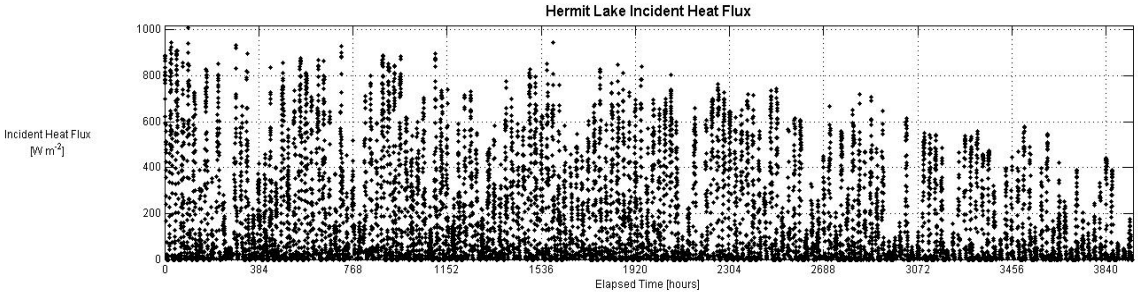

Figure 19. Incident heat flux (Q_i) series for Hermit Lake from 201005261515 GMT till 201011070330 GMT.

Table 11. Bulk statistics for Q_i [W m^{-2}]

Max	1008.146
Min	0.000
Mean	171.908
Mode	0.000
Std. Dev.	222.650

2) BLACKBODY HEAT FLUX

The blackbody heat flux $(Q_{b_{net}})$ is mainly driven by cloud cover, water vapor above the water surface, and the temperature gradient between the water surface and the air directly above it. The separate terms of the blackbody heat flux equation (Chapter 1, section *d*) derive from the original equation developed by M. E. Beriland (Budyko 1974). Net blackbody heat flux for Hermit Lake is calculated from these terms (Figure 20, Table 12).

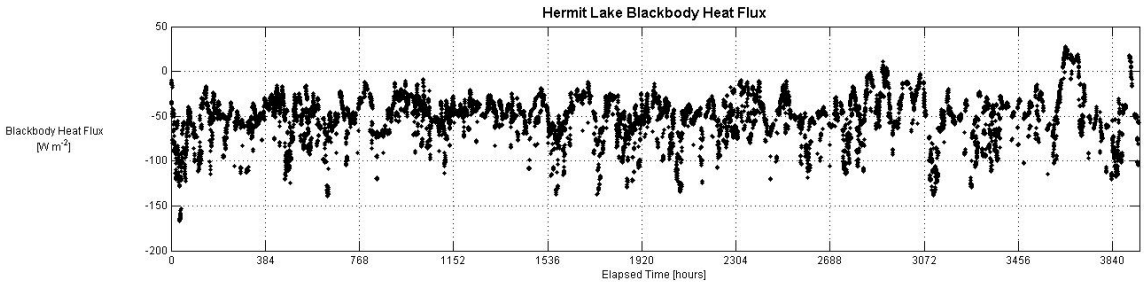

Figure 20. Blackbody heat flux ($Q_{b_{net}}$) series for Hermit Lake from 201005261515 GMT till 201011070330 GMT.

Table 12. Bulk statistics for Q_{b_1}, Q_{b_2}, Q_{b_3}, and $Q_{b_{net}}$ [W m^{-2}]

	Q_{b_1}	Q_{b_2}	Q_{b_3}	$Q_{b_{net}}$
Max	88.453	-44.789	56.277	28.253
Min	6.742	-158.813	-61.260	-166.564
Mean	28.793	-71.427	-10.778	-53.412
Mode	22.738	-57.314	-46.993	-51.402
Std. Dev.	13.002	29.162	16.537	26.747

From Table 12, the largest gain associated in $Q_{b_{net}}$ is a product of the water vapor directly above Hermit Lake and the cloud cover, both aspects of Q_{b_1}. The largest loss associated with $Q_{b_{net}}$ is in the term, Q_{b_2} (-159 W m^{-2}), involving sensible heat. This is very close to the maximum loss in $Q_{b_{net}}$ (-167 W m^{-2}), indicating that Q_{b_2} is probably responsible for most of the blackbody radiational heat loss associated with $Q_{b_{net}}$. With sensible heat, gains and losses are primarily driven by the temperature gradient between the temperature of the air directly above the water surface and the water surface temperature. The statistics for Q_{b_3} show that the maximum gain of ~ 56 W m^{-2} nearly equals the maximum loss of ~ -61 W m^{-2}. However, Q_{b_3} is mainly a loss term; its

negative mean value of ~ -11 W m^{-2} indicates that the surface water temperature is usually greater than the air temperature, during the period of study.

Overall, $Q_{b_{net}}$ contributes to net heat flux by a loss of heat, which is expected. This finding is consistent with other studies such as Miller (1999), Beardsley *et al.* (1998), and Churchill and Kerfoot (2007). There are however three distinct points in the blackbody heat flux series (Figure 20) where $Q_{b_{net}}$ is positive and so, a heat gain. These three points occur in the fall when increased cloud cover occurs over Hermit Lake (NCDC 2011) and cold air masses drop the water surface temperature below the air temperature.

3) ELECTROMAGNETIC RADIATIONAL HEAT FLUX (EMR)

The electromagnetic radiational heat flux (Q_{emr}) is the sum of the incident heat flux (Q_i) and blackbody heat flux ($Q_{b_{net}}$) (Miller 1999). Overall, the EMR heat flux is dominated by the larger, incident heat flux for most of the study period (Figure 21; Table 13). The blackbody heat flux dominates at night when the incident heat flux is equal to zero.

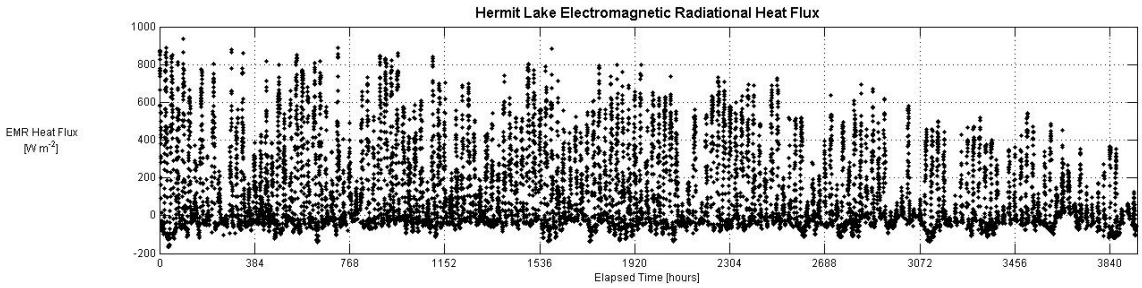

Figure 21. EMR heat flux (Q_{emr}) series for Hermit Lake from 201005261515 GMT till 201011070330 GMT.

Table 13. Bulk statistics for Q_{emr} [W m^{-2}]

Max	935.470
Min	-166.564
Mean	117.905
Mode	-62.333
Std. Dev.	223.987

4) SENSIBLE HEAT FLUX

The sensible heat flux (Q_s) is mainly a product of the temperature gradient between the water surface temperature (°C) and the air temperature (°C) directly above the lake and the wind speed (m s^{-1}). At Hermit Lake, the sensible heat flux is mostly responsible for a loss of heat from the lake (Figure 22; Table 14), with a few notable exceptions. Positive Q_s values occur when the air temperature (T_a) exceeds the surface water temperature (T_s). The greatest losses occur in late fall. During the greatest losses, the wind speed (Figure 16) is ≥ 10 m s^{-1} and the air temperature (Figure 12) is less than the water surface temperature (Figure 9) by almost 10°C.

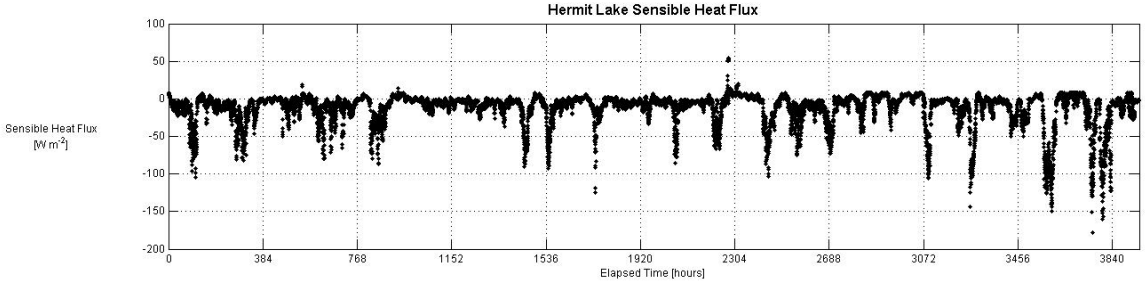

Figure 22. Sensible heat flux (Q_s) series for Hermit Lake from 201005261515 GMT till 201011070330 GMT.

Table 14. Bulk statistics for Q_s [W m^{-2}]

Max	53.825
Min	-178.654
Mean	-11.548
Mode	-12.490
Std. Dev.	20.952

The maximum heat gain associated with Q_s (54 W m^{-2}) is overshadowed by the maximum loss of -179 W m^{-2}. The negative mean value of -12 W m^{-2} affirms that the sensible heat flux is mostly a loss term for the net heat flux.

4) LATENT HEAT FLUX

The latent heat flux (Q_e) is primarily driven by wind speed and the difference between the specific humidity of the water surface and the specific humidity of the air directly above the water surface. In other words, the latent heat flux is the amount of heating or cooling produced by evaporation and condensation. For Hermit Lake, the latent heat flux produced the largest loss of heat (of the four individual heat fluxes), at -308 W m^{-2} (Figure 23; Table 15).

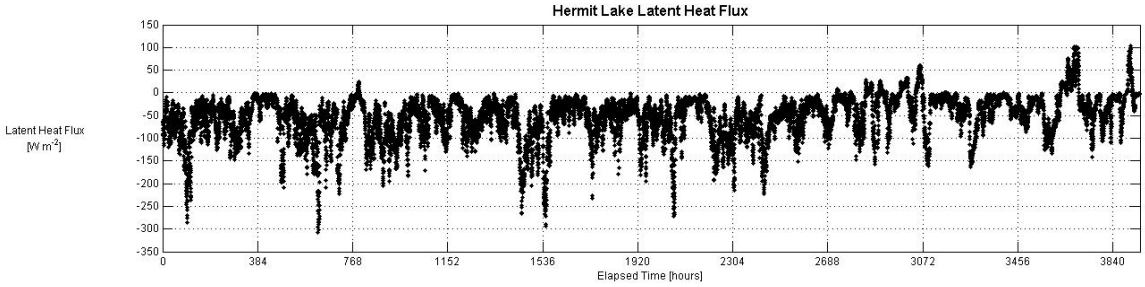

Figure 23. Latent heat flux (Q_e) series for Hermit Lake from 201005261515 GMT till 201011070330 GMT.

Table 15. Bulk statistics for Q_e [W m^{-2}]

Max	104.230
Min	-307.953
Mean	-52.666
Mode	-86.864
Std. Dev.	47.735

Overall Q_e is a loss term for the net heat flux, with a negative mean value of -53 W m^{-2}. The latent heat flux is mostly negative until the onset of fall, when several positive peaks in Q_e occur, especially near late October, early November. This can be explained by relatively cloudy conditions at this time (Figure 15) and by the nearly saturated air above Hermit Lake during this period. This saturation is due to the nearly identical air and dew point temperatures (Figures 12 and 13).

5) NET HEAT FLUX

The net heat flux (Q_n) is the sum of Q_i, Q_b, Q_s, and Q_e. For Hermit Lake, the net heat flux appears to be dominated by the incident heat flux (Figure 24; Table 16). This corresponds with the findings of Churchill and Kerfoot (2007) and Beardsley *et al.* (1998). The net heat flux is largely positive during late May and through the summer season. As the season transitions to fall, the net heat flux decreases, following the same trend as the incident heat flux (Figure 19). The standard deviation of 221 W m^{-2}, for the net heat flux, closely resembles the large variation found in Q_i. The maximum loss of heat associated with the net heat flux is -482 W m^{-2}. Most of this loss can be attributed to the losses associated with the sensible, latent, and blackbody heat flux terms.

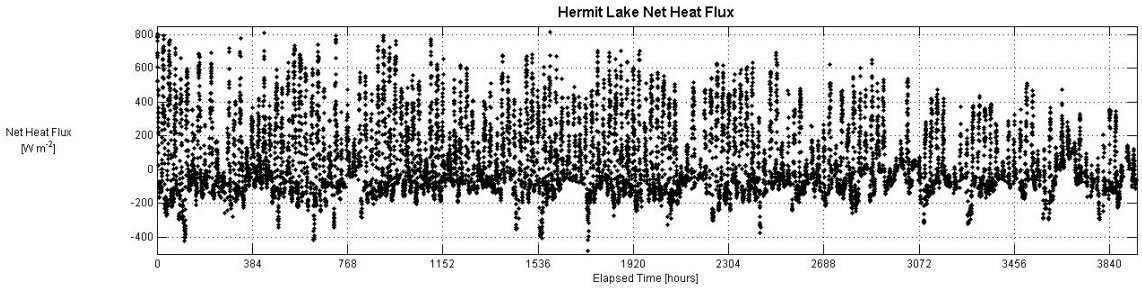

Figure 24. Net heat flux (Q_n) series for Hermit Lake from 201005261515 GMT till 201011070330 GMT.

Table 16. Bulk statistics for Q_n [W m^{-2}]

Max	814.220
Min	-481.980
Mean	54.049
Mode	-162.267
Std. Dev.	220.691

i. Total heat gain or loss by Hermit Lake

The heat fluxes (above) are input data to the calculation of total heat gained or lost for Hermit Lake over the course of the study period. A running summation calculated for each of the heat flux series is multiplied by 900 seconds (15 minutes), the time interval for data used in this study. The multiplication provides units in Joules per meter squared (J m^{-2}), the standard units for heat (Figure 25; Table 17). Negative values represent a heat loss from the lake while positive values represent a gain of heat.

Table 17. Summary of heat flux series mean values and sums.

	Mean Value [W m^{-2}]	**Sum [J m^{-2}]**
Incident Heat Flux (Q_i)	171.908	18.663 x 10^8
Blackbody Heat Flux ($Q_{b_{net}}$)	-53.412	-7.444 x 10^8
EMR Heat Flux (Q_{emr})	117.905	11.216 x 10^8
Latent Heat Flux (Q_e)	-52.666	-7.494 x 10^8
Sensible Heat Flux (Q_s)	-11.548	-1.641 x 10^8
Net Heat Flux (Q_n)	54.049	2.194 x 10^8

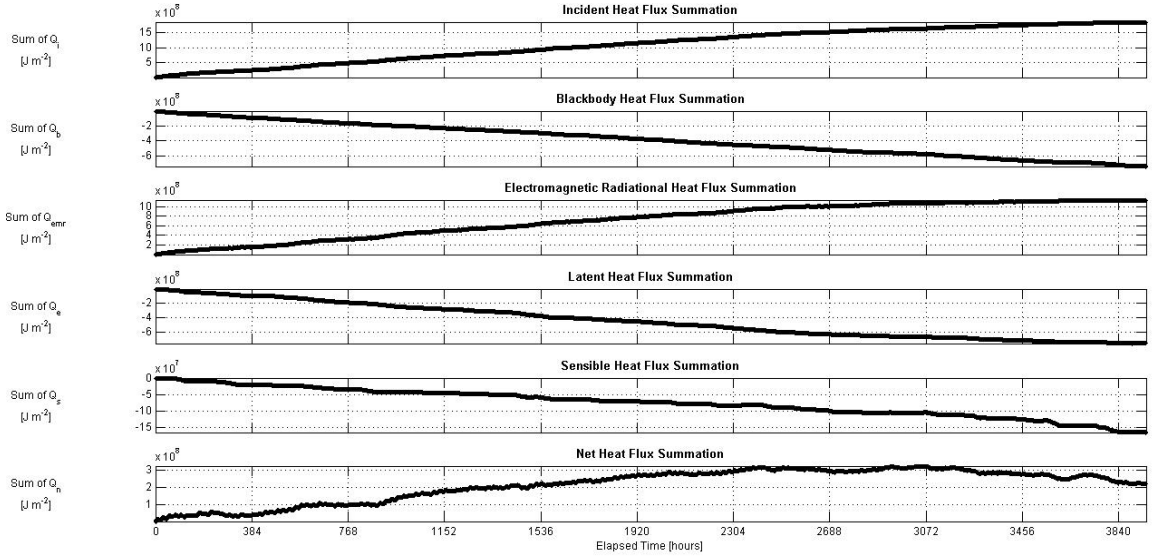

Figure 25. Graphs of the individual heat flux series summations from 201005261515 to 201011070330 GMT.

j. Frog calling and meteorological data comparisons

Frog calls were recorded and collected by Scott Smyers of Oxbow Associates during an 83 day period from May 26, 2010 until August 16, 2010. Of the four different frog species, the spring peeper, American toad, and green frog provided enough sound data during the 83 day period to produce meaningful results. The wood frog only had six days of recorded calling activity during the recording period. Linear regressions of air temperature, surface water temperature, wind speed, and the five individual heat flux summations against the spring peeper, American toad, and green frog sound data provide

some notable results (Figures 26-45). Appendix B provides the full suite of linear regressions performed on each of the four frog species.

The figures displayed below are for the meteorological variables that seem to most affect the spring peeper, American toad, or green frog. In each figure, a red line separates intervals of calling where activity increases or decreases. An actively calling frog is labeled with a frog sound category of 1, 2, or 3. The red boxes highlight the areas where the frog species are not calling; the blue boxes highlight the actively calling areas; and the green circles mark data that are considered to be outliers. In the top left corner of each graph, N represents the number of actively calling days for each frog species during the 83 day recording period.

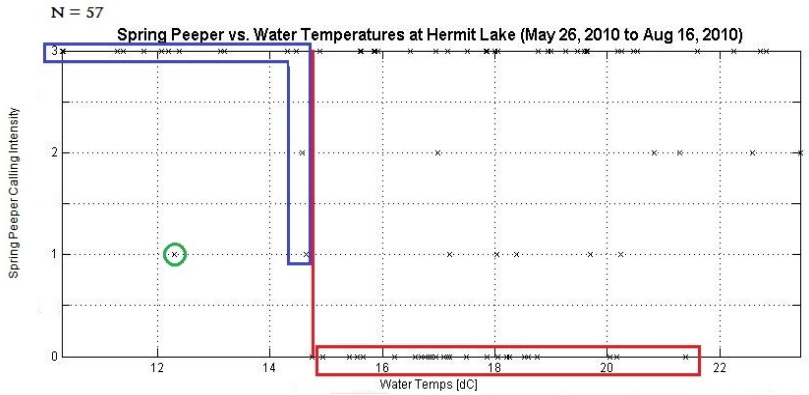

Figure 26. Comparison of the surface water temperature data and spring peeper calling intensity. Spring peeper calling activity decreases once water temperatures exceed 15°C.

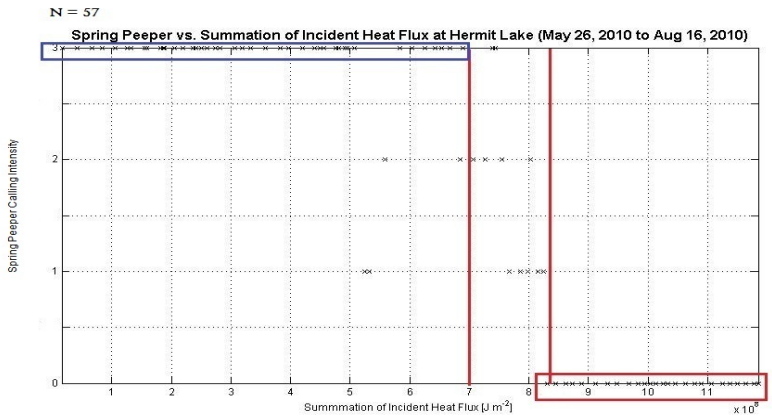

Figure 27. Comparison of the incident heat flux summation and spring peeper calling intensity. The area between $7x10^8$ J m^{-2} and $8.3x10^8$ J m^{-2} marks the transition zone from actively calling to no calling activity.

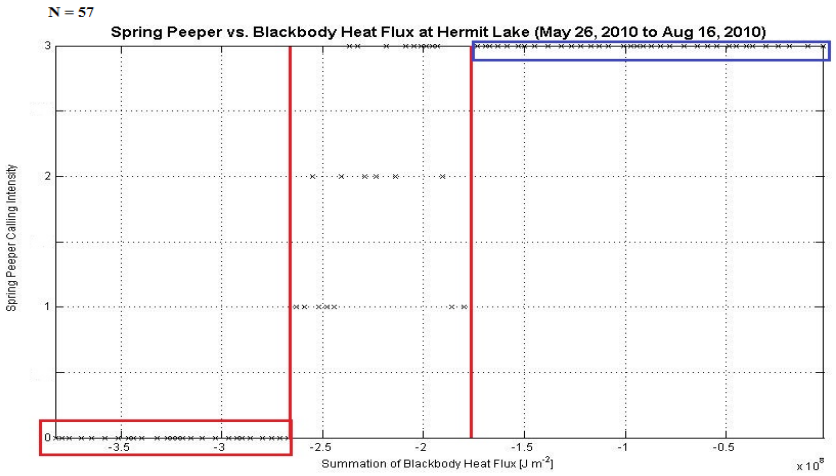

Figure 28. Comparison of the blackbody heat flux summation and spring peeper calling intensity. The area between -2.6×10^8 J m^{-2} and -1.7×10^8 J m^{-2} marks the transition zone from silence to calling.

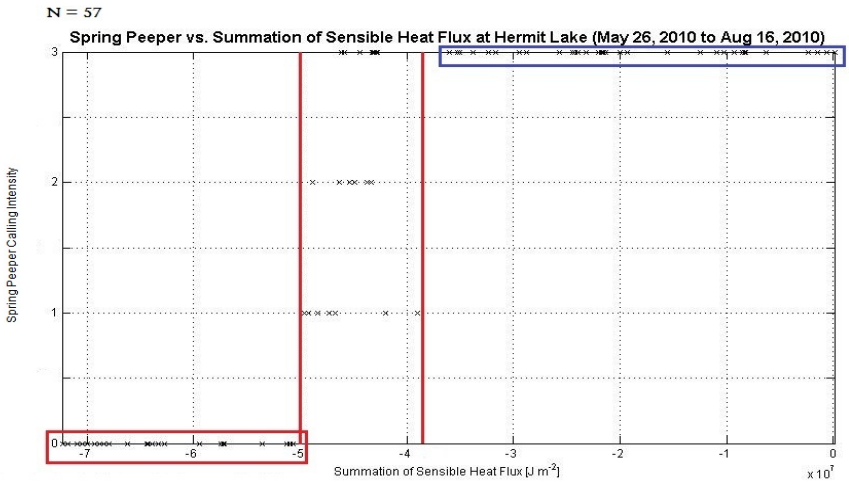

Figure 29. Comparison of the sensible heat flux summation and spring peeper calling intensity. The area between -5×10^7 J m^{-2} and -3.8×10^7 J m^{-2} marks the transition zone from silence to calling.

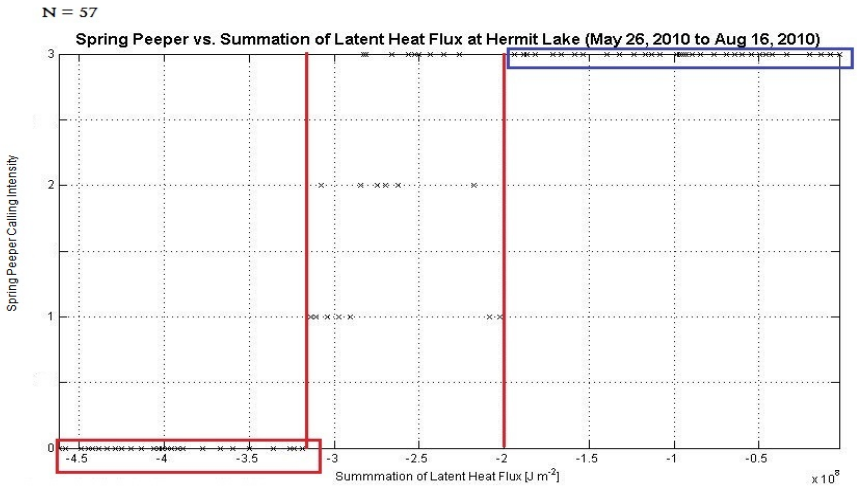

Figure 30. Comparison of the latent heat flux summation and spring peeper calling intensity. The area between -3.1×10^8 J m^{-2} and -2×10^8 J m^{-2} marks the transition zone from silence to actively calling.

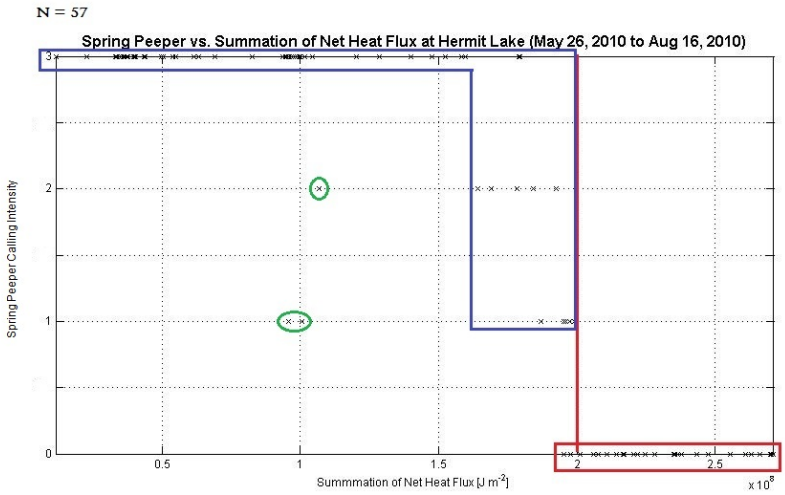

Figure 31. Comparison of the net heat flux summation and spring peeper calling intensity. Spring peeper calling activity ceases once the net heat flux summation exceeds $2x10^8$ J m^{-2}.

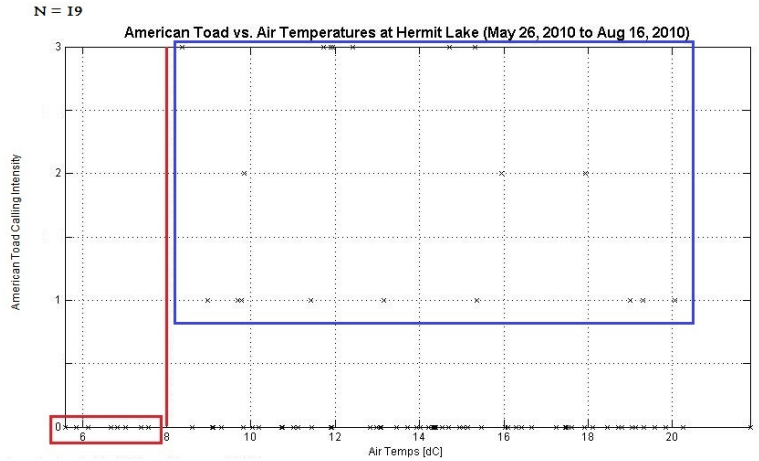

Figure 32. Comparison of the air temperature data and American toad calling intensity. American toad calling activity increases once the air temperatures exceed 8°C.

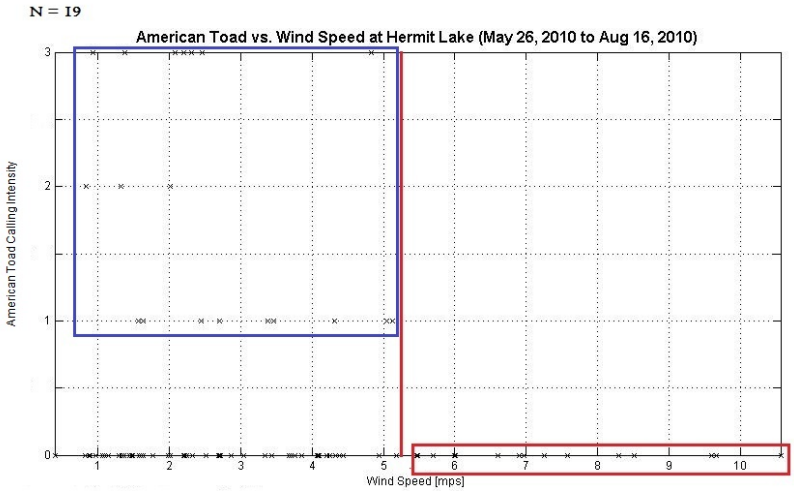

Figure 33. Comparison of wind speed data and American toad calling intensity. American toad calling activity ceases once the wind speed exceeds 5.2 m s^{-1}.

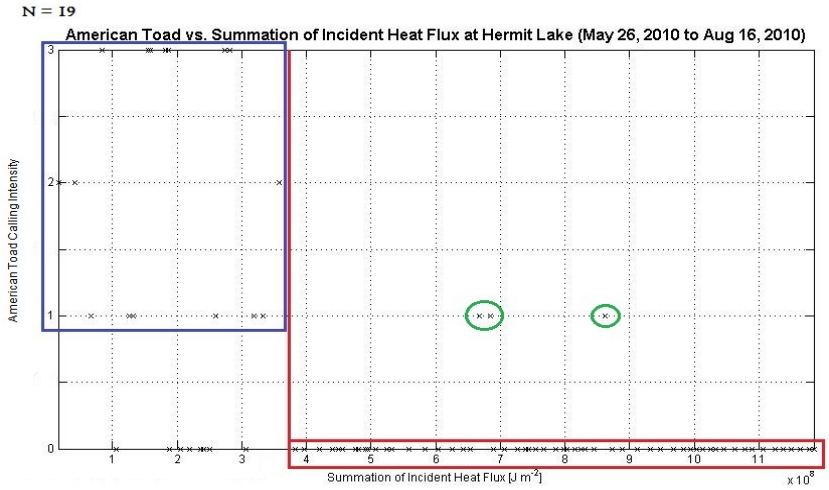

Figure 34. Comparison of the incident heat flux summation and American toad calling intensity. American toad calling activity decreases once the incident heat flux summation exceeds 3.8×10^8 J m^{-2}.

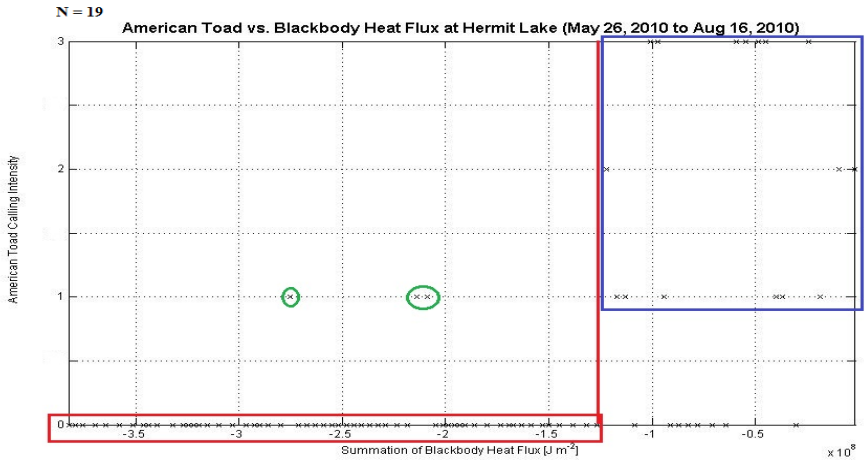

Figure 35. Comparison of the blackbody heat flux summation and American toad calling intensity. American toad calling activity increases once the blackbody heat flux summation exceeds -1.3×10^8 J m^{-2}.

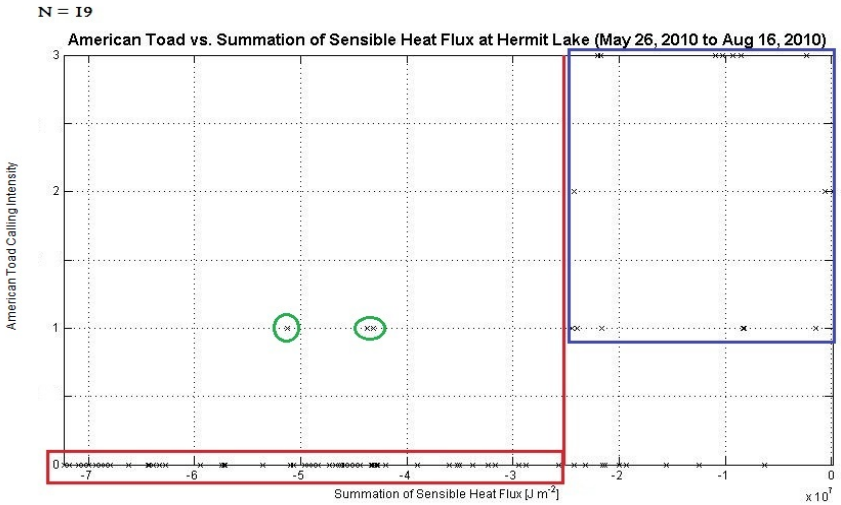

Figure 36. Comparison of the sensible heat flux summation and American toad calling intensity. American toad calling activity increases once the sensible heat flux summation exceeds -2.5×10^7 J m^{-2}.

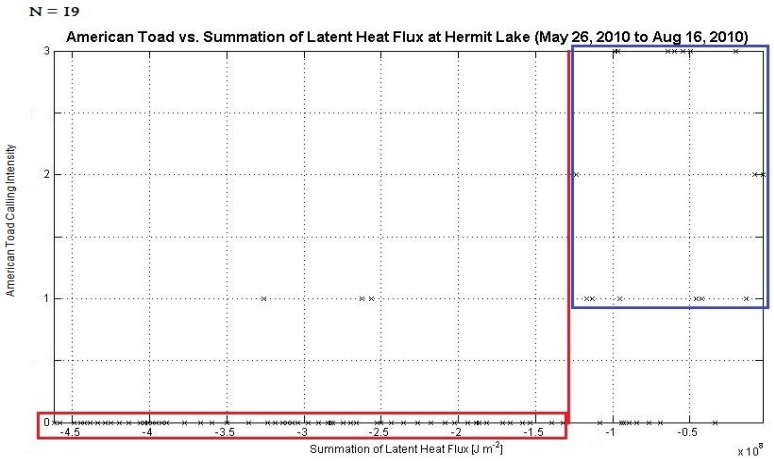

Figure 37. Comparison of the latent heat flux summation and American toad calling intensity. American toad calling activity increases once the latent heat flux summation exceeds -1.25x10^{8} J m^{-2}.

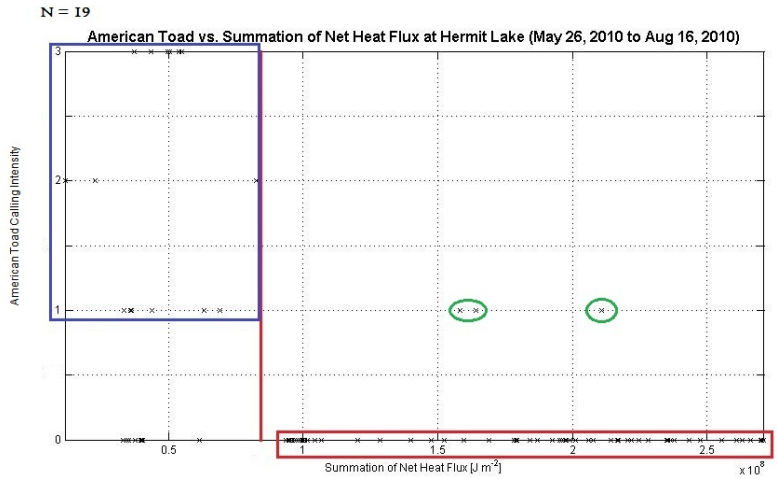

Figure 38. Comparison of the net heat flux summation and American toad calling intensity. American toad calling activity decreases once the net heat flux summation exceeds 0.8x10^{8} J m^{-2}.

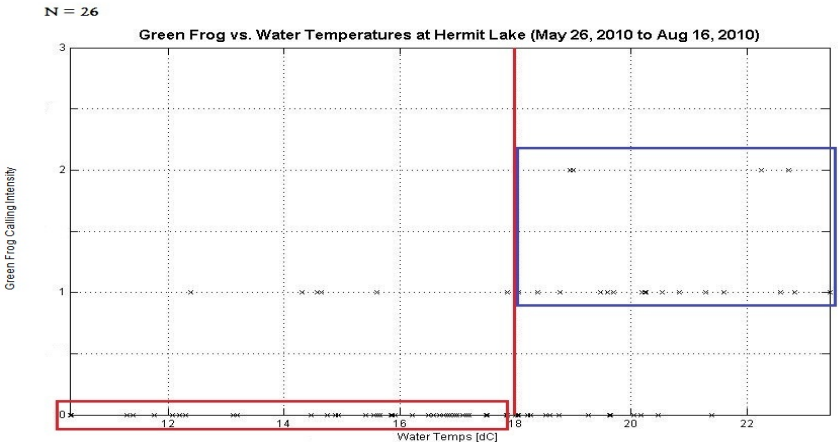

Figure 39. Comparison of surface water temperature data and green frog calling intensity. Green frog calling activity increases once the surface water temperatures exceed 18°C.

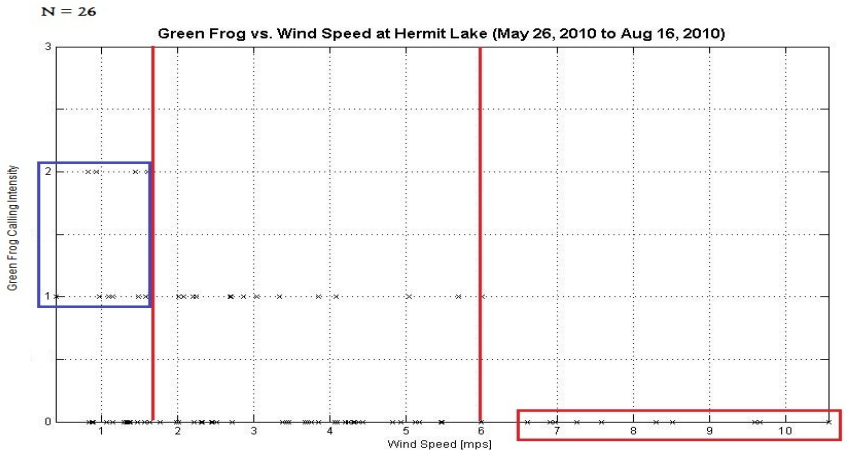

Figure 40. Comparison of wind speed data and green frog calling intensity. Green frog calling activity decreases once the wind speed exceeds 1.7 m s^{-1}.

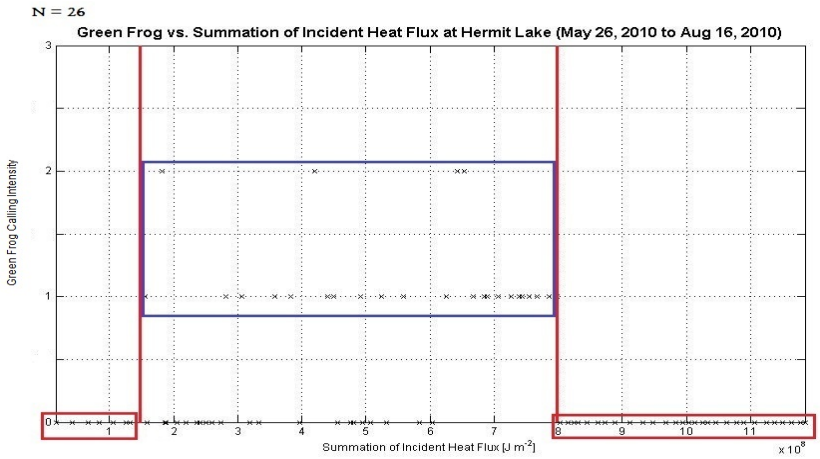

Figure 41. Comparison of the incident heat flux summation and green frog calling intensity. Green frog calling activity increases once the incident heat flux summation exceeds $1.5x10^8$ J m^{-2} and decreases once the heat flux values exceed $8x10^8$ J m^{-2}.

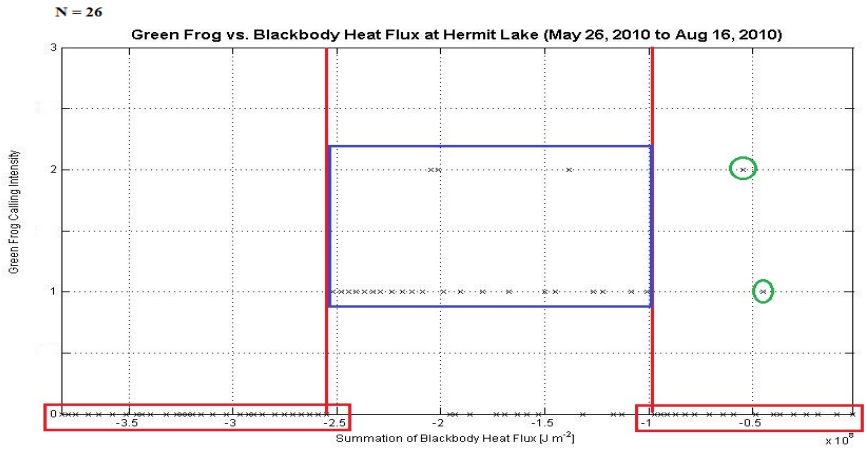

Figure 42. Comparison of the blackbody heat flux summation and green frog calling intensity. Green frog calling activity increases once the blackbody heat flux summation exceeds $-2.5x10^8$ J m^{-2} and decreases once the heat flux values exceed $-1x10^8$ J m^{-2}.

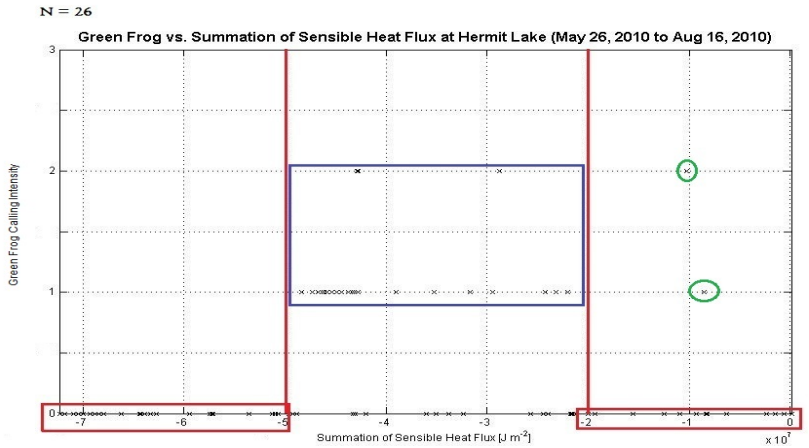

Figure 43. Comparison of the sensible heat flux summation and green frog calling intensity. Green frog calling activity increases once the sensible heat flux summation exceeds $-5x10^7$ J m^{-2} and decreases once the heat flux values exceed $-2x10^7$ J m^{-2}.

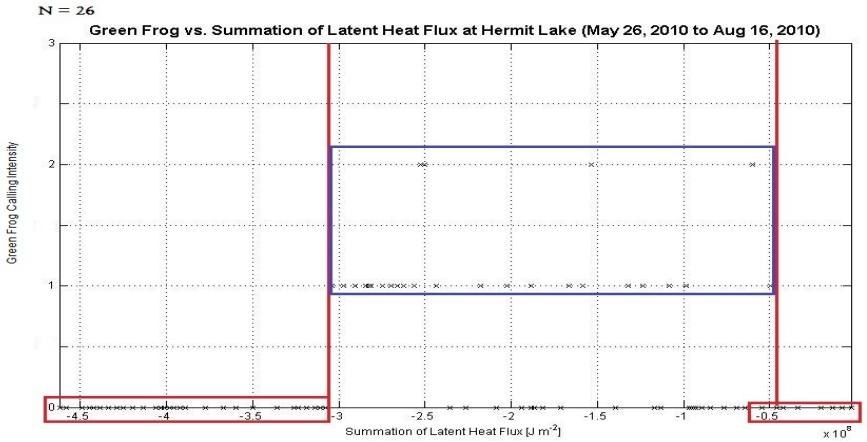

Figure 44. Comparison of the latent heat flux summation and green frog calling intensity. Green frog calling activity increases once the latent heat flux summation exceeds $-3.1x10^8$ J m^{-2} and decreases once the heat flux values exceed $-0.5x10^8$ J m^{-2}.

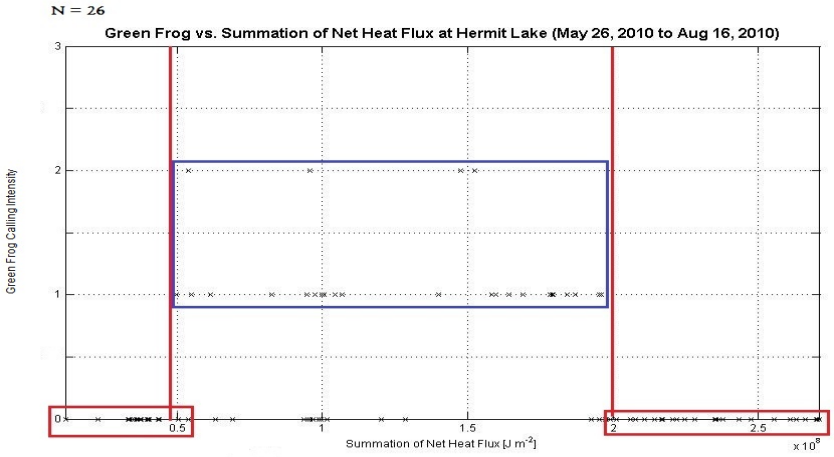

Figure 45. Comparison of the net heat flux summation and green frog calling intensity. Green frog calling activity increases once the net heat flux summation exceeds $0.5x10^8$ J m^{-2} and decreases once the heat flux values exceed $2x10^8$ J m^{-2}.

CHAPTER 4

4. Discussion and Conclusions

a. Discussion

1) HEAT FLUXES

The net heat flux (Q_n) is the sum of the incident heat flux (Q_i), the blackbody heat flux ($Q_{b_{net}}$), the sensible heat flux (Q_s), and the latent heat flux (Q_e). The incident heat flux appears to be responsible for a large source of heat gain within Hermit Lake with a fairly large mean value of 171.908 W m^{-2} and a maximum value of 1008.146 W m^{-2} (Table 11). The largest incident heat flux values occur during late spring through early summer (Figure 19). With the transition into fall, the solar elevation angles, as well as the amount of sunlight per day decreases, thereby decreasing the incident heat flux. Under these conditions, the loss terms $Q_{b_{net}}$, Q_s, and Q_e may have a heightened effect on the net heat flux. Power spectrum analysis to determine the behavior of the incident heat flux over time, produces two large peaks above the 95% confidence interval. The first peak is likely an artifact of the cloud cover estimation technique (Chapter 2, section *a*). The second peak is quite large and occurs at the 24 hour mark. The appearance and size of the second peak affirms that the incident heat flux has a strong, and anticipated diurnal behavior.

The blackbody heat flux is a loss term for most of the study period and is dependent on the water vapor present in the air above the water surface, cloud cover, and the temperature gradient present between the air above the lake and the water itself. The largest gains by $Q_{b_{net}}$ are actually produced by the water vapor term found in Q_{b_1} and the sensible term found in Q_{b_3} (Table 12).

Figure 46 compares the vapor pressure, the temperature gradient between the lake water surface and the air above the lake, the incident heat flux, and the blackbody heat flux. The black arrows point to areas where the blackbody heat flux produces either a minimal loss of heat or a gain of heat. Notice that the gains produced by the blackbody heat flux as well as the minimal losses of heat are associated with large spikes in the vapor pressure and periods where the air temperature is greater than the surface water temperature. The largest gains of heat, which are found in mid-October to early November, are also associated with fairly cloudy conditions and low solar elevation angles, as seen in the incident heat flux.

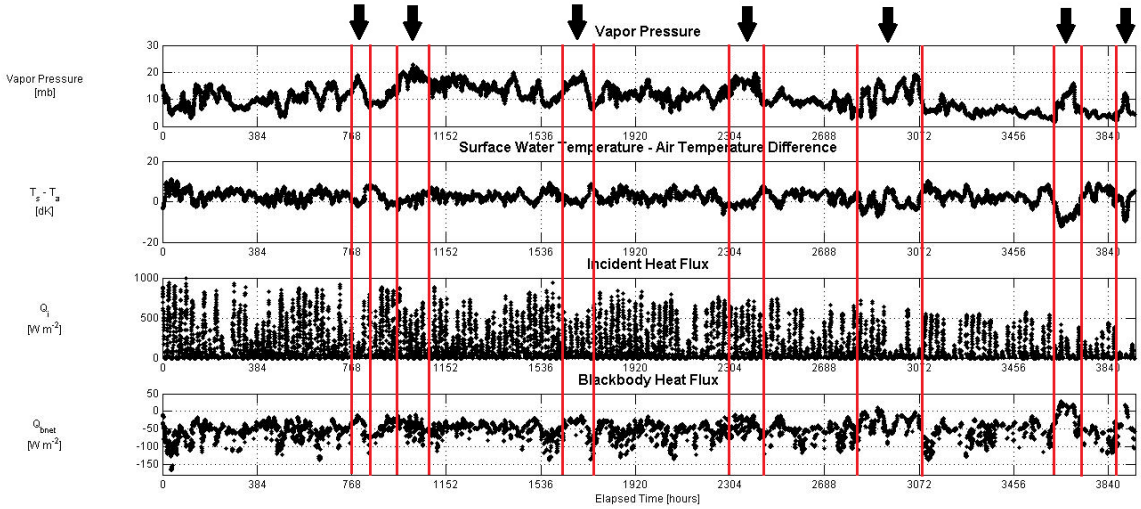

Figure 46. Comparison of the vapor pressure, temperature gradient between the air temperature and the surface water temperature, incident heat flux, and blackbody heat flux. The red lines and black arrows mark areas where the blackbody heat flux is positive (gaining heat) or nearly positive (very small losses of heat).

It is speculated that the last three "events" in Figure 46 each coincide with the passage of low pressure systems and their associated frontal systems, mainly the warm front. According to Martin (2006), the cloud structure associated with a mid-latitude cyclone's warm front is normally widespread to the northern edge of the front, with gradual clearing southward of the southern edge of the front. The area on the southern side of the warm front and east of the cold front is known as the "warm sector" due to the

warm, moist air that is associated with this area (Figure 47). During these events, it is very plausible that Hermit Lake experienced substantial to moderate cloud cover with a warm, moist air mass directly over the lake. The warm, moist air would explain the "spikes" in the vapor pressure as well as the large negative temperature gradients (Figure 46).

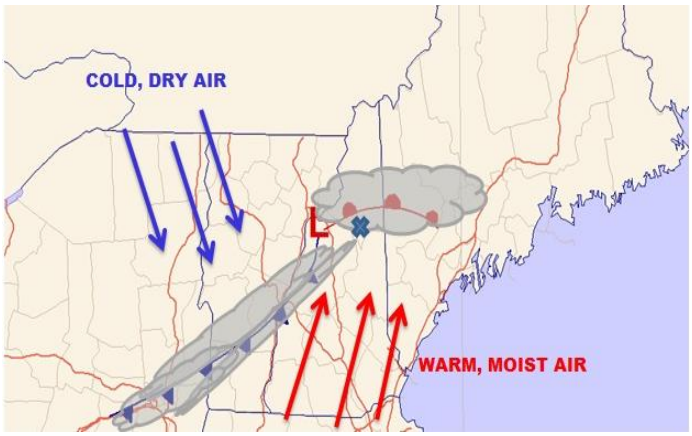

Figure 47. Idealized mid-latitude cyclone frontal structure over northern New England. The blue X marks the approximate location of Hermit Lake.

Since these temperature gradients involve the sensible term in $Q_{b_{net}}$ a negative temperature gradient ($T_a > T_s$) actually implies a heat gain (Equation 3.3). Thus, the negative temperature gradients, most likely from a warm front, will create a positive effect on the blackbody heat flux. The relatively moderate to low values of the incident heat flux during these three events are most likely from the approach and passage of a warm front and its associated cloud cover.

Spectral analysis of the blackbody heat flux produces two rather large peaks above the 95% confidence interval, one at the one hour mark, the second at the 24 hour mark. As with the analysis of the incident heat flux, the first peak is believed to be an artifact of the cloud cover estimation technique used to produce 15-minute cloud cover data for this research. The second peak indicates that the blackbody heat flux, like the

incident heat flux, exhibits a diurnal behavior. This behavior is expected; there is most likely greater losses of heat in relation to $Q_{b_{net}}$ during the night, due to a lack of sunlight.

The similarity in spectral results for the incident and blackbody heat fluxes raises the question: How do the two heat fluxes interact? Cross correlation of the two heat flux series, with the incident heat flux as the independent variable and the blackbody heat flux as the dependent variable, reveal that minima in the blackbody heat flux occur approximately two days and 14 hours prior to maxima in the incident heat flux. This timeframe closely follows the periodicity of the weather band, with roughly a three day period between the passage of low pressure systems at a certain point (Miller 2011; personal communication). A minimum in $Q_{b_{net}}$ may occur with the passage of a cold front. At Hermit Lake, this requires advection of cold, dry air over New Hampshire, from Canada, and thick cloud cover (Figure 48). Approximately two and a half to three days later, high pressure moves into the Hermit Lake area and advects warm, possibly moist air from the south. This dissipates the cloud layer and allows for clear skies and maximum values of Q_i (Figure 49).

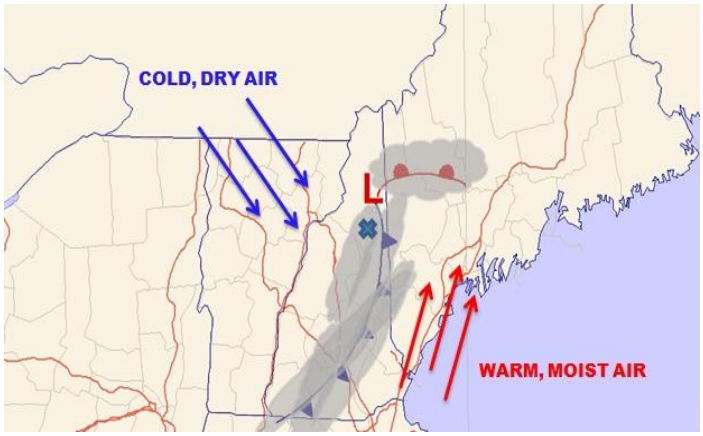

Figure 48. Idealized mid-latitude cyclone frontal structure over northern New England. The blue X marks the approximate location of Hermit Lake. Minimal values of $Q_{b_{net}}$ are estimated to be occurring with this synoptic setup.

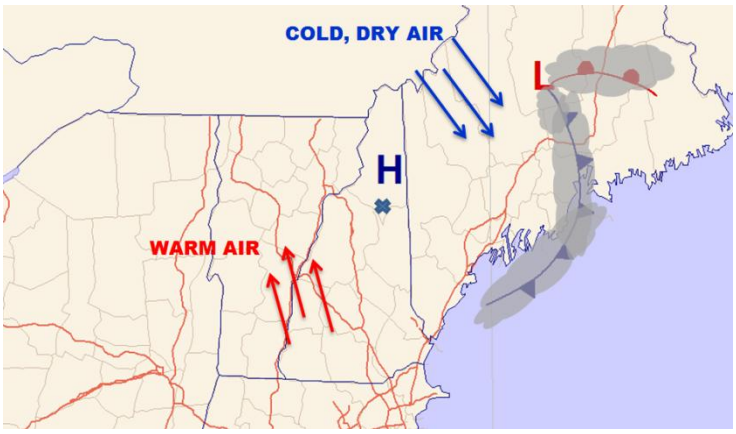

Figure 49. Approximately 2.5 days after Figure 48. Clear skies associated with high pressure system allow for a maximum in Q_i. The blue X marks the approximate location of Hermit Lake.

Sensible heat flux and latent heat flux both present (mostly) losses for the period of study (Table 17), with mean values of -11.548 W m^{-2} (Q_s) and -52.666 W m^{-2} (Q_e), respectively. The greatest losses of heat in Q_s are mostly during late fall, with a few exceptions (Chapter 3, section *h*-4). These losses appear to be associated with wind speeds ≥ 10 m s^{-1} and air temperatures ~ 10°C cooler than the surface water temperatures. Figure 50 highlights the areas of greatest heat loss within Q_s along with the wind speeds and temperature differences at the time of the maximum heat losses.

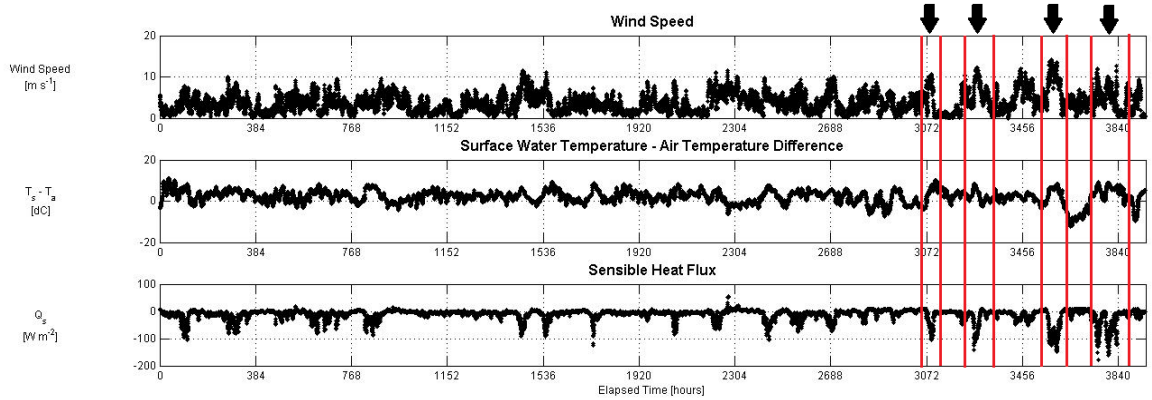

Figure 50. Comparison of the wind speed, temperature gradient between the air temperature and the surface water temperature, and the sensible heat flux. The red lines and black arrows mark areas of maximum heat loss associated with Q_s.

Two cross correlation analyses on the wind speed and temperature gradient against the sensible heat flux reveal that sensible heat flux minima occur frequently, 15-

minutes after maxima in wind speed. The second analysis indicates that maxima in the sensible heat flux occur roughly three and a half days prior to maxima in the positive temperature gradient ($T_s > T_a$). Positive temperature gradients infer losses in the sensible heat flux (Equation 4, Chapter 1, section *e*). Therefore, when the water temperature exceeds the air temperature, a loss of heat (by the sensible heat flux) occurs.

These results indicate that windy conditions and the positive temperature gradient associated with the losses of heat in Q_s arrived with the passage of a fairly strong cold front. Figures 48 and 49 can again be used to explain this process beginning with Figure 49. When high pressure dominates Hermit Lake and its surroundings, it is accompanied by clear skies and advection of southerly warm air into the area (Figure 49). Wind speeds are fairly light while the air temperature is most likely warmer than the water surface temperature. This combination will produce maximum values in Q_s with minimal losses of heat from the lake. Approximately three days later, following the exit of high pressure, a low pressure system moves over Hermit Lake. Cold air from Canada advects into the Hermit Lake area behind the cold front with increasing wind speeds. The increased wind speeds combined with the positive temperature gradient ($T_s > T_a$) create a minima in Q_s and maximum heat losses from the lake (Figure 50).

The latent heat flux is a function of wind speed and the difference between the specific humidities of the water surface (q_s) and air (q_a) (Chapter 1, section *f*). The latent heat flux is negative until mid to late October then slowly increases and produces a large heat gain in three distinct time periods (Figure 51). These maxima in the latent heat are most likely associated with a saturated airmass, dew point temperatures that are warmer

than the surface water temperature, relatively light winds, and a slightly negative specific humidity gradient between the air and surface water ($q_a > q_s$).

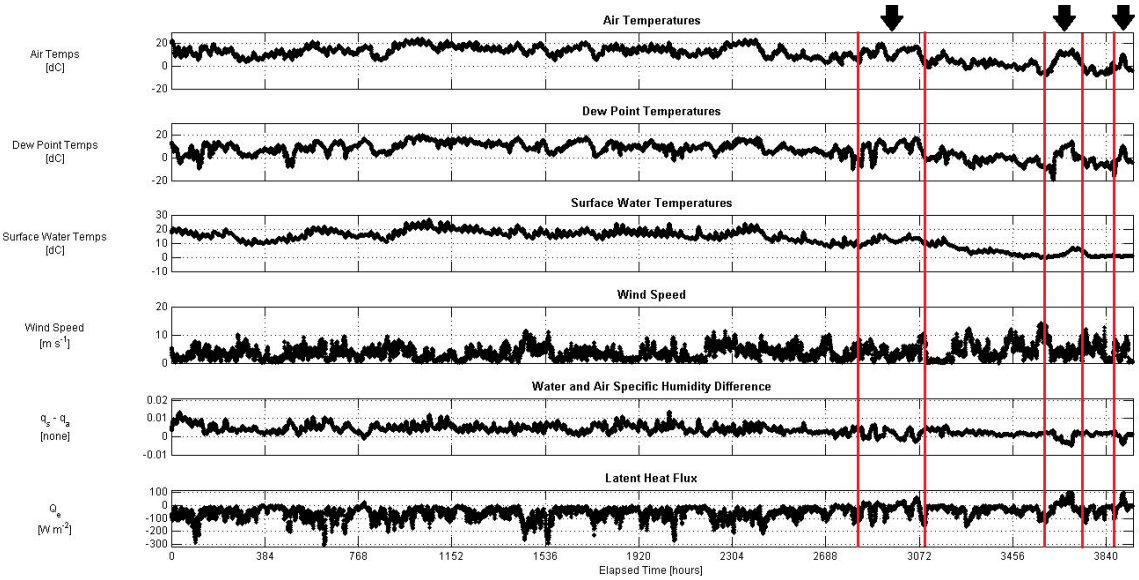

Figure 51. Comparison of air temperatures, dew point temperatures, surface water temperatures, wind speed, the specific humidity gradient between the air and water surface, and the latent heat flux. The red lines and black arrows mark areas where the latent heat flux is responsible for a gain of heat.

Cross correlation analysis reveals that four and a half days after minima in the specific humidity gradient ($q_a > q_s$), minima in Q_e occur. The four and a half day period can be explained by the passage of a high pressure system. High pressure is located to the east of Hermit Lake, which in this location; Hermit Lake is under the influence of moist, warm air advection by the southeasterly flow produced by the clockwise rotation of the high pressure system (Figure 52). The air directly over Hermit Lake is fairly moist and most likely warmer than the surface water temperature as is the dew point temperatures. The winds in this sector of the high pressure system are fairly light (Miller 2011; personal communication), which allows the air and dew point temperatures to increase faster than the surface water temperatures, creating a minimum in the specific humidity gradient between the air and water and a heat gain by the lake.

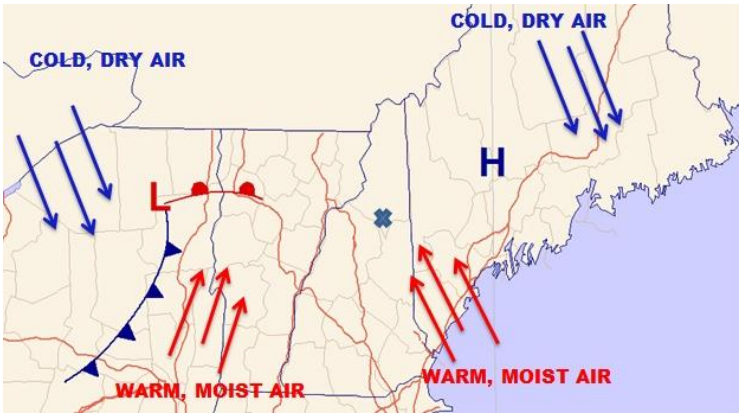

Figure 52. Speculative synoptic setup creating a minimum specific humidity gradient and a heat gain by the latent heat flux. The blue X marks the approximate location of Hermit Lake.

Four and half days following the minimum in the specific humidity gradient, the high pressure system has moved on with a low pressure system located to the west and its associated cold front to pass through the Hermit Lake area. Advection of cold, dry air follows behind the passage of the cold front with the eastern edge of the secondary high pressure system beginning to build in (Figure 53). The location of Hermit Lake between these two pressure systems is conducive to stronger wind speeds and dryer air masses (Figure 53). The combination of strong wind speeds, cold temperatures, and dry air create minima the latent heat flux.

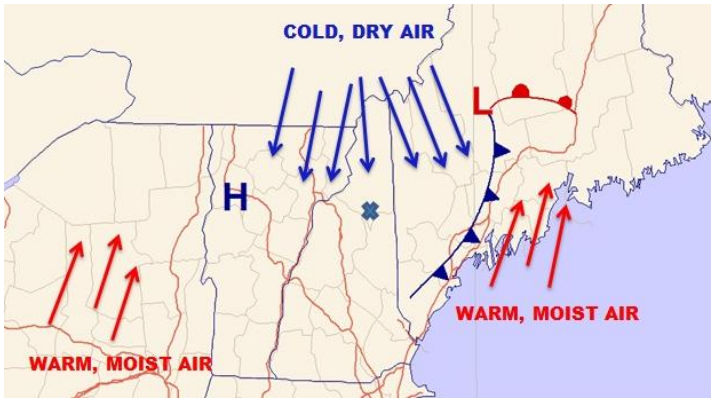

Figure 53. Speculative synoptic setup 4.5 days after Figure 52. The blue X marks the approximate location of Hermit Lake.

Spectral analysis of the sensible and latent heat fluxes reveals no peaks above the 95% confidence interval in either analysis contrary to prior expectations of a diurnal or weather band peak. The lack of any significant peaks in each analysis signifies that neither the air nor water temperatures are behaving as expected. Wind speed is also a key component within each flux and may be partially responsible for this unpredictability of the behavior of each flux. Therefore, further research is necessary to determine how the air and water temperatures as well as the wind are interacting within Hermit Lake.

The net heat flux is highly variable especially in late spring through late summer (Figure 24, Chapter 3). As the transition from summer to fall occurs, the variability in the net heat flux gradually decreases. The incident heat flux produces the greatest gains of heat associated with the net heat flux and is also the dominant heat flux out of the four individual fluxes. Cross correlation analysis of the four heat fluxes versus the net heat flux quantitatively supports the notion that the incident heat flux is the dominant term within the net heat flux, which accounts for 93% of the total variance in Q_n. The second largest component of the net heat flux is the sensible heat flux followed by the blackbody heat flux. The combined effects of Q_i, $Q_{b_{net}}$, and Q_s are instantaneous and large enough to mask the small effects by Q_e, which are notable approximately four hours and 15 minutes after a maximum in Q_n occurs (Table 18).

Table 18. Results of cross correlation analysis performed on the four heat fluxes vs. the net heat flux. The 95% confidence interval is above 0.0039785. The closer to 1 the correlation is, the better the correlation. The time lag is the time it takes for the heat fluxes to affect the net heat flux after a maximum in Q_n occurs.

Heat Flux	**Correlation [Time Lag (minutes)]**
$\boldsymbol{Q_i}$	0.93334069 [0]
$\boldsymbol{Q_{b_{net}}}$	0.22797320 [0]
$\boldsymbol{Q_s}$	0.32748681 [0]
$\boldsymbol{Q_e}$	0.15387223 [255]

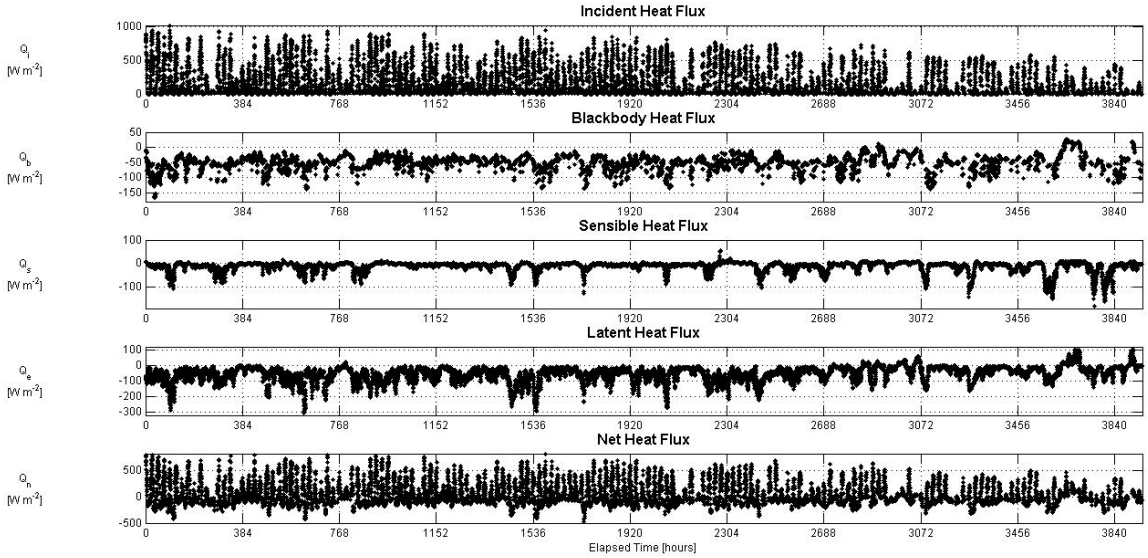

Figure 54. Comparison of all five heat fluxes within Hermit Lake.

Wavelet analysis to determine if any peaks, such as a diurnal signal, are hidden by non-periodic signals within the previous spectral analyses of the five heat fluxes, further reaffirms that the incident heat flux is the dominant driver of variations within the net heat flux. To perform this analysis, the online interactive wavelet analysis toolkit is utilized (Torrence and Compo 2011). The toolkit only allows 2000 datapoints at a time to be analyzed, therefore to produce statistically meaningful results, the temporal resolution for each of the heat flux series is reduced from 15-minutes to one hour using AIRSEA

(Miller 2011). Each of the heat flux series is then split into three time periods to accomadate the 2000 data point limit. The first time period is from May 26, at 1700 GMT to July 26, at 1700 GMT. During this time period, it is estimated that 27% of the data is missing due to missing cloud cover data. The second time period is from August 5, at 1000 GMT to October 5, at 1000 GMT. It is estimated that 30% of the data is missing due to missing cloud cover data. The final time period is from October 10, at 0500 GMT to November 4, at 1000 GMT. It is estimated that 40% of the data is missing during this period due to missing cloud cover data. Following these steps the wavelet analysis is performed on each of the heat flux series.

Only the incident and net heat flux series produces statistically meaningful results. Within each of the analyses, there are two prominent peaks above the 95% confidence interval, one at 12 hours and the second at 24 hours (Figures 55-60). These peaks are associated with the diurnal behavior of the incident heat flux and also further reaffirms that the incident heat flux is the primary driver in variations within the net heat flux. The other three heat fluxes either contain no peaks above the 95% confidence interval or the peaks are too weak to be considered statistically meaningful. Each figure associated with the wavelet analysis of the incident and net heat fluxes contains three graphs (Figures 55-60). Graph *a*, is the actual heat flux during the time period of analysis. Graph *b*, contains the colored power spectrum graph. This graph depicts the power of depicted periodicity, with red being the highest power and white being the lowest. The hatched area is known as the "cone of influence". This area marks data that is unreliable due to the overall length of the data series. The most important graph for this research is graph *c.* The dashed line is the 95% confidence interval line. Any peaks above this line are deemed

statistically meaningful. For a more in depth discussion of wavelet analysis, please refer to Torrence and Compo (1998).

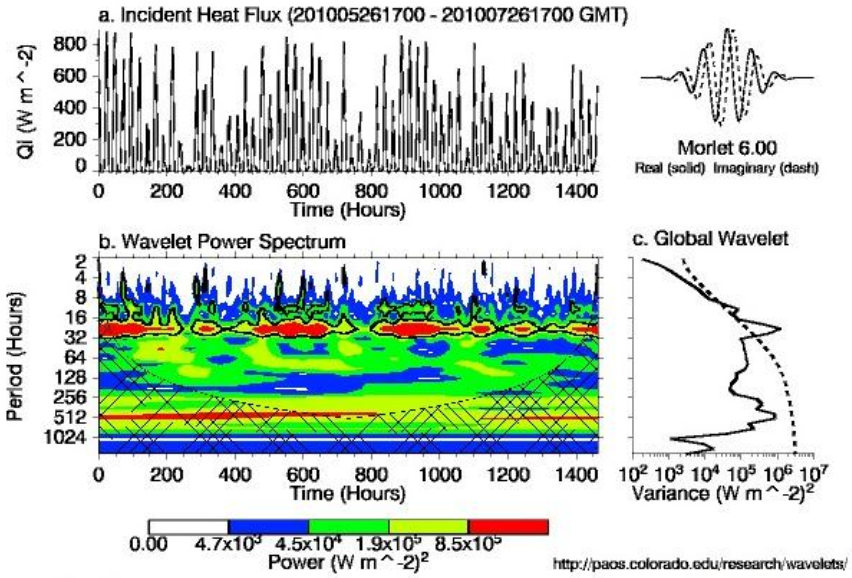

Figure 55. Wavelet analysis of the incident heat flux from May 26, at 1700 GMT to July 26, at 1700 GMT.

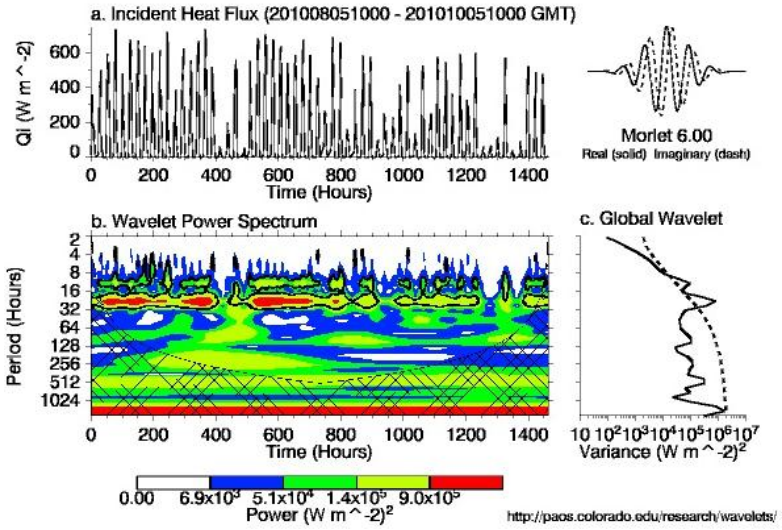

Figure 56. Wavelet analysis of the incident heat flux from August 5, at 1000 GMT to October 5, at 1000 GMT.

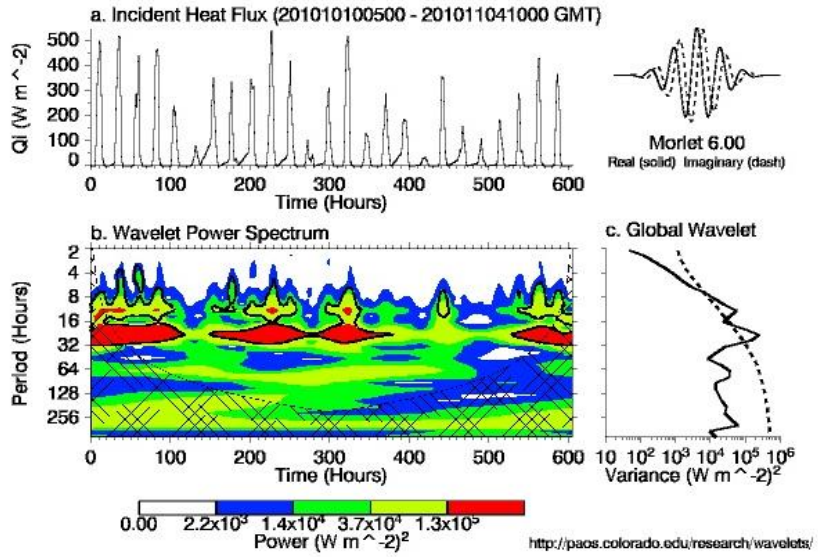

Figure 57. Wavelet analysis of the incident heat flux from October 10, at 0500 GMT to November 4, at 1000 GMT.

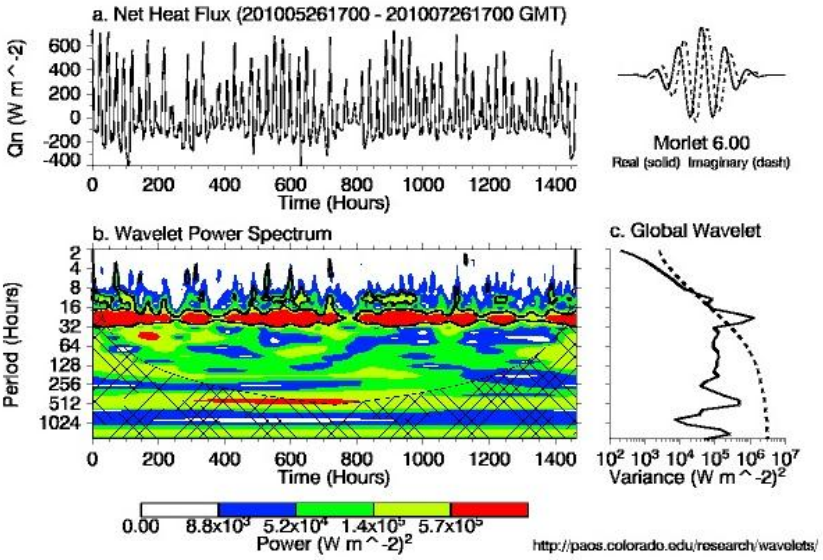

Figure 58. Wavelet analysis of the net heat flux from May 26, at 1700 GMT to July 26, at 1700 GMT.

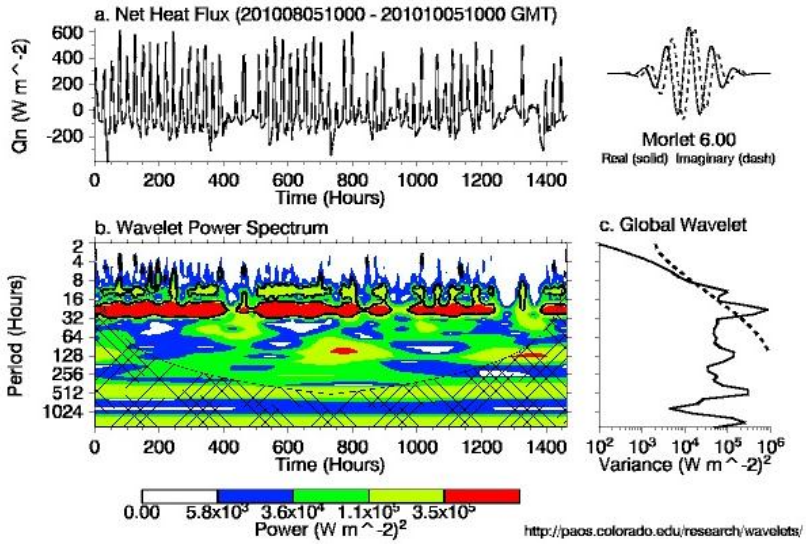

Figure 59. Wavelet analysis of the net heat flux from August 5, at 1000 GMT to October 5, at 1000 GMT.

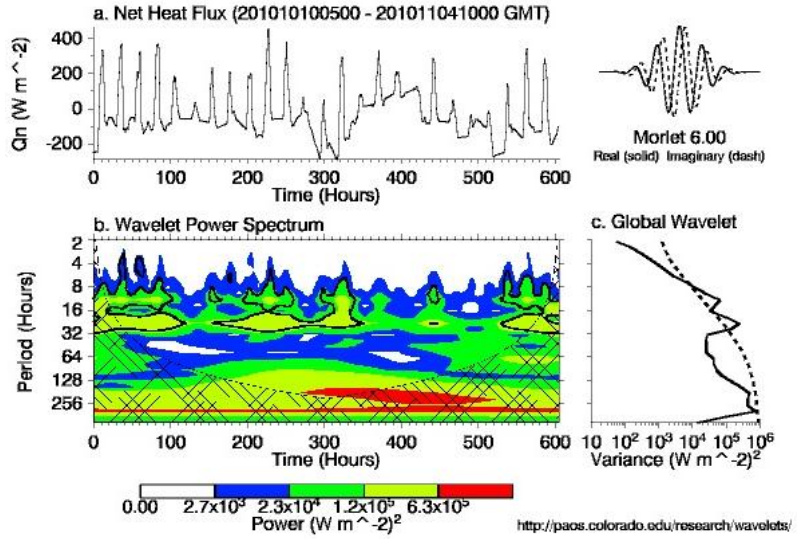

Figure 60. Wavelet analysis of the net heat flux from October 10, at 0500 GMT to November 4, at 1000 GMT.

The total summation of each individual heat flux provides insight into the amount of heat the lake is gaining or losing over the period of this study due to each heat flux (Table 17). By far, the largest source of heat gain or loss is the incident heat flux with a total heat gain of 18×10^8 J m^{-2}. Of the four heat fluxes that make up the net heat flux, Q_i is the only heat flux producing a net gain of heat over the entirety of the study period. The maximum heat gain by the incident heat flux does not occur during the summer,

when the sun is normally at its highest point over New Hampshire, rather, it occurs in late fall (Figure 25). This implies that there is a storage effect of heat within Hermit Lake. The water absorbs the heat from the sun's rays and allows the energy to build up over time within the lake. With the onset of fall, the heat absorbed during the summer is slowly released to heat Hermit Lake through the fall. Even as the height of the sun lowers in the sky during the fall and the amount of sunlight reaching the earth's surface reduces (Figure 14), thereby reducing the incident heat flux (Figure 19), Hermit Lake is continuing to gain heat due to the incident heat flux. These gains in late fall, however, are offset by the combined losses produced by $Q_{b_{net}}$, Q_e, and Q_s.

The largest loss of heat in Hermit Lake is attributable to the latent heat flux with a total heat loss of ~ -8x10^8 J m^{-2}. The loss produced by Q_e is similar to the heat loss of -7x10^8 J m^{-2} by $Q_{b_{net}}$. The sensible heat flux has a minimal effect on the net heat flux with a total heat loss of only ~ -1x10^8 J m^{-2}. However, with the onset of late fall, the sensible heat flux decreases and produces larger losses. Had the study period been extended through the winter season, it is this author's belief that the sensible heat flux would contribute to the net heat flux as a source of larger heat losses. Further research is necessary to determine if this is true.

Hermit Lake is gaining heat from May 26, 2010 till October 1, 2010 at 1800 GMT, where the net heat flux decreases. This decrease is largely due to the minimal heat gains by the incident heat flux countered by the larger combined losses of $Q_{b_{net}}$, Q_s, and Q_e (Figure 25). Overall the net heat flux produces a net heat gain of ~ 2x10^8 J m-^{2}, concluding that Hermit Lake is gaining more heat than it is losing over the course of the

study period. The large gains of heat by the incident heat flux are largely responsible for the overall gain of heat by the net heat flux.

2) FROG CALLS VS. METEOROLOGICAL DATA

Three out of the four frog species recorded at Hermit Lake, provide enough sound data during an 83 day recording period (Table 4) within the study period. These three frog species are the spring peeper, American toad, and green frog. The calling activity of the frogs is separated into 4 categories (Chapter 2, section *e*), thereafter the sound data is then compared to the heat flux data as well as the air temperature, surface water temperature, and wind speed data.

The air temperature at Hermit Lake has little effect on the spring peeper and green frog. However, the American toad did not call with air temperatures less than 8°C. When the air temperatures increase beyond this threshold, the toad's calling activity increases throughout the given range of temperatures. The American toad is unaffected by changes in the surface water temperature, but the spring peeper's and green frog's calling activity is affected by certain water temperatures. The Spring peepers are more likely to call with surface water temperatures that are less than 15°C and less likely to call when water temperatures exceed this threshold. The green frog is more likely to call with warmer water temperatures and less likely to call with temperatures below 18°C. In terms of wind speed and frog calling activity, this comparison provides some interesting results. The spring peeper is unaffected by changes in the wind speed, but the American toad's and green frog's calling activity are strongly sensitive to wind speed. The American toad is very active in terms of calling until wind speeds exceed ~ 5.2 m s^{-1} where all calling activity abruptly ceases. The green frog is actively calling until wind speeds exceed ~ 1.7

m s^{-1} and a gradual decrease in calling activity occurs until wind speeds exceed 6 m s^{-1}, where the green frog silences.

All three frog species are sensitive to the incident, blackbody, sensible, latent, and net heat fluxes. The American toad is more likely to call when the heat produced by the incident heat flux within the lake is below 3.8x10^{8} J m^{-2}. When the heat exceeds this threshold, the American toad calling activity immediately ceases. The spring peeper is actively calling with incident heat flux values less than 7x10^{8} J m^{-2}. When the heat increases beyond this value, the spring peeper calling activity gradually declines until the heat flux reaches 8.3x10^{8} J m^{-2}, where all calling by the spring peeper terminates. There is no calling by the green frog with Q_i values less than 1.5x10^{8} J m^{-2}. Calling activity then increases until the heat flux values reached 8x10^{8} J m^{-2}, where calling ceases once again.

The spring peeper is silent when the lake is experiencing strong cooling by the blackbody heat flux ($Q_{b_{net}}$). When $Q_{b_{net}}$ increases above -2.6x10^{8} J m^{-2}, the calling activity gradually increases until the values increase beyond -1.7x10^{8} J m^{-2}, where the spring peeper is very actively calling. The American toad is silent when the blackbody heat flux is below -1.3x10^{8} J m^{-2}. Once the values exceed -1.3x10^{8} J m^{-2}, American toad calling activity increases. For blackbody heat flux values less than -2.5x10^{8} J m^{-2} and greater than -1x10^{8} J m^{-2}, the green frog is silent. For values in between, which represent a moderate cooling of the lake, the green frog is actively calling.

For sensible heat flux values less than -5x10^{7} J m^{-2} and greater than -2x10^{7} J m^{-2} there is no calling by the green frog. In terms of the latent heat flux, there is no calling activity with values less than -3.1x10^{-8} J m^{-2} or greater than -0.5x10^{8} J m^{-2}. With these

results, it can be surmised that the green frog avoids calling when a strong cooling or minimal cooling effect occurs within the lake.

The American toad is silent when the sensible heat flux values are less than -2.5x10 ^{7} J m^{-2}. Calling activity increases once the loss of heat decreases beyond the sensible heat flux threshold. Similarly, the American toad is silent until the latent heat flux values increase above -1.25x10^{8} J m^{-2}. As with the green frog, the American toad is less likely to call when Hermit Lake experiences situations of strong cooling.

The spring peeper's calling activity increases when Hermit Lake is transitioning from strong cooling to minimal cooling situations. This species is silent with sensible heat flux values values less than -5x10^{7} J m^{-2}. Spring peeper calling activity then increases until Q_s values exceed -3.8x10^{7} J m^{-2} where the frogs are then extremely vocal. This same trend is also seen with the latent heat flux. No calling activity exists below -3.1x10^{8} J m^{-2}, but increases until the latent heat flux exceeds -2x10^{8} J m^{-2} , where the spring peeper's calling activity drastically increases.

The different frog species' reaction to the net heat flux in terms of calling activity reveals how the frogs react to the net heating or cooling of the lake. The spring peeper and green frog are both very actively calling until the net heat flux reaches 2x10^{8} J m^{-2}, beyond this both frog species are silent. However, the green frog does not call with net heat flux values below 0.5x10^{8} J m^{-2} as well. The American toad only calls when there is a minimal gain of heat by Hermit Lake, as calling activity ceases once the net heat flux reaches 0.8x10^{8} J m^{-2}. The results discussed above are preliminary and further research is necessary to better understand the relationship between the frog calls and the various meteorological variables and heat fluxes.

b. Conclusion

An extensive study is performed at Hermit Lake from May 26, 2010 at 1515 GMT till November 7, 2010 at 0330 GMT to determine the effects of the five individual heat fluxes on Hermit Lake and the surrounding amphibian community. The incident heat flux (Q_i) is the dominate term within the net heat flux (Q_n) throughout the course of the study until fall. Lower solar elevation angles and an increase in cloudiness contribute to minimal incident heat flux values beyond fall. However, the incident flux continues to produce a large net gain of heat even with the lack of sunlight, revealing a storage effect of heat within the lake.

The blackbody heat flux ($Q_{b_{net}}$) produces a loss of heat for most of the study period until mid to late fall. Three distinct events occur when the blackbody produces a gain of heat. It is speculated that these three events are associated with the warm sector of mid-latitude cyclone. In this area a warm, moist airmass is present over Hermit Lake aiding in a positive blackbody heat flux.

The largest contributor to the net heat flux in terms of a heat loss is the latent heat flux (Q_e). Over the course of the study period, Q_e is negative with some losses measuring at ~ -300 W m^{-2}. Most of these losses are most likely due to warm, dry air masses over the lake. As the summer transitions into fall, the latent heat flux gradually increases. It is hypothesized that fairly warm and moist airmasses traversed through Hermit Lake, most common with the western side of high pressure systems. As for the sensible heat flux (Q_s), it is the smallest of all three heat fluxes with a minimal heat loss of ~ -2x10^8 J m^{-2}. However, with the onset of late fall, the heat loss due to the sensible heat flux increases.

The sum of the four individual fluxes creates the net heat flux. Over the course of the study period, Q_n is highly variable and mostly positive due to the incident heat flux. There are however times when the combined losses by $Q_{b_{net}}$, Q_s, and Q_e are greater than the gains by the incident heat flux. With the onset of fall, Q_n becomes less variable and smaller, most likely due to the smaller incident heat flux values during the fall.

Overall Hermit Lake experiences a ~ $2x10^8$ J m^{-2} gain of heat. On October 1, 2010, a gradual decline in heat occurs through the end of the study period. This decline is most likely caused by the minimal gains in the incident heat flux and the large combined losses of the sensible, latent, and blackbody heat fluxes.

Certain water temperature thresholds affect the calling activity of the spring peeper and green frog, while higher wind speeds have a dramatic effect on the calling activity of both the green frog and American toad. What is more interesting is that the three frog species phenological activities are affected by thresholds in the incident, blackbody, latent, sensible, and net heat fluxes.

c. Future work

First and foremost the study period needs to be extended. This study is limited by memory limits within the water temperature sensors, thereby limiting surface water temperature data. To gain a full understanding of the heat flux behavior within Hermit Lake, a period of at least one year or more must be examined. A one year study will allow for a more comprehensive examination of the monthly and seasonal effects and behaviors of each heat flux. A more accurate picture of the net heat gain or loss can also be ascertained from a yearlong study. From the results provided in this present study, it

can only be determined that Hermit Lake experiences a net gain of heat for the roughly five and a half month long study period.

Secondly, a more reliable cloud cover dataset needs to be generated and used for future studies. A major source of error for this study is found in the synthesized cloud cover dataset that is generated and utilized. Next, recall that there are no peaks present above the 95% confidence interval in the spectral analysis of the sensible heat flux time series. It is inferred that the air and water temperatures are not behaving as would be expected. A future study into the microscale interactions between the water temperatures, air temperatures, wind speed, and wind direction as well as the synoptic systems that create these interactions, can provide insight into how these variables all interact with one another.

Finally, it has been revealed that the multiple frog species in and around Hermit Lake are sensitive to the different heat fluxes. A closer and more detailed examination is necessary to further understand the interaction between the frog species and the heat fluxes. Some suggestions include measuring and examining water temperatures from known breeding areas of the different frogs within the lake, extending the frog sound collection period to match the heat flux study period, and closely monitoring individual heat flux changes prior to and during known breeding periods of the different frog species.

APPENDIX A

Full Calculations of the Heat Fluxes and Associated Uncertainties at Hermit Lake

a. Calculations

1) NET HEAT FLUX

According to Pickard and Emery (1982), the net air-sea heat flux is given by:

$$Q_n = Q_i + Q_{b_{net}} + Q_s + Q_e \quad \textbf{(A1)}$$

where Q_n is the net vertical heat flux (W m^{-2}), Q_i is the shortwave radiational (incident) heat flux, $Q_{b_{net}}$ is the net longwave radiational (blackbody) heat flux, Q_s is the conductive (sensible) heat flux, and Q_e is the evaporative (latent) heat flux. Each of these terms is in turn a complex function. Positive values indicate heat flux into the water, while negative values indicate heat flux out of the water. This air-sea heat flux equation can also be used for air-water heat flux in lakes with some adjustments made to each term.

2) INCIDENT SHORTWAVE HEAT FLUX

The incident heat flux is given by:

$$Q_i = (1 - Ab) I_{sw} \quad \textbf{(A2)}$$

where Ab is the water-surface albedo (unitless), and I_{sw} is the measured incoming shortwave radiation (W m^{-2}) (Rogers *et al*. 1995).

The albedo for a body of water with infinite depth (Ab_∞) is a function of atmospheric transmittance (Tr) and solar elevation angle (θ), quantified in tabular form by Payne (1972). Tr is a dimensionless number between 0 and 1, and is given by:

$$Tr = \frac{I_{sw}\gamma^2}{S\sin(\emptyset)}$$

(A2.1)

where γ is the multiple of the mean Earth-Sun distance (a number approximately equal to one), S is the solar "constant" (1353 W m^{-2}), and $\emptyset$ is terrestrial latitude (degrees) (Payne 1972). According to Miller (1999), the Earth-Sun distance multiple (γ) is calculated via:

$$\gamma = 1.00011 + 0.034221\cos(\alpha) + 0.00128\sin(\alpha) + 0.000719\cos(2\alpha) + 0.000077\sin(2\alpha)$$

(A2.2)

where α is the day angle, which is in turn calculated by:

$$\alpha = \frac{2\pi(N-1)}{365}$$

(A2.3a)

$$\alpha = \frac{2\pi(N-1)}{366}$$

(A2.3b)

where N is the Julian day. Equation A2.3b is used for leap years, and (A2.3a) for normal years (Miller 1999).

The solar elevation angle (θ) (degrees) is calculated by:

$$\theta = 90 - \text{acos}(\cos(Z))$$

(A2.4)

where the zenith angle (Z) is calculated by:

$$\cos(Z) = \sin(\emptyset)\sin(\sigma) + \cos(\emptyset)\cos(\sigma)\cos(H)$$

(A2.5)

where $\emptyset$ is the terrestrial latitude (degrees), σ is a function of the day angle, and H is the hour angle (degrees) (Cogley 1979). σ and H are calculated by:

$$\sigma = 0.006918 - 0.399912\cos(\alpha) + 0.070257\sin(\alpha) - 0.006758\cos(2\alpha) + 0.000907\sin(2\alpha) - 0.002697\cos(3\alpha) + 0.00148\sin(3\alpha)$$

(A2.6a)

$$H = 15.0\ (12.0 - Hour)$$

(A2.6b)

where Hour is the decimal hour in local standard time (LST), and α is the day angle (Miller 1999).

In order to calculate the albedo of an unfrozen body of water with finite depth, the albedo of an infinitely deep water body (Ab_∞) (unitless) must be calculated. Ab_∞ is calculated by:

$$Ab_\infty = p_1(1 + p_2x + p_3x^2 + p_4x^3)\left(1 + p_5\frac{1}{\cos(Z)}\right)(1 + p_6W)x$$

(A2.7)

where W is the surface wind (m s^{-1}), Z is the zenith angle (degrees), and p_1 through p_6 are coefficients for the irradiance reflectance of deep water (Table A1) empirically determined by Albert and Mobley (2003). x is calculated by:

$$x = \frac{b_b}{a + b_b}$$

(A2.8)

where b_b is the backscattering coefficient of pure water and a is the absorption coefficient of pure water. Albert and Mobley (2003), used wavelengths 400 to 750 nm in their simulations for a and b_b. For a, the values range from 0.0106 ± 0.0070 and for b_b, the values range from 0.0053 ± 0.0004 (Pegau *et al*. 2002).

Table A1. Coefficients for the albedo of deep water for Equation A2.7.

Coefficient	Value
p_1	0.1034 ± 0.0014
p_2	3.3586 ± 0.0305
p_3	-6.5358 ± 0.0808
p_4	4.6638 ± 0.0649
p_5	2.4121 ± 0.0443
p_6	-0.0005 ± 0.0001

The albedo (Ab) (unitless) of a water body with finite depth is calculated by:

$$Ab = B_C\left(Ab_\infty\left[1 - A_1 exp\left\{-\left(\frac{k_0}{\cos(Z)} + (1+x)^{k_{1,W}}\left(1 + \frac{k_{2,W}}{\cos(Z)}\right)\right)(a+b_b)D_B\right\}\right] + A_2 Ab_B exp\left\{-\left(\frac{k_0}{\cos(Z)} + (1+x)^{k_{1,B}}\left(1 + \frac{k_{2,B}}{\cos(Z)}\right)\right)(a+b_b)D_B\right\}\right)$$

(A2.9)

where B_C is the cloud correction factor (Churchill and Kerfoot 2007). Ab_∞ is the albedo of an infinitely deep water body (A2.7), A_1, A_2, k_0, $k_{1,W}$, $k_{2,W}$, $k_{1,B}$, and $k_{2,B}$ are empirically determined coefficients for the irradiance reflectance for shallow water (Table A2) (Albert and Mobley 2003). Z is the zenith angle (degrees), D_B is the bottom depth in meters, a is the absorption coefficient of water (see above), b_b is the backscattering coefficient of pure water (see above), and Ab_B is the albedo of the bottom surface of a shallow body of water. According to Leathers and McCormick (1999), the value of Ab_B ranges from 0 to 0.4 for natural waters.

The cloud correction factor (B_C) can be determined by using the formula from Churchill and Kerfoot (2007):

$$B_C = (1 - 0.72C)$$

(A2.10)

where C is the fraction of sky obscured by clouds in eighths determined from observations. If the observed cloud cover (C) increases, then B_C will decrease thereby having a lesser effect on the albedo. The opposite is true if the observed cloud cover decreases.

Table A2. Coefficients for the albedo of shallow water for Equation A2.9.

Coefficient	Value
A_1	1.0546 ± 0.0038
k_0	1.0546 ± 0.0001
$k_{1,W}$	1.9991 ± 0.0305
$k_{2,W}$	0.2995 ± 0.0122
A_2	0.9755 ± 0.0013
$k_{1,B}$	1.2441 ± 0.0209
$k_{2,B}$	0.5182 ± 0.0036

According to Rogers *et al.* (1995), the albedo (Ab) for a frozen mid-latitude lake is given by:

$$Ab = \Delta Ab_{s,a} + \Delta Ab_{s,m} + \Delta Ab_{\beta} + \Delta Ab_{C} \quad \textbf{(A2.11)}$$

where $\Delta Ab_{s,a}$ is the change in albedo due to accumulating snow, $\Delta Ab_{s,m}$ is the change in albedo due to melting snow, ΔAb_{β} is the change in albedo via the solar noon angle, and ΔAb_{C} is the change in albedo due to the total fraction of cloud cover. Following Rogers *et al.* (1995), the albedo is set at a base value of 0.84, following each snowfall. This base value is then modified accordingly. Figure A1 displays the necessary steps taken in calculating the albedo after each new snowfall.

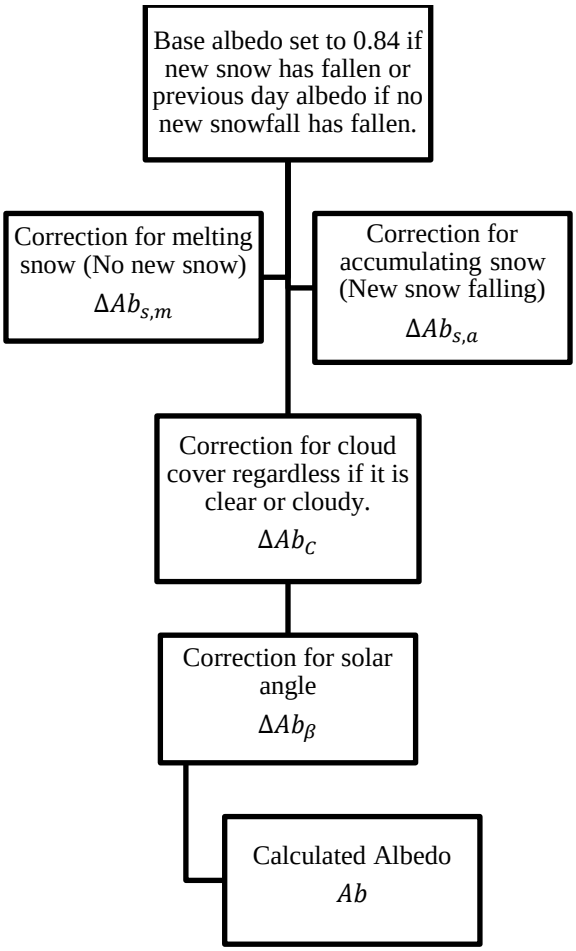

Figure A1. Albedo calculation chart for Equations A2.11 – A2.14 for a frozen lake.

The change in albedo due to accumulating or melting snow is given by:

$$\Delta Ab_{s,a} = -10^{-(1.22+0.69d)} \qquad d = 1, 2, 3, \ldots, n \text{ (accumulating)}$$

$$\Delta Ab_{s,m} = -10^{-(0.95+0.07d)} \qquad d = 1, 2, 3, \ldots, n \text{ (melting)} \qquad \textbf{(A2.12)}$$

where $\Delta Ab_{s,a}$ is the change in albedo via snow accumulation and $\Delta Ab_{s,m}$ is the change in albedo via snow melting. Both terms represent the change in albedo in terms of the number of days, d, since the last snowfall. Albedo also decreases with increasing solar elevation. This change in albedo is expressed as:

$$\Delta Ab_{\beta} = -0.019 + 0.248\left[exp\left(\frac{-\beta}{15.5}\right)\right]$$

(A2.13)

where β is the solar noon angle in degrees. β is given by:

$$\beta = 90 - Z$$

(A2.14)

where Z is the zenith angle (degrees). Cloud cover must also be factored into the total change in albedo. The change in albedo due to cloud cover (ΔAb_C) is expressed as:

$$\Delta Ab_C = 0.00449 + 0.097C^3$$

(A2.15)

where C is the fraction of the sky obscured by clouds in eighths. Here C was determined from an empirical relationship expressing cloud cover in terms of observed cloud cover and theoretical clear-sky solar radiation (Rogers *et al.* 1995).

3) BLACKBODY HEAT FLUX

The net longwave (blackbody) radiational heat flux for an unfrozen lake is given by:

$$Q_{b_{net}} = Q_{b_1} + Q_{b_2} + Q_{b_3}$$

(A3)

where Q_{b_1} is a downwelling term and is therefore a radiational gain for the lake while Q_{b_2} and Q_{b_3} are both considered upwelling terms and are therefore radiational losses for the lake (Budyko 1971; Churchill and Kerfoot 2007). Q_{b_1} is given by:

$$Q_{b_1} = \varepsilon\sigma T_s^4(0.05e^{0.5})B_C$$

(A3.1)

where ε is the emissivity of the water-surface (0.985), σ is the Stefan-Boltzmann constant (5.673×10^{-8} W m^{-2} K^{-4}), T_s is the surface water temperature (Kelvins), e is the vapor pressure (millibars), and B_C is the cloud correction factor found using Equation A2.10

(Churchill and Kerfoot 2007). According to Petty (2008), the vapor pressure (e) can be determined by utilizing the Clausius-Clapeyron equation:

$$e = e_0 exp\left[\left(\frac{L_V}{R_V}\right)\left(\frac{1}{T_0} - \frac{1}{T_d}\right)\right] \quad \textbf{(A3.2)}$$

where e_0 is the reference pressure of water found experimentally to be 611.12 Pascals, L_V is the latent heat of vaporization (J kg^{-1}), R_V is the specific gas constant of water vapor (461.5 J kg^{-1} K^{-1}), T_0 is the reference temperature for e_0 (273.16 Kelvins), and T_d is the dewpoint temperature (Kelvins) (Petty, 2008).

The latent heat of vaporization (L_V) is calculated by:

$$L_V = L_{V0} - 2369T \quad \textbf{(A3.3)}$$

where L_{V0} is the value of L_V at 0°C, taken as 2.5x10^6 J kg^{-1}, and T is the temperature in Celsius (Miller 1999).

Q_{b_2} is given by:

$$Q_{b_2} = -\varepsilon\sigma T_s^4(0.39)B_C \quad \textbf{(A3.4)}$$

where ε is the emissivity of the water-surface (0.985), σ is the Stefan-Boltzmann constant (5.673x10^{-8} W m^{-2} K^{-4}), T_s is the surface water temperature (Kelvins), 0.39 is an empirically derived value, and B_C is the cloud correction factor found using Equation A2.10 (Churchill and Kerfoot 2007).

Q_{b_3} is given by:

$$-4\varepsilon\sigma T_s^3(T_s - T_a) \quad \textbf{(A3.5)}$$

where ε is the emissivity of the water-surface (0.985), σ is the Stefan-Boltzmann constant (5.673×10^{-8} W m^{-2} K^{-4}), T_s is the surface water temperature (Kelvins), and T_a is the air temperature directly above the lake (Kelvins).

The blackbody heat flux for a frozen lake can be determined by utilizing the formula from Duguay *et al.* (2003) and Maykut and Church (1973):

$$Q_b = \varepsilon_A \sigma T_a^4 B_C - \varepsilon_i \sigma T_i^4 \quad \textbf{(A3.6)}$$

where ε_A is the atmospheric emittance (0.7855) (unitless) (Key *et al*. 1996), σ is the Stefan Boltzmann constant, T_a is the air temperature (Kelvins), B_C is the cloud correction factor determined from Equation A2.10, ε_i is the emissivity of ice (0.97) (unitless) (Launiainen and Cheng 1998), and T_i is the surface temperature of the ice (Kelvins). The first term on the right hand side represents the downwelling longwave radiation while the second term on the right hand side represents the upwelling longwave radiation. The vapor pressure of ice is minute and ranges from 0.1 to 6 hPa at temperatures of -40 to 0°C (Lide 1997). Therefore the vapor pressure will have a minimal effect on the blackbody heat flux of a frozen lake and can be omitted from Q_b.

4) SENSIBLE HEAT FLUX

According to Miller (1999), the sensible heat flux through a water-surface is given by:

$$Q_s = -\rho_a c_p C_S (T_s - T_a) W \quad \textbf{(A4)}$$

where ρ_a is the density of moist air (kg m^{-3}), c_p is the specific heat coefficient of moist air at constant pressure (J kg^{-1} K^{-1}), C_s is the sensible heat transfer coefficient (Stanton

number), T_s and T_a are the temperatures of the water-surface and the air immediately above the water-surface (Celsius), and W is the wind speed (m s^{-1}).

The ideal gas law is used to calculate the density of the moist airmass:

$$\rho_a = \frac{p}{R_d T_v} \quad \textbf{(A4.1)}$$

where p is the atmospheric pressure (Pascals), R_d is the specific heat constant of dry air (287 J kg^{-1} K^{-1}), and T_v is the virtual temperature (Kelvins) (Petty 2008). Virtual temperature (T_v) (Kelvins) is in turn calculated by:

$$T_v = T\left(\frac{1 + \frac{w}{\varepsilon}}{1 + w}\right) \quad \textbf{(A4.2)}$$

where ε is the ratio of the mean molecular weight of water to the mean molecular weight of dry air (0.62197), w is the mixing ratio of water vapor to dry air, and T is the dry air temperature (Kelvins) (Miller 1999). The mixing ratio (w) is calculated by:

$$w = \frac{\varepsilon e}{p - e} \quad \textbf{(A4.3)}$$

where e is the vapor pressure (Pascals) and p is the atmospheric pressure (Pascals) (Petty 2008). Any units of e and p are allowable, provided they are the same units (Miller 1999).

The specific heat coefficient of moist air is calculated by:

$$c_p = c_{p0}\left(\frac{1 + w\left(\frac{c_{pv}}{c_{p0}}\right)}{1 + w}\right) \quad \textbf{(A4.4)}$$

where c_{p0} is the value of c_p at zero relative humidity (1004.6 J kg^{-1} K^{-1}), w is the water vapor mixing ratio, and c_{pv} is the specific heat constant of water vapor (1870 J kg^{-1} K^{-1}) (Rogers and Yau 1989).

The sensible heat transfer coefficient (C_s) also known as the Stanton number is calculated by:

$$C_s = \begin{cases} W < 8\ m\ s^{-1}: (0.720 + [0.0175W(T_s - T_a)]) \times 10^{-3} \\ W \geq 8\ m\ s^{-1}: (1.000 + [0.0015W(T_s - T_a)]) \times 10^{-3} \end{cases} \quad \textbf{(A4.5)}$$

where W is the wind speed (m s^{-1}), T_s is the water-surface temperature (°C), and T_a is the temperature of the airmass (°C) (Wu 1992).

5) LATENT HEAT FLUX

The latent heat flux is given by:

$$Q_e = -\rho_a L_V C_e (q_s - q_a) W \quad \textbf{(A5)}$$

where ρ_a is the density of the moist air (kg m^{-3}), L_V is the latent heat of vaporization (J kg^{-1}), C_e is the evaporative heat transfer coefficient (Dalton number), q_s and q_a are the specific humidities at the water-surface and the air immediately above the water-surface, and W is wind speed (m s^{-1}) (Miller 1999).

The calculations of the density of the airmass (ρ_a) and the latent heat of vaporization (L_V) are as described above. The evaporative heat transfer coefficient (Dalton number) is a constant value equal to 1.5x10^{-3}. Specific humidities are calculated by:

$$q = \frac{\varepsilon e}{p - (1 - \varepsilon)e} \quad \textbf{(A5.1)}$$

where p is the atmospheric pressure, e is the vapor pressure, and ε is the ratio of the mean molecular weight of water to the mean molecular weight of dry air (0.62197) (Petty 2008). Any units for p and e are permissible, provided they are the same units (Miller 1999).

b. Uncertainty Estimates.

The net uncertainty (imprecision) in a composite function (those consisting of more than one term, each with its own uncertainty) is estimated by:

$$\sigma_T = \sqrt{\sum_i^n \sigma_i^2} \quad \textbf{(A6)}$$

where σ_T is the total estimated uncertainty, σ_i is the uncertainty associated with an individual term, and n is the number of terms in the function.

The maximum uncertainties in the air-water heat flux series are estimated as follows:

• Incident heat flux (Q_i) is a function of albedo (Ab) and the measured incident shortwave radiation field (I_{sw}). According to the method outlined in Payne (1972), Ab is primarily a function of atmospheric transmittance (Tr) and solar elevation angle (θ). For high Sun angles, Payne's method yields an Ab uncertainty of $\pm$ 7.0 percent, and for low Sun angles, $\pm$ 25 percent. Since the important contributions by Q_i occur at high Sun angles, Miller (1999) suggests using the smaller uncertainty estimate. The uncertainty in I_{sw} is on the order of $\pm$ 5.0 percent and is associated with the Apogee SP-110 Precision

Pyranometer used for this study (Doner 2011). Thus the combined maximum uncertainty associated with Payne's method for Q_i is conservatively estimated at $\pm$ 10 percent.

- The albedo for an infinitely deep unfrozen lake (Ab_∞) is a function of wind speed (W), zenith angle (Z), and the empirically determined coefficients for the irradiance reflectance of deep water ($p_1$through p_6). According to Albert and Mobley (2003), the uncertainty in Ab_∞ is $\pm$ 4.0 percent. For situations of high backscattering due to high concentrations of suspended matter, the uncertainty is reduced to less than $\pm$ 1.0 percent. The wind speed (W) is measured using the R.M. Young Model 05103-45 Alpine Wind Monitor. According to the R. M. Young Company (2011), the maximum uncertainty associated with the Alpine Wind Monitor is $\pm$ 1.0 percent Thus the combined uncertainty for Ab_∞ is estimated to be $\pm$ 3.0 percent by Albert and Mobley (2003).

- The albedo of an unfrozen lake of finite depth (Ab) is a function of the albedo of an infinitely deep lake (Ab_∞), zenith angle (Z), bottom depth of the lake (D_B), the albedo of the bottom depth (Ab_B), the cloud correction factor (B_C), and the empirically determined coefficients for the irradiance of reflectance of shallow water ($A_1,\ A_2,\ k_0,\ k_{1,w},\ k_{2,w},\ k_{1,B},\ k_{2,B}$). According to Gleckler and Weare (1997), the uncertainty associated with B_C is on the order of $\pm$ 25 percent. Albert and Mobley (2003), state that the uncertainty in Ab alone is $\pm$ 2.0 percent. If the albedo is associated with wavelengths from 660 to 715 nm, there is an added uncertainty of -12.0 percent. This uncertainty is due to the influence of chlorophyll fluorescence. Overall the mean uncertainty for Ab is estimated to be $\pm$ 25.0 percent. Thus the combined uncertainty for the method used to calculate Q_i for this study is conservatively estimated to be ± 26.0 percent.

- The albedo of a frozen lake (Ab) has four components to it. Those components include: the change in albedo due to melting snow ($\Delta Ab_{s,m}$), the change in albedo due to accumulating snow ($\Delta Ab_{s,a}$), the change in albedo due to the solar noon angle (ΔAb_{β}), and the change in albedo due to cloud cover (ΔAb_{C}). According to Petzold (1977), the combined uncertainty associated with the calculation of Ab is estimated to be $\pm$ 10 percent.

- Blackbody heat flux ($Q_{b_{net}}$) for an unfrozen lake is a function of the water surface emissivity (ε), the water-surface temperature (T_s) raised to the fourth power and third power, the cloud correction factor (B_C), and the air temperature (T_a). The YSI 600LS Level Sonde is used to measure T_s for this study. This instrument has an associated uncertainty of approximately $\pm$ 0.5 percent (Doner 2011). According to Miller *et al*. (1999), the uncertainty associated with ε is on the order of ± 1.0 percent. T_a has a random error that represents the error in the reading of the thermometer or any bias that the instrument may have. This error has been estimated to be on the order of $\pm$1.0 percent (Gleckler and Weare 1997).

By raising T_s to the fourth power, its associated error increases by approximately an order of magnitude, to ± 1.0 percent (Miller 1999). According to Gleckler and Weare (1997), the uncertainty associated with B_C is on the order of $\pm$ 25 percent. Thus the maximum uncertainty associated with the Q_b of an unfrozen lake is estimated to be $\pm$ 25 percent.

- Blackbody heat flux (Q_b) for a frozen lake is a function of atmospheric emittance (ε_A), the air temperature (T_a) raised to the fourth power, the cloud correction factor (B_C), the emissivity of ice (ε_i), the Stefan Boltzmann constant (σ), and the temperature of the ice-surface (T_i) raised to the fourth power. According to Key *et al.*

(1996) and Gleckler and Weare (1997), the first term on the right hand side of Q_b for a frozen lake has an estimated uncertainty of $\pm$ 30 percent.

The second term on the right hand of Q_b contains T_i, σ, and ε_i. When the lake is frozen, the YSI 600LS Level Sonde continues to record the temperature of the ice itself. Therefore the uncertainty of $\pm$ 0.5 percent, which is associated with the temperature of the water, can be applied to the temperature of the ice. However, raising T_i to the fourth power increases the error by an order of magnitude to $\pm$ 5.0 percent. The error associated with ε_i is assumed to be on the order of $\pm$ 1.0 percent. Therefore the maximum uncertainty associated with Q_b of a frozen lake is estimated to be $\pm$ 30 percent.

• Sensible heat flux (Q_S) is a function of the density of the air (ρ_a), the specific heat coefficient of air at constant pressure (c_p), the sensible heat transfer coefficient (C_S), the air and water-surface temperatures (T_s and T_a), and the wind speed (W). The air and water-surface temperatures have associated uncertainties of $\pm$ 1.0 percent and $\pm$ 0.3 percent.

W is measured directly at the Hermit Lake station and is recorded as 5-minute averages. W has an estimated maximum uncertainty of approximately $\pm$ 1.0 percent (see above). ρ_a is a function of T_a, relative humidity (RH), and sea-level pressure (SLP), and has a combined estimated uncertainty of $\pm$ 1.0 percent. c_p is a function of T_a and RH, and has an estimated maximum uncertainty of $\pm$ 1.0 percent. C_S is a function of W, T_a and T_s, and also has a maximum combined uncertainty of $\pm$ 1.0 percent (Miller 1999). Therefore, the uncertainty for Q_s, yields a net maximum estimated uncertainty of $\pm$ 2.0 percent.

• Latent heat flux (Q_e) is a function of ρ_a, the latent heat of vaporization (L_V), the evaporative heat transfer coefficient (C_e), specific humidities of the air and near the water-surface (q_a and q_s), and W. q_a and q_s are in turn functions of sea-level pressure, T, and RH, and have a combined estimated maximum uncertainty of $\pm$ 1.0 percent. ρ_a has a similar uncertainty of $\pm$ 1.0 percent. The transfer coefficient (C_e) is a fixed

constant and is assumed to have zero uncertainty. The function used for calculating L_V reproduces tabulated experimental values almost exactly when the temperature is near zero Celsius, thus, its error was conservatively estimated at $\pm$ 1.0 percent (Miller 1999). Therefore, the net maximum uncertainty for Q_e is estimated to be $\pm$ 2.0 percent.

• Uncertainties in the two summation series Q_{emr}, (which is the term-by-term sum of Q_i and Q_b) and Q_n (which is the sum of all four heat flux components), are estimated by taking the square root of the sum of the squares of the uncertainties of the component series.

Tables A3 & A4. Summary of air-water heat flux uncertainties.

Heat Flux Series For a Frozen Lake	**Abbr.**	**Uncertainty [%]**
Incident	Q_i	$\pm$ 14
Blackbody	Q_i	$\pm$ 30
Total EMR ($Q_b + Q_i$)	Q_{emr}	$\pm$ 33
Latent	Q_e	$\pm$ 2.0
Sensible	Q_S	$\pm$ 2.0
Net	Q_n	$\pm$ 33

Heat Flux Series For an Unfrozen Lake	**Abbr.**	**Uncertainty [%]**
Incident	Q_b	$\pm$ 26
Blackbody	Q_i	$\pm$ 25
Total EMR ($Q_b + Q_i$)	Q_{emr}	$\pm$ 36
Latent	Q_e	$\pm$ 2.0
Sensible	Q_S	$\pm$ 2.0
Net	Q_n	$\pm$ 36

APPENDIX B

Meteorological and Heat Flux Data Comparisons to Frog Calling Intensity

This appendix includes the full suite of figures of the heat flux and meteorological data compared to the frog calling intensity recorded from Hermit Lake, one hour after sunset each night from May 26, 2010 until August 16, 2010. Four frog species were recorded at Hermit Lake including the spring peeper (*Pseudacris crucifer),* wood frog (*Lithobates sylvaticus*), American toad (*Anaxyrus americanus*), and green frog (*Lithobates clamitans*) (Smyers and Jones 2008; Smyers 2011; personal communication). The blue boxes highlight areas of calling activity, red boxes highlight areas of no recorded calling activity, green circles mark data points that are suspected outliers, and the solid red lines separate intervals of increasing or decreasing calling activity. Frog species that present a lack of sensitivity to a meteorological variable or heat flux or there is an insufficient number of actively calling days are represented in figures with no markings. The number of actively calling days during the recording period is marked at the top of each figure by N.

a. Spring peeper

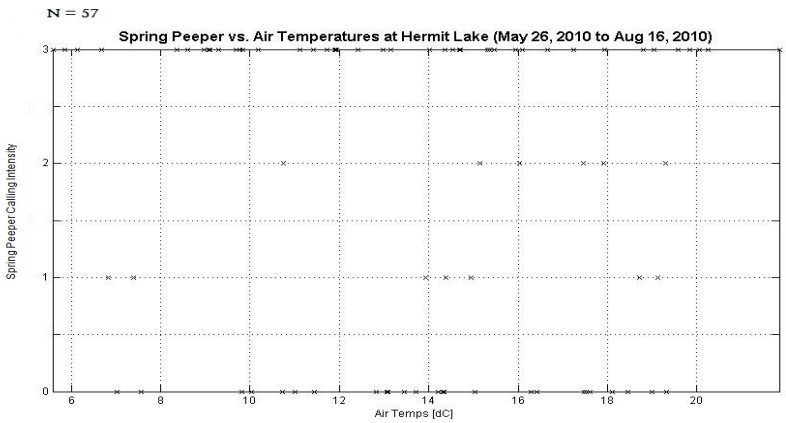

Figure B1. Comparison of air temperature data and spring peeper calling intensity. The spring peeper is unaffected by changes in air temperature.

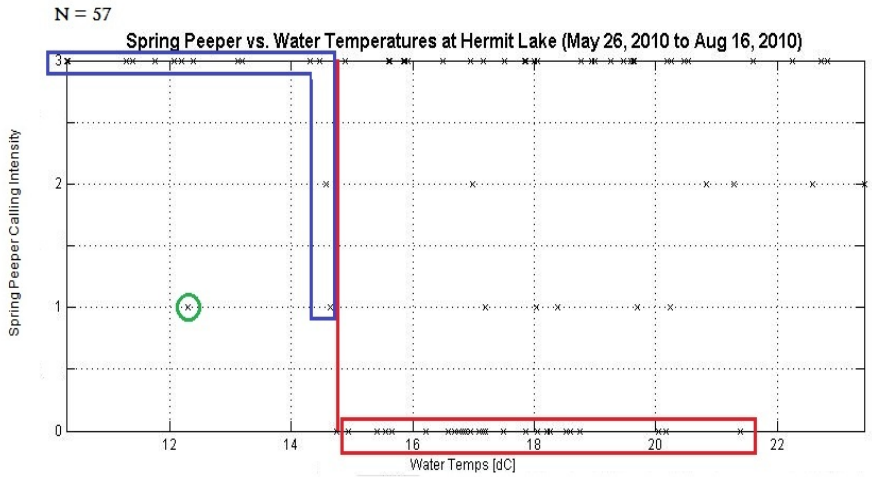

Figure B2. Comparison of the surface water temperature data and spring peeper calling intensity. Spring peeper calling activity decreases once water temperatures exceed 15°C.

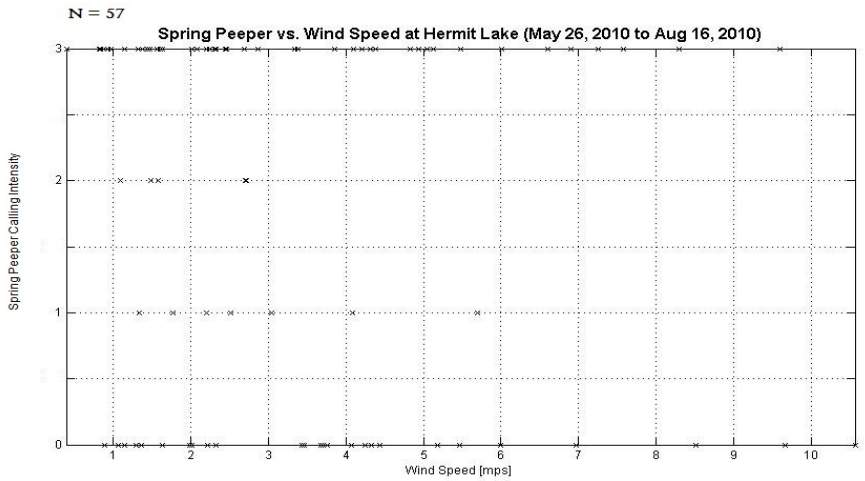

Figure B3. Comparison of the wind speed data and spring peeper calling intensity. The spring peeper is unaffected by changes in the wind speed.

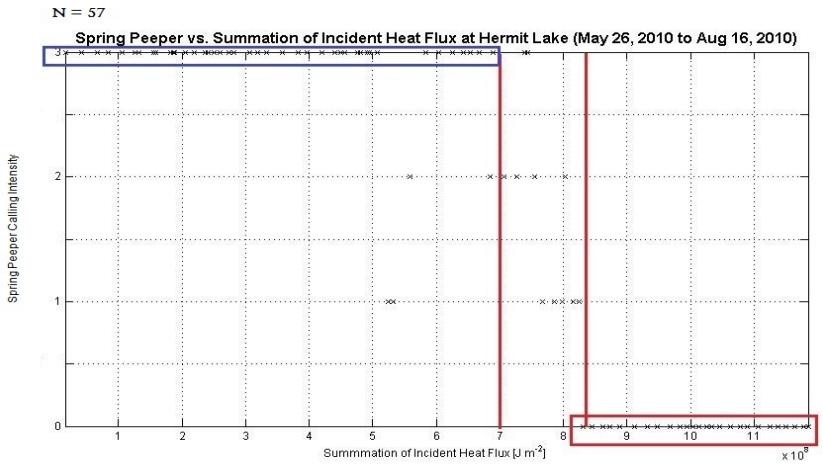

Figure B4. Comparison of the incident heat flux summation and spring peeper calling intensity. The area between $7x10^8$ J m^{-2} and $8.3x10^8$ J m^{-2} marks the transition zone from actively calling to silence.

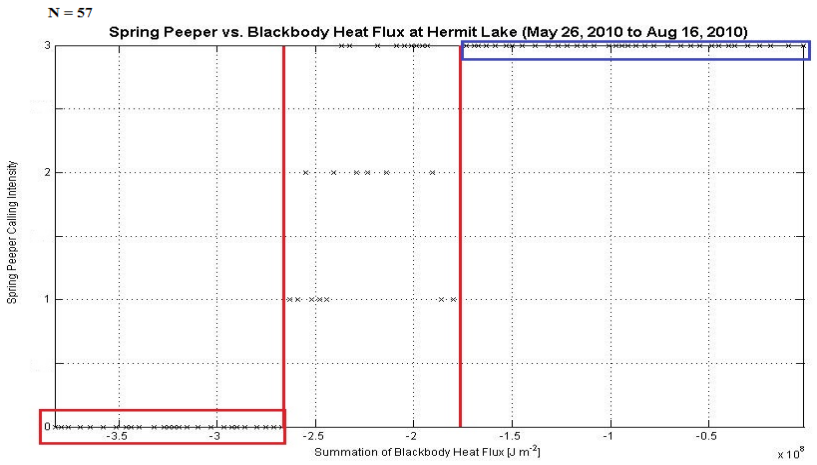

Figure B5. Comparison of the blackbody heat flux summation and spring peeper calling intensity. The area between -2.6×10^8 J m^{-2} and -1.7×10^8 J m^{-2} marks the transition zone from silence to calling.

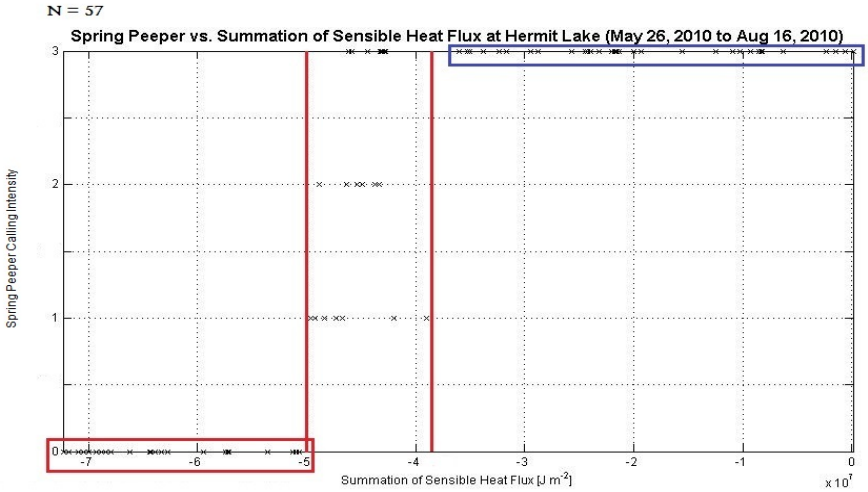

Figure B6. Comparison of the sensible heat flux summation and spring peeper calling intensity. The area between -5×10^7 J m^{-2} and -3.8×10^7 J m^{-2} marks the transition zone from silence to actively calling.

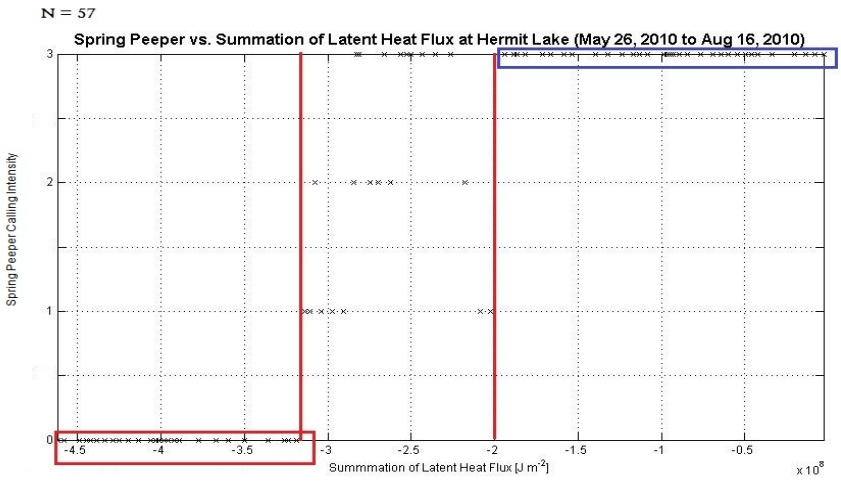

Figure B7. Comparison of the latent heat flux summation and spring peeper calling intensity. The area between -3.1×10^8 J m^{-2} and -2×10^8 J m^{-2} marks the transition zone from silence to actively calling.

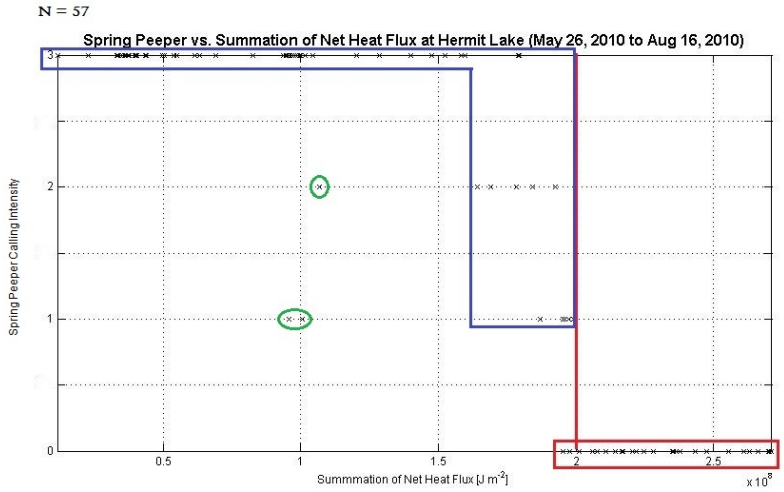

Figure B8. Comparison of the net heat flux summation and spring peeper calling intensity. Spring peeper calling activity ceases once the net heat flux summation exceeds $2x10^8$ J m^{-2}.

b. Wood frog

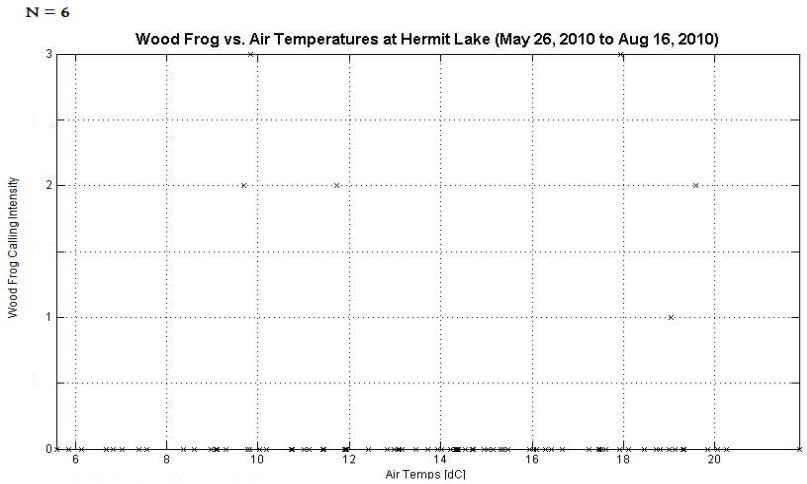

Figure B9. Comparison of the air temperature data to the wood frog calling intensity. There is insufficient calling activity data.

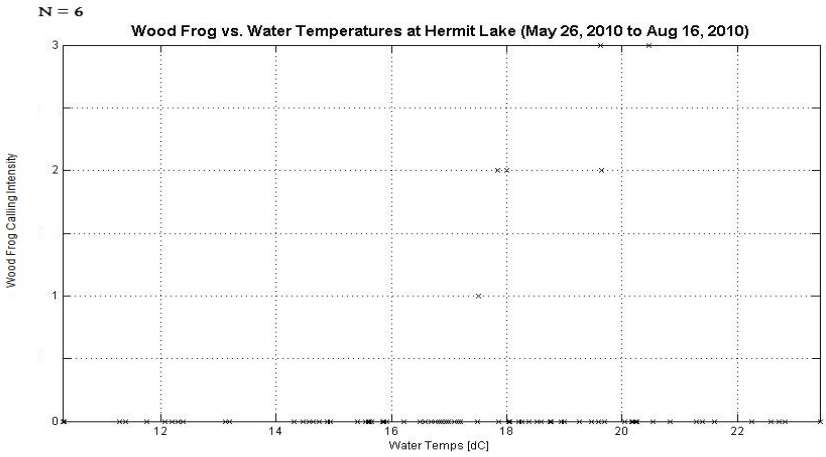

Figure B10. Comparison of the surface water temperature data to the wood frog calling intensity. There is insufficient calling activity data.

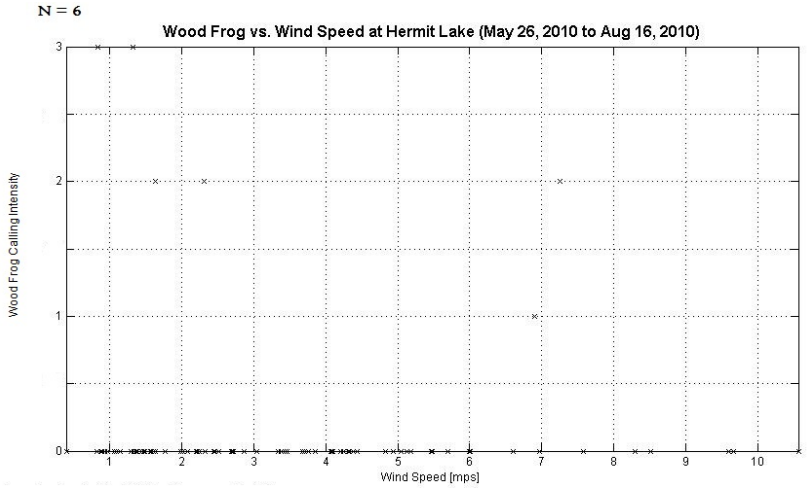

Figure B11. Comparison of the wind speed data to the wood frog calling intensity. There is insufficient calling activity data.

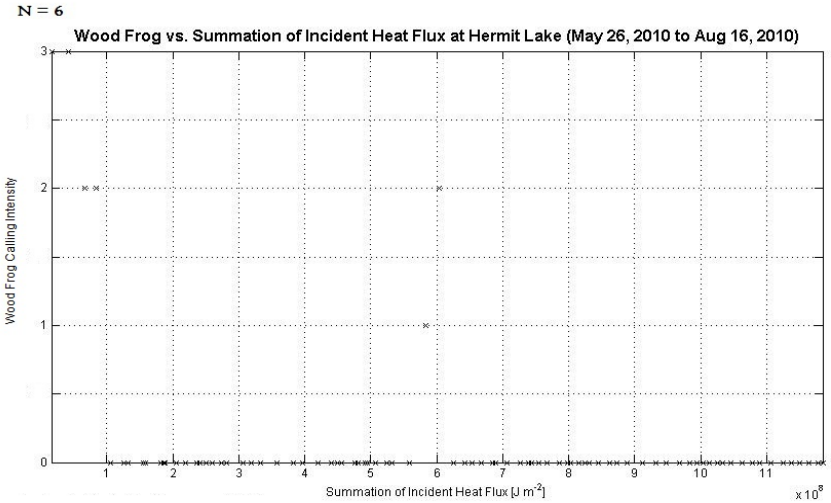

Figure B12. Comparison of the incident heat flux data to the wood frog calling intensity. There is insufficient calling activity data.

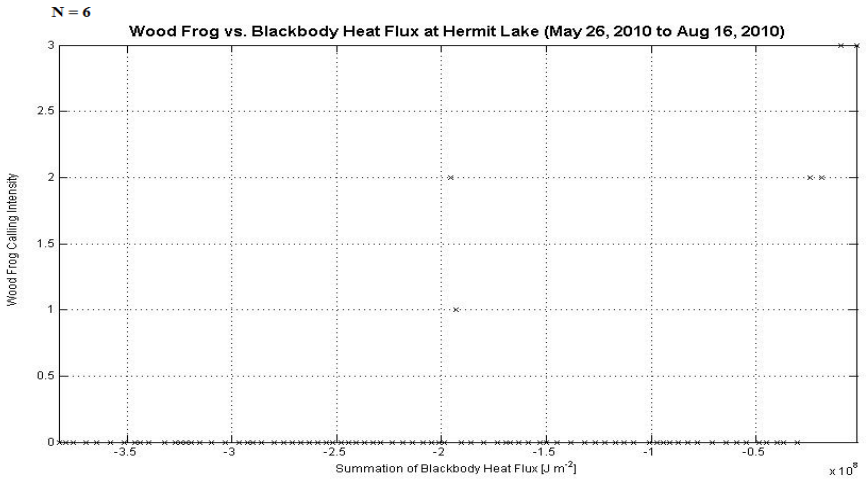

Figure B13. Comparison of the blackbody heat flux data to the wood frog calling intensity. There is insufficient calling activity data.

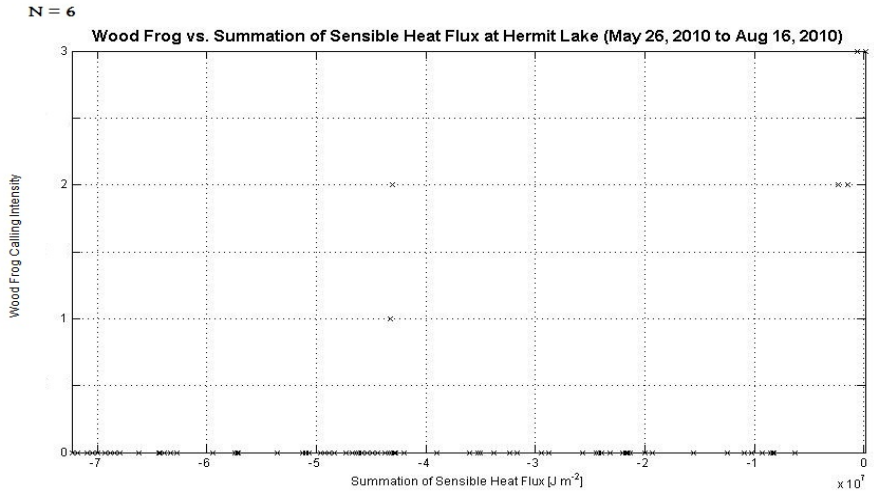

Figure B14. Comparison of the sensible heat flux data to the wood frog calling intensity. There is insufficient calling activity data.

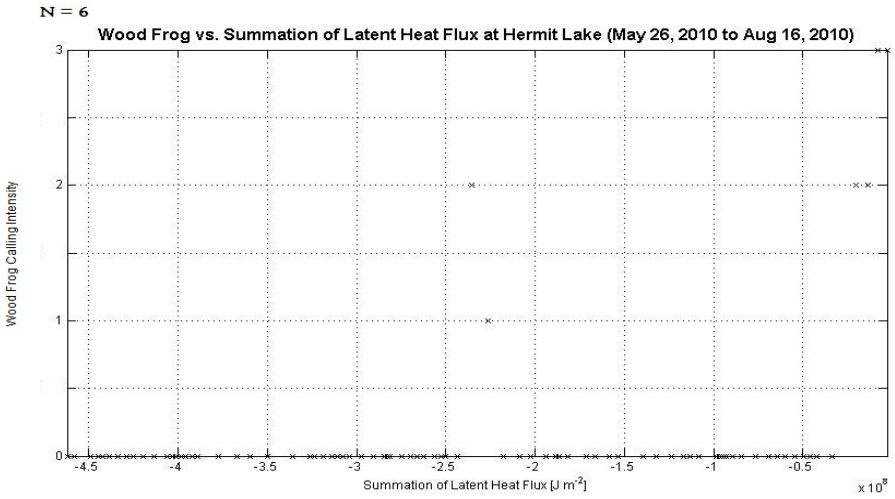

Figure B15. Comparison of the latent heat flux data to the wood frog calling intensity. There is insufficient calling activity data.

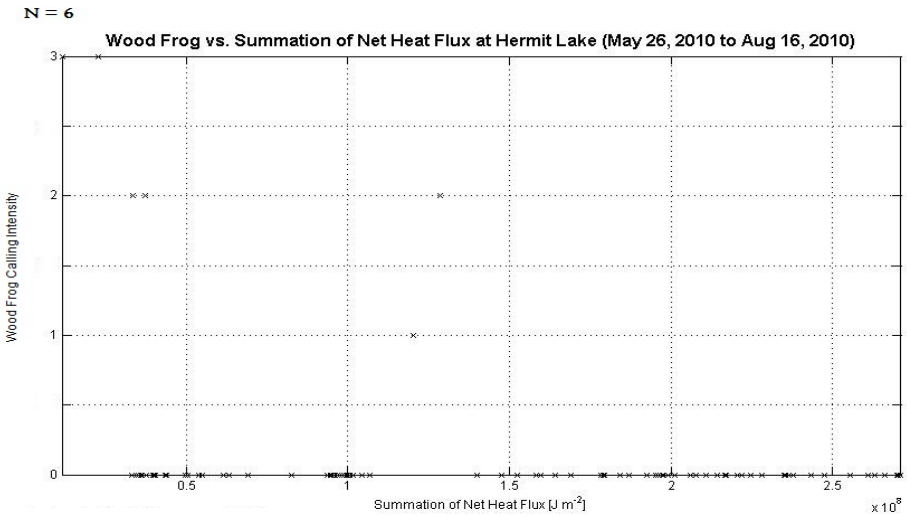

Figure B16. Comparison of the net heat flux data to the wood frog calling intensity. There is insufficient calling activity data.

c. American toad

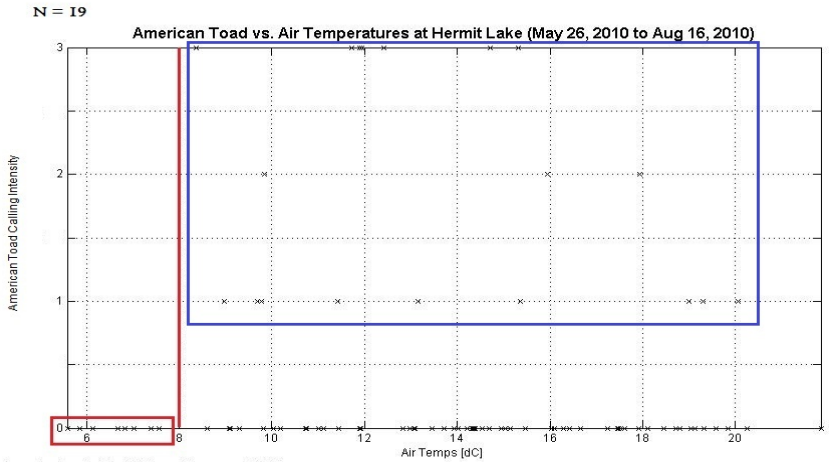

Figure B17. Comparison of the air temperature data and American toad calling intensity. American toad calling activity increases once the air temperatures exceed 8°C.

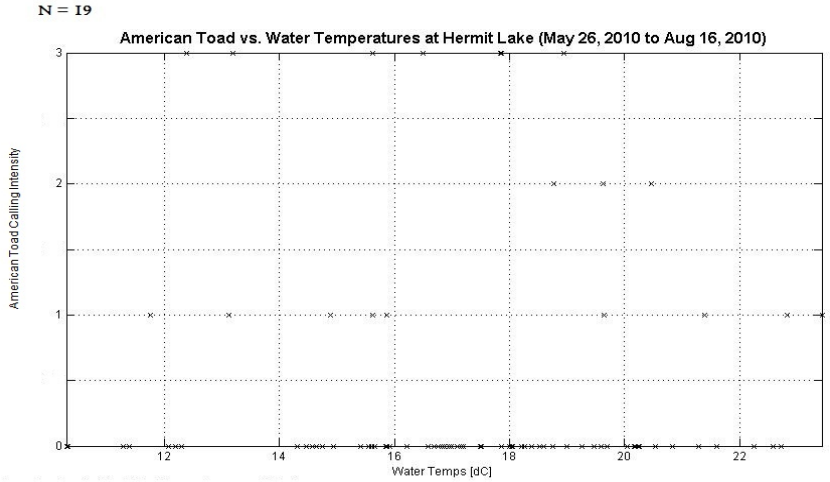

Figure B18. Comparison of the water temperature data and American toad calling intensity. The American toad is unaffected by changes in the water temperatures.

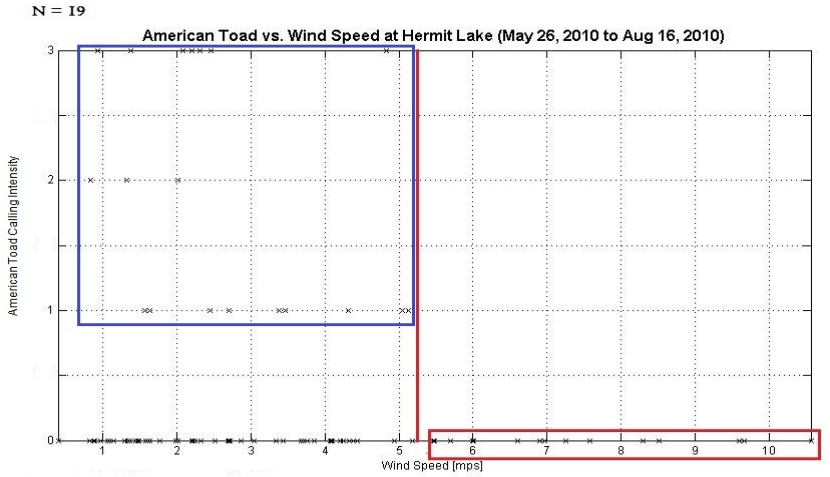

Figure B19. Comparison of wind speed data and American toad calling intensity. American toad calling activity ceases once the wind speed exceeds 5.2 m s^{-1}.

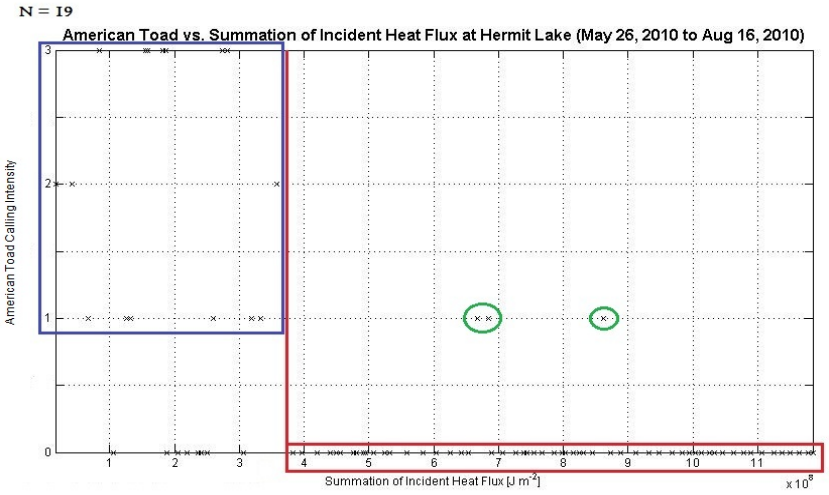

Figure B20. Comparison of the incident heat flux summation and American toad calling intensity. American toad calling activity decreases once the incident heat flux summation exceeds 3.8×10^8 J m^{-2}.

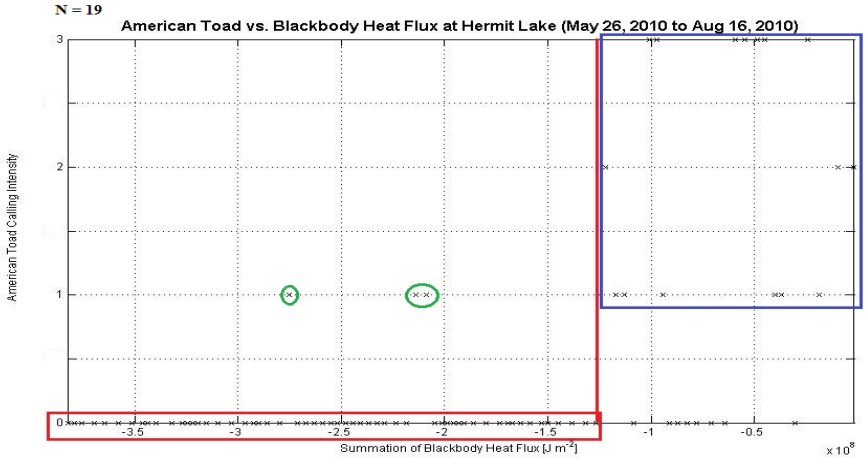

Figure B21. Comparison of the blackbody heat flux summation and American toad calling intensity. American toad calling activity increases once the blackbody heat flux summation exceeds -1.3×10^8 J m^{-2}.

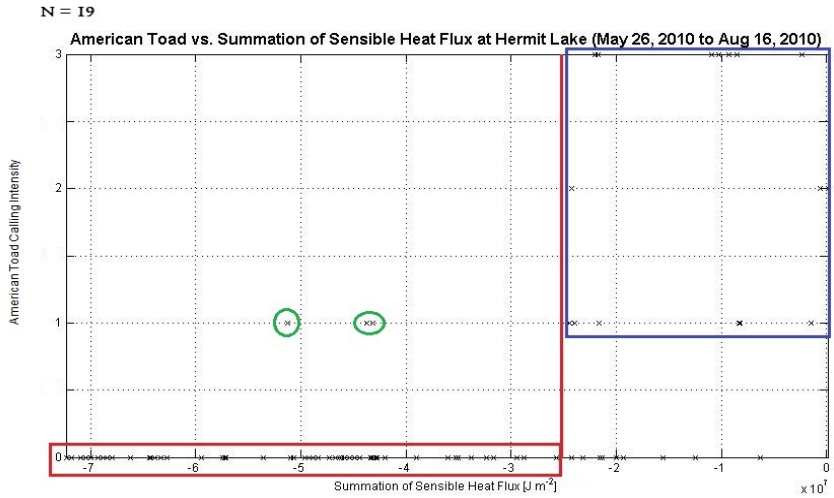

Figure B22. Comparison of the sensible heat flux summation and American toad calling intensity. American toad calling activity increases once the sensible heat flux summation exceeds -2.5×10^7 J m^{-2}.

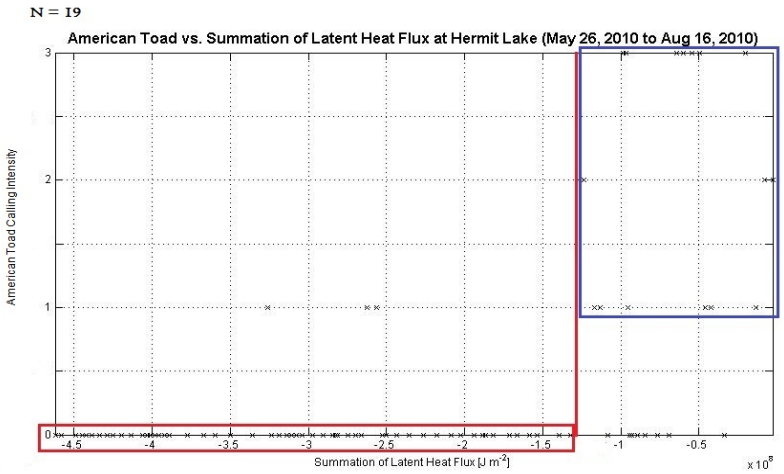

Figure B23. Comparison of the latent heat flux summation and American toad calling intensity. American toad calling activity increases once the latent heat flux summation exceeds -1.25x10^{8} J m^{-2}.

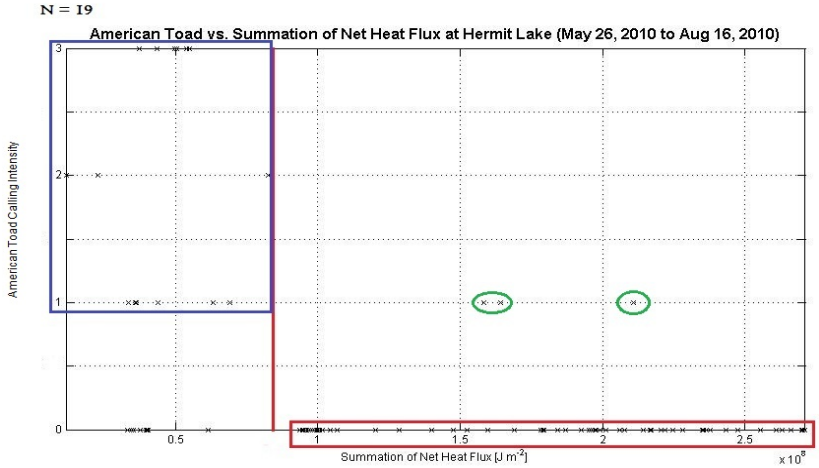

Figure B24. Comparison of the net heat flux summation and American toad calling intensity. American toad calling activity decreases once the net heat flux summation exceeds 0.8x10^{8} J m^{-2}.

d. Green frog

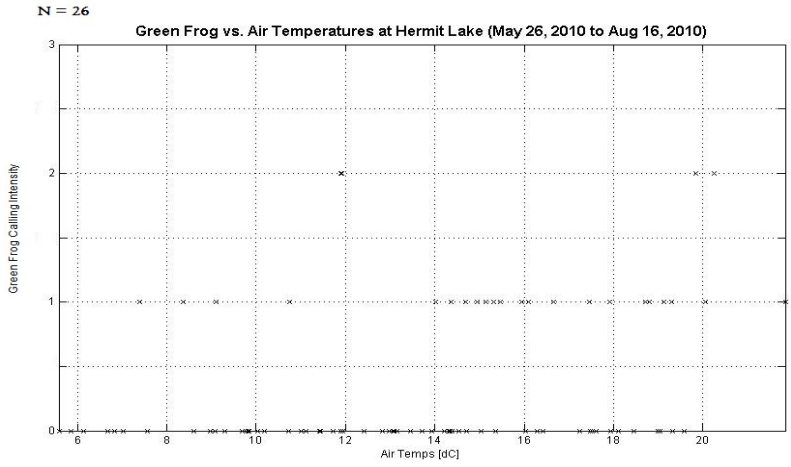

Figure B25. Comparison of the air temperature data and green frog calling intensity. The green frog is unaffected by changes in the air temperature.

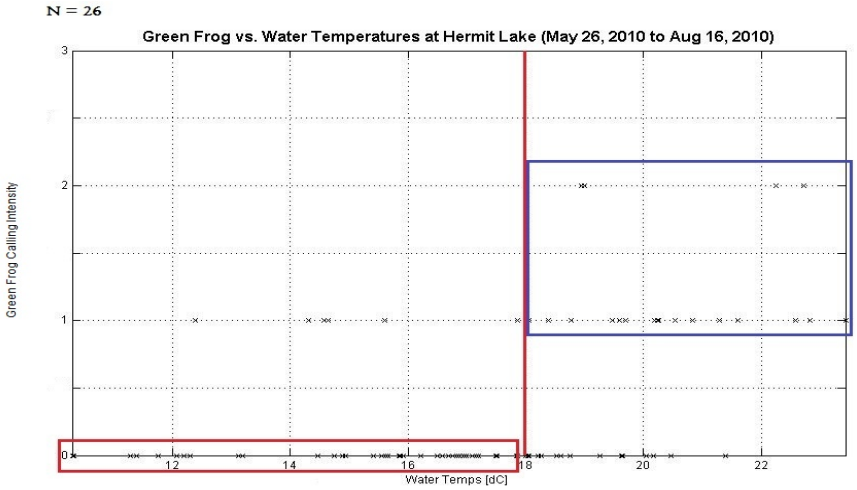

Figure B26. Comparison of surface water temperature data and green frog calling intensity. Green frog calling activity increases once the surface water temperatures exceed 18°C.

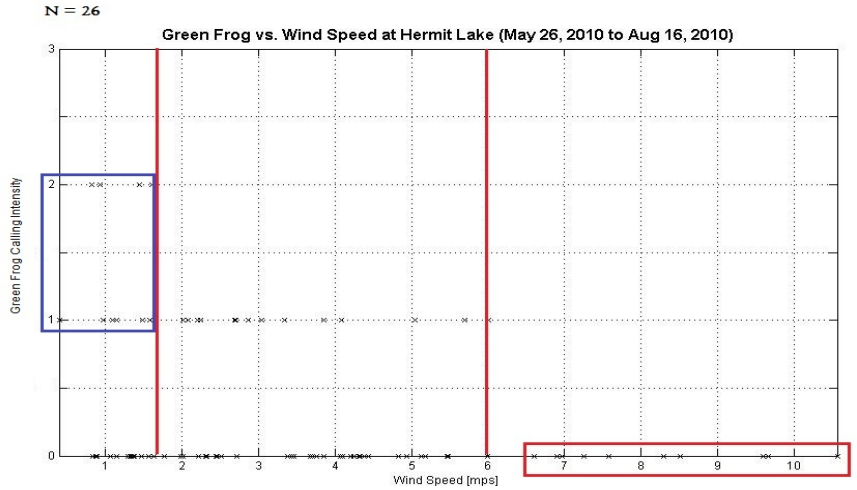

Figure B27. Comparison of wind speed data and green frog calling intensity. Green frog calling activity decreases once the wind speed exceeds 1.7 m s^{-1}.

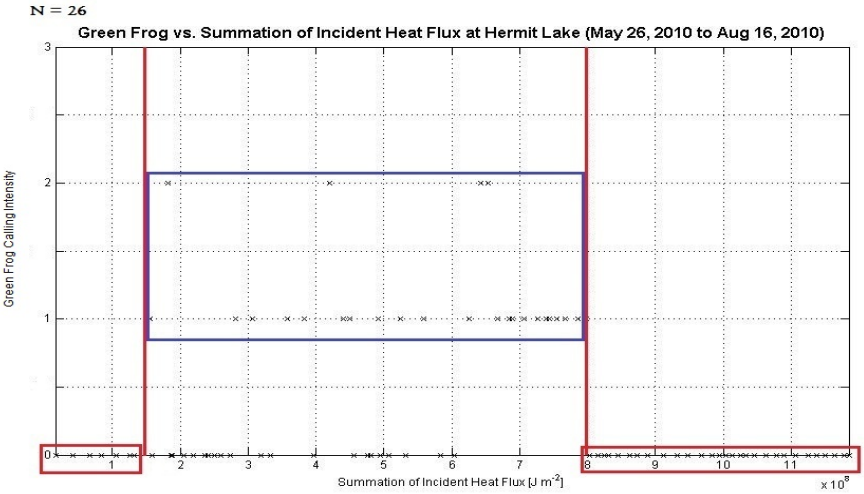

Figure B28. Comparison of the incident heat flux summation and green frog calling intensity. Green frog calling activity increases once the incident heat flux summation exceeds $1.5x10^8$ J m^{-2} and decreases once the heat flux values exceed $8x10^8$ J m^{-2}.

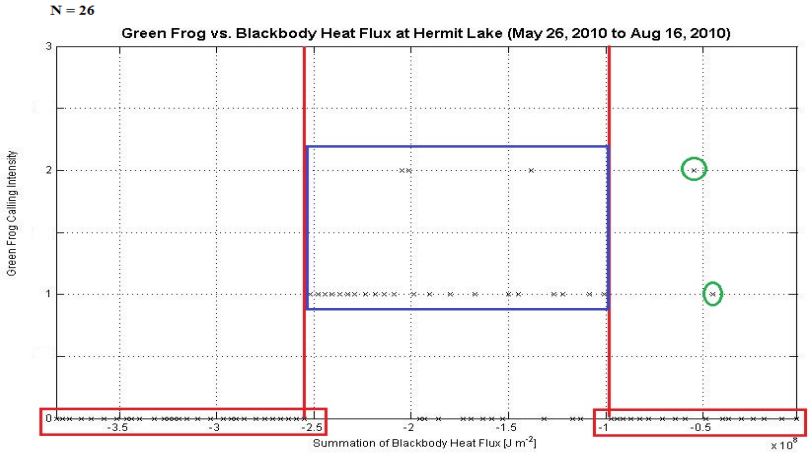

Figure B29. Comparison of the blackbody heat flux summation and green frog calling intensity. Green frog calling activity increases once the blackbody heat flux summation exceeds -2.5×10^8 J m^{-2} and decreases once the heat flux values exceed -1×10^8 J m^{-2}.

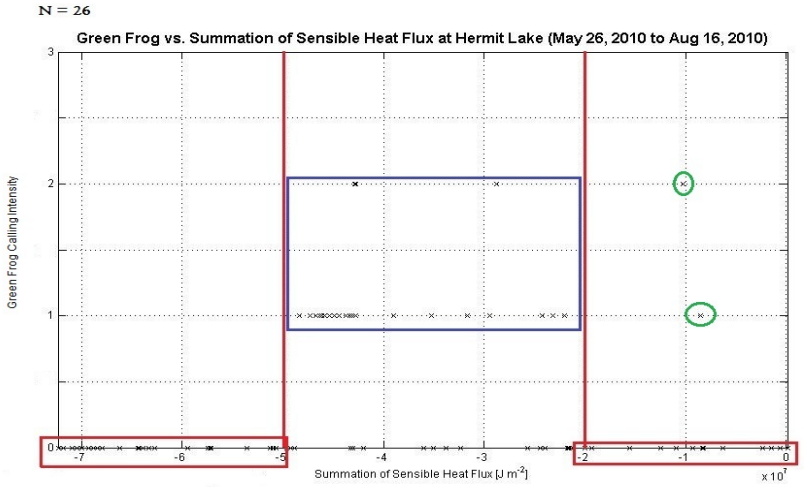

Figure B30. Comparison of the sensible heat flux summation and green frog calling intensity. Green frog calling activity increases once the sensible heat flux summation exceeds -5×10^7 J m^{-2} and decreases once the heat flux values exceed -2×10^7 J m^{-2}.

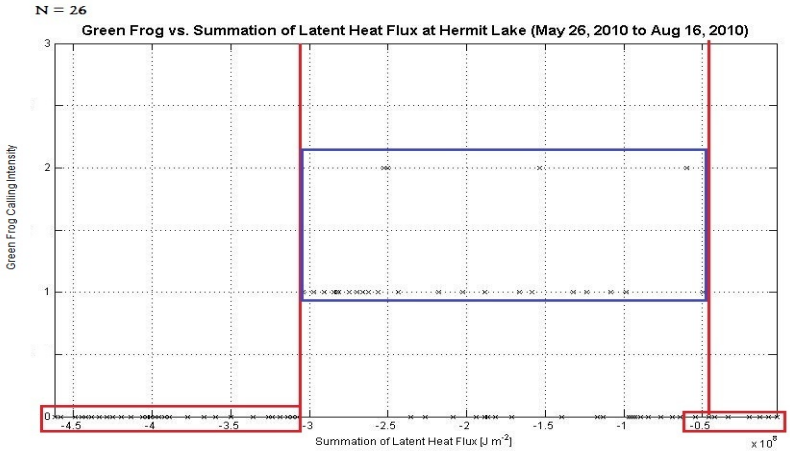

Figure B31. Comparison of the latent heat flux summation and green frog calling intensity. Green frog calling activity increases once the latent heat flux summation exceeds -3.1×10^8 J m^{-2} and decreases once the heat flux values exceed -0.5×10^8 J m^{-2}.

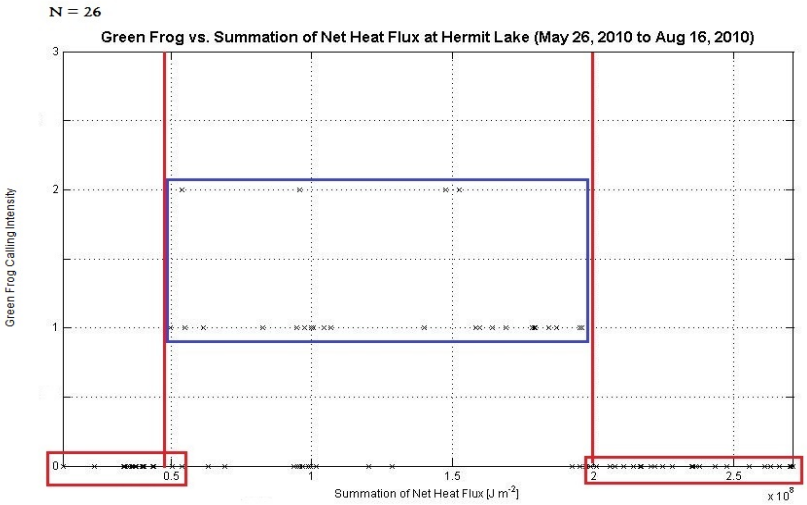

Figure B32. Comparison of the net heat flux summation and green frog calling intensity. Green frog calling activity increases once the net heat flux summation exceeds $0.5x10^8$ J m^{-2} and decreases once the heat flux values exceed $2x10^8$ J m^{-2}.

REFERENCES

Albert, A. and C.D. Mobley, 2003. *An analytical model for subsurface irradiance and remote sensing reflectance in deep and shallow case-2 waters*. Optics Express. 11(22): 2873-2890.

Bane, J.M, Jr., and K.E. Osgood, 1989. *Wintertime Air-Sea Interaction Processes Across the Gulf Stream*. Journal of Geophysical Research. 94: 10,755-10,772.

Barnes, Stanley L., 1964. A technique for maximizing details in numerical map analysis. Journal of Applied Meteorology, 3: 396 - 409.

Beardsley, Robert C., Edward P. Dever, Steven J. Lentz, and Jerome P. Dean, 1998. *Surface Heat Flux Variability over the Northern California Shelf. Woods Hole Oceanographic Institution Contribution No. 9406.* Accepted by the Journal of Geophysical Research, April, 1998.

Broecker, Wallace S., 1987. *The Biggest Chill.* Natural History. 10: 74-82.

Broecker, Wallace S., 1995. *The Glacial World According to Wally.* Palisades, New York: Lamont-Doherty Earth Observatory, Columbia University.

Brown, W.S., and R.C. Beardsley, 1978. *Winter Circulation in the Western Gulf of Maine: Part 1. Cooling and Water Mass Formation.* Journal of Physical Oceanography. 8: 265-277.

Brown, W.S., and J.D. Irish, 1993. *The Annual Variation of Water Mass Structure in the Gulf of Maine: 1986-1987*. Journal of Marine Research. 51: 53-107.

Budyko, M. I., 1974: Methods for determining the components of the heat balance. *Climate and Life*, David H. Miller, Ed, International Geophysical Series, Vol 18, Academic Press, 508 pp.

Churchill, James H. and W. Charles Kerfoot, 2007. *The Impact of Surface Heat Flux and Wind on Thermal Stratification in Portage Lake, Michigan.* Journal of Great Lakes. 33: 143-155.

Cogley, J. Graham, 1979. *The Albedo of Water as a Function of Latitude*. Monthly Weather Review. 107: 775-781.

Cook, Robert P., Todd A. Tupper, Peter W.C. Paton, and Brad C. Timm, 2011. *Effects of Temperature and Temporal Factors on Anuran Detection Probabilities at Cape Cod National Seashore, Massachusetts, USA: Implications for Long Term Monitoring.* Herpetological Conservation and Biology. 6(2): 25 – 39.

Dickey, T.D., D.V. Manov, R.A. Weller, and D.A. Seigel, 1994. *Determination of Longwave Heat Flux at the Air-Sea Interface Using Measurements from Buoy Platforms*. Journal of Atmospheric and Oceanic Technology. 11: 1057-1078.

Doner, Lisa, 2011. *Monitoring Environmental Change at Hermit Lake, Mt. Washington, NH*. Windswept. 52 (1): 36-40.

Duguay, Claude R., Greg M. Flato, Martin O. Jefferies, Patrick Menard, Kim Morris, and Wayne R. Rouse, 2003. *Ice-cover variability on shallow lakes at high latitudes: model simulations and observations.* Hydrological Processes. 17: 3465 – 3483.

Feng, Hui, 1996. *Wind-Induced Responses of The WesternCoastal Gulf of Maine During Spring and Summer 1994*. Master's Thesis, University of New Hampshire. Durham, New Hampshire.

Fofonoff, N.P, and R.C. Millard, Jr., 1983. Algorithms for The Computation of Fundamental Properties of Seawater. Unesco/SCOR/ICES/IAPSO Joint Panel on Oceanographic Tables and Standards, and SCOR Working Group 51.

Gill, Adrian E., 1982. *Atmosphere-Ocean Dynamics*. San Diego, California: Academic Press.

Gleckler, Peter J. and Bryan C. Weare, 1997. *Uncertainties in Global Ocean Surface Heat Flux Climatologies Derived from Ship Observations.* Journal of Climate. 10: 2764 – 2781.

Halliday, D., R. Resnick, and J. Walker, 1993. *Fundamentals of Physics*, pg. 553 ff. New York: John Wiley and Sons.

Hess, Seymour L., 1959. *Introduction to Theoretical Meteorology*. Malabar, Florida: Krieger Publishing Company.

Hopkins, Thomas S., 1976. Coastal Cooling in the Gulf of Maine. National Science Foundation Research Proposal #76-033. Bigelow Laboratory for Ocean Sciences, West Boothbay Harbor, Maine.

Hopkins, T.S., and N. Garfield III, 1979. *Gulf of Maine Intermediate Water*. Journal of Marine Research. 37:103-139.

Iqbal, Muhammad, 1983. *An Introduction to Solar Radiation.* San Diego, California: Academic Press.

Irish, J.D., and W.S. Brown, 1986. *An Archiving and Analysis System for Geophysical Data*. Marine Data Systems International Symposium (MDS86): 64-69.

Jones, Michael T. and Scott D. Smyers, 2008. *Preliminary Biological Surveys at Four Alpine Pond Sites in the White Mountain National Forest, New Hampshire.* Oxbow Associates, Inc. 1 – 23.

Jones, Michael T. and Scott D. Smyers, 2010. *Occurrence of Pond-breeding Amphibians at Alpine Ponds in the White Mountains, New Hampshire.* Northeastern Naturalist. 17(1): 161 – 166.

Josey, Simon A., Daniel Oakley, and Robin W. Pascal, 1997. *On estimating the atmospheric longwave flux at the ocean surface from ship meteorological reports.* Journal of Geophysical Research. 102: 27961 – 27972.

Joyce, T.M., 1987. *Meteorology and Air-Sea Interactions*, in The Marine Environment of the U.S. Atlantic Continental Slope and Rise (Milliman, John, D., and W. Redwood Wright, eds.). Woods Hole, Massachusetts: Jones and Bartlett Publishers, Inc.

Kearey, Philip, and Frederick J. Vine, 1996. *Global Tectonics.* London: Blackwell Science Ltd.

Key, Jeffrey R., Robert A. Silcox, and Robert S. Stone, 1996. *Evaluation of surface radiative flux parameterizations for use in sea ice models.* Journal of Geophysical Research. 101: 3839 – 3849.

Launiainen, Jouko and Bin Cheng, 1998. *Modelling of ice thermodynamics in natural water bodies.* Cold Regions and Technology. 27: 153 – 178.

Leathers, Robert A., and Norman J. McCormick, 1999. *Algorithms for ocean-bottom albedo determination from in-water natural-light measurements.* Applied Optics. 38(15): 3199-3205.

Lide, David R., 1997. *Handbook of Chemistry and Physics 78th Edition*, pg. 6-7 ff. New York: CRC Press LLC.

Lide, Susan M., 1992. *An Introduction to Marine Biogeochemistry.* New York: John Wiley & Sons, Inc.

Lind, Richard J. and Kristina B. Katsaros, 1986. *Radiation Measurements and Model Results From R/V Oceanographer During STREX 1980*. Journal of Geophysical Research. 91: 13308 – 13314.

Lutgens, F.K., and Edward J. Tarbuck, 1998. *The Atmosphere*. New Jersey: Prentice Hall, Inc.

Marion, W. and R. George, 2001. *Calculation of Solar Radiation Using A Methodology With Worldwide Potential*. Solar Energy. 71(4): 275-283.

Martin, Jonathan E., 2006. *Mid-Latitude Atmospheric Dynamics: A First Course.* John Wiley and Sons, Ltd., 237 – 273.

Mathworks, 2010: MATLAB R2010a Student. The Mathworks, Inc. [Available online at http://www.mathworks.com/products/matlab/.]

Maykut, Gary A. and Phil E. Church, 1973. *Radiation Climate of Barrow, Alaska, 1962-1966.* Journal of Applied Meteorology. 12: 620-628.

Meehl, G. A., and Coauthors, 2007: Global climate projections. *Climate Change 2007: The Physical Science Basis,* S. Solomon *et al.*, Eds, Cambridge University Press, 996 pp.

Miller, S., 1999. *Air-Sea Heat Flux in the Gulf of Maine Meteorological Forcing and Oceanic Response*. Master's Thesis. University of New Hampshire, 232 pp.

Miller, S., 2011: AIRSEA TOOLKIT. [Available online at http://vortex.plymouth.edu/~stmiller/stmiller_content/Matlab/matlab.html.]

Miller, S.T., W.S. Brown, and F.L. Bub, 1999. CONVEX Moored Measurements Data Report: October 1997 - May 1998. Technical Report. Ocean Process Analysis Laboratory, University of New Hampshire, Durham, New Hampshire.

Miller, Samuel, 2011. Personal Communication. Dr. Miller is an associate professor employed by the Atmospheric Sciences and Chemistry Department, Plymouth State University, Plymouth, New Hampshire.

Mooers, C.N.K., J. Fernandez-Partages, and J.F. Price, 1976. Meteorological Forcing Fields of the New York Bight. Technical Report, University of Miami. Miami, Florida.

Mountain, D.G., and J.P. Manning, 1994. *Seasonal and Interannual Variability in the Properties of the Surface Waters of the Gulf of Maine*. Continental Shelf Research. 14: 1555-1581.

Mountain, D.G., Glenn A. Strout, and Robert C. Beardsley, 1996. *Surface Heat Flux in the Gulf of Maine.* Deep Sea Research II. 43: 1533-1546.

National Climatic Data Center, cited 2011: Climate maps of the United States database. [Available online at http://hurricane.ncdc.noaa.gov/cgi-bin/climaps/climaps.pl?directive=welcome&subrnum=.]

Payne, R.E., 1972. *Albedo of the Sea Surface*. Journal of Atmospheric Science. 29: 959-970.

Pegau, Scott, J. Ronald, V. Zanefeld, and James L. Mueller, 2003. *Inherent Optical Property Measurement Concepts: Physical Principles and Instruments*. Ocean Optics Protocols For Satellite Ocean Color Sensor Validation. 4: 1-18.

Petty, Grant W., 2008. *A First Course in Atmospheric Thermodynamics.* Danvers, Massachusetts: Sundog Publishing, 336 pp.

Petzold, D. E., 1977. *An estimation technique for snow surface albedo.* Climatological Bulletin. McGill University. 21: 1 – 11.

Pickard, G.L., and W.J. Emery, 1982. *Descriptive Physical Oceanography*. New York: Pergamon Press.

Pond, Stephen, and George L. Pickard, 1983. *Introductory Dynamical Oceanography.* App. A.3.2., pg. 310. Oxford:Butterworth-Heinemann.

Reed, R.K. and P.J. Stabeno, 2001. *Surface Heat Fluxes and Subsurface Heat Content at a Site Over the Southeastern Bering Sea Shelf, May – July 1996.* Deep Sea Research Part II: Tropical Studies in Oceanography. 15 pp.

Rizzi, Giuliano, 2008: Hydrotherodynamics of a small alpine lake. *Monographs of the School of Doctoral Studies in Environmental Engineering*, No. 12, Univeristá Delgi Studi Di Trento. 196 pp.

Rogers, Christopher K., Gregory A. Lawrence, and Paul F. Hamblin, 1995. *Observations and numerical simulation of a Shallow ice-covered lake.* Limnology and Oceanography, 40(2): 374-385.

Rogers, R.R., and M.K. Yau, 1989. *A Short Course in Cloud Physics.* Woburn, Massachusetts: Butterworth-Heinemann.

Smyers, Scott, 2011. Personal Communication. Mr. Smyers is a research biologist employed by Oxbow Associates, Inc, Acton, Massachusetts.

Stommel, Henry, 1972. *Deep winter-time convection in the western Mediterranean Sea*, in Studies in Physical Oceanography, A Tribute to George Wüst on his 80th Birthday (A.L. Gordon, ed.). Gordon and Breach, 2: 207-218.

Torrence, Christopher and Gilbert P. Compo, 1998. *A Practical Guide to Wavelet Analysis.* Bulletin of the American Meteorological Society, 79: 61 – 78.

Torrence, Christopher and Gilbert P. Compo, 2011. Interactive Wavelet Plot [Available online at http:// http://paos.colorado.edu/research/wavelets/].

Wallace, John M. and Peter V. Hobbs, 2006: *Atmospheric Science. An Introductory Survey.* Academic Press, 481 pp.

Wu, Jin, 1992. *Variation of Heat Transfer Coefficients with Environmental Parameters*. Journal of Physical Oceanography. 22: 293-300.